Temporal Dynamics and Statistical Characteristics of Ocular Wavefront Aberrations and Accommodation

by Conor Leahy

Supervisor: Prof. Chris Dainty

OÉ Gaillimh
NUI Galway

A thesis submitted in partial fulfilment of the requirements for the degree of
Doctor of Philosophy,

School of Physics, Science Faculty,
National University of Ireland, Galway

March 2010

Abstract

It has long been known that the optical quality of the human eye varies continuously in time. These variations are largely attributable to changes in the optical aberrations of the eye, among which one of the principal influences is the presence of fluctuations in the eye's accommodative response. New technological developments now permit us to study the dynamics of ocular aberrations and accommodation with unprecedented resolution and accuracy. In this thesis, we present an in-depth analysis of the dynamics of ocular aberrations and accommodation, measured with a high-performance aberrometer. We aim to characterise the spectral content and statistical properties of aberrations and accommodation. In particular, our results demonstrate the systematic dependence of accommodation dynamics on the level of accommodative effort. Given that the temporal dynamics of ocular aberrations and accommodation are generally known to be non-stationary, we include methods in our analysis that are targeted specifically towards non-stationary processes. We show that as well as non-stationarity, the measured signals exhibit characteristics that suggest long-term dependence and self-affinity. We then present a method of modelling the temporal dynamics of ocular aberrations and accommodation, based on the findings of our measurements and analysis. The model enables time-domain simulation of the dynamics of these processes. Finally, we discuss the implications of our results, along with possible applications and the potential impact of this work on future studies.

Acknowledgements

I would like to express my gratitude to my supervisor, Prof. Chris Dainty for his constant support, encouragement, and inspiration throughout my PhD studies. It has been a real privilege to work with you Chris, thank you for everything. I am also very grateful to Dr. Luis Diaz-Santana for adding his insight to the project, as well as for his endless encouragement and enthusiasm. Thank you Emer for all the times you went out of your way in helping me to get organised, from my first day of work right up to the submission of this thesis.

I am thankful to all my colleagues in the Applied Optics Group for making it such a great environment to work in. I would especially like to thank Charlie for all his help and advice over the last four years, without which I simply could not have accomplished this work. Thanks to Andrew and Arlene for being such good company in the office, to Maciej, Dirk, and Elie for all the laughs, and to all the other friends that I have been lucky enough to meet through working here.

I would like to thank my brothers and sister, without whom I don't think I would have ever even considered attempting to study for a PhD. Thanks also to all my great friends who have supported me along the way. Most of all, I am eternally grateful to my parents for everything they have done for me. I will not forget all the wonderful support that you have given me throughout my entire education, thank you.

Conor Leahy
Galway, December 2009

Contents

List of Figures

Preface

The level of interest in the structure and function of the human eye stems not only from the fact that sight is the most utilised of our senses, but also because of the importance of the visual system as an extension of the brain. Though the human eye has been studied by scientists for centuries, the work of Thomas Young and Hermann von Helmholtz has perhaps been particularly instrumental in shaping our modern knowledge of the human visual system [1, 2]. These experiments showed the influence of the optical components within the eye on image formation. Young's experiments on accommodation demonstrated that the optical power of the eye varies in time due to changes in the lens. Helmholtz showed that despite all the sophisticated and precise tasks that can be performed with human vision, its optical qualities are far from ideal, due in part to optical defects known as aberrations. Furthermore, he demonstrated that these aberrations were time-varying. These dynamic features of the eye have attracted much study since, and interest has been been further boosted in the last decade by the development of ocular aberration correction using adaptive optics [3]. Advances in wavefront sensing methods and technology, along with developments in fields such as corneal topography, mean that ocular wavefront dynamics can be studied with increased precision and accuracy. This thesis attempts to characterise and model some of these time-varying properties of the eye, and to increase our understanding of them. In particular we look to answer questions such as: how do ocular wavefront dynamics evolve in time? What are their causes and what factors influence them? Are the dynamic changes merely a physiological byproduct, or do they play an active role in the visual system - and if so, what is this role?

There are two main aims of this research. Firstly, we aim to improve our knowledge and understanding of the temporal dynamics of the human optical system. This is important in areas such as the investigation of the impact of these dynamic effects

on visual performance, and the improvement of accuracy in the estimation of ocular aberrations [4]. Secondly, we endeavour to develop a realistic model of ocular dynamics based on our findings. This not only assists us in understanding the nature of the underlying processes, but could also be useful in the testing of aberrometers, customised contact lenses, or in simulations of retinal image quality.

Parts of the project were carried out in collaboration with Charles Leroux of the Applied Optics Group, and with Dr. Luis Diaz-Santana of City University London. The collaborative elements of work included in this thesis are detailed in the synopsis below. The remainder of the thesis represents the author's own work, except where otherwise referenced or stated in the text.

Synopsis

Chapter 1 presents background information on the human eye. A general description of the physiology of the human eye is given, followed by a more detailed look at the particular properties of the eye that this thesis is concentrated upon, namely ocular aberrations and ocular accommodation.

Chapter 2 is intended to lay the statistical and mathematical foundations for the rest of the thesis. Some general properties of biomedical signals are discussed, followed by a description of the statistical and signal processing tools used in the analysis and characterisation of measured data. Some signal modelling techniques are also presented, with particular attention paid to the modelling of non-stationary processes.

Chapter 3 focuses on the dynamics of ocular aberrations. A general explanation of wavefront sensing and aberrometry is given, followed by a technical description of the particular aberrometer used throughout this work. The experimental procedure involved in the measurement of the dynamics of ocular aberrations is described in detail, and the results are presented along with some statistical analysis. The quality of these results compared to previous studies is discussed, along with information uncovered by the analysis. Section 3.2 describes work carried out in collaboration with Charles Leroux of the Applied Optics Group, who designed and implemented the aberrometer, developed the experimental procedure for measuring the dynamics of aberrations, and also contributed to the data processing.

Chapter 4 describes measurements of the dynamics of the accommodative system. The precise meaning of the accommodative signal is first defined, followed by a description of the experimental procedure used for its measurement. Results are pre-

sented for 9 young, healthy subjects. Some spectral and statistical analysis is then shown, including techniques that have not previously been used in accommodation studies. Results are compared from subject to subject, and particular attention is paid to the effects of changes in target vergence on the results. Evidence that suggests self-affine and long-term correlated behaviour in accommodative response time series is presented, followed by a discussion of the implications of these findings. The full body of work described in this chapter, apart from Section 4.5, was conducted in collaboration with Charles Leroux of the Applied Optics Group and Dr. Luis Diaz-Santana of City University, London.

Chapter 5 describes modelling of ocular aberrations and the accommodative response. The motivations behind developing such a model are explained, and several modelling methods that were considered throughout the course of the work are described, along with their respective benefits and drawbacks. A non-stationary power-law model is presented as the most accurate and useful of the modelling approaches. The formulation of this model is described in detail, along with a discussion of how the model parameters are selected. Some examples of simulation and validation of the model are then presented. The chapter is concluded with a discussion of possible modifications to the model, and some potential applications.

Chapter 6 concludes on the work presented in this thesis and discusses the implications for the study of ocular dynamics. Finally, some suggestions for future related topics of research are given.

Publications

- C.M. Leahy and J.C. Dainty. Modelling of nonstationary dynamic ocular aberrations. In *Proceedings of 6th International Workshop on Adaptive Optics for Industry and Medicine, Galway, Ireland*, 6:342-347, 2007.

- C. Leahy, C. Leroux, C. Dainty, and L. Diaz-Santana. Temporal dynamics and statistical characteristics of the microfluctuations of accommodation: Dependence on the mean accommodative effort. *Opt. Express*, 18:2668-2681, 2010.

Chapter 1

Optics of the Eye and Vision

Human vision is a complex process that consists of several interacting systems. In this chapter we will describe some key elements of the eye and identify the functions and limitations associated with them. We will proceed to discuss ocular aberrations and ocular accommodation, which are key subjects of this thesis. This will help to give an understanding of how these phenomena are quantified and interpreted, as well as the challenges and limitations encountered in their measurement.

1.1   Optics of the Eye

The human eye is a robust optical system [5], whose purpose is to image objects onto a sensing element (the retina). It consists of an optical path containing refractive components, a limiting aperture, and a sensor. A schematic of the eye is given in Figure 1.1. In this section, we discuss some of the basic components of the eye, and their relevance to this project. The most immediate refractive element encountered by light incident upon the eye is the anterior surface of the tear film [6], which has a standard refractive index of $n_{tf} \approx 1.337$ [7]. Given that the refractive index of air is 1, it can be said that the interface between air and the tear-film is the largest change in refractive index encountered in the eye [8]. The combination of the tear-film and the cornea results in a smooth optical surface that refracts light. The cornea itself is the most powerful refractive medium in the eye however, typically having an optical power of
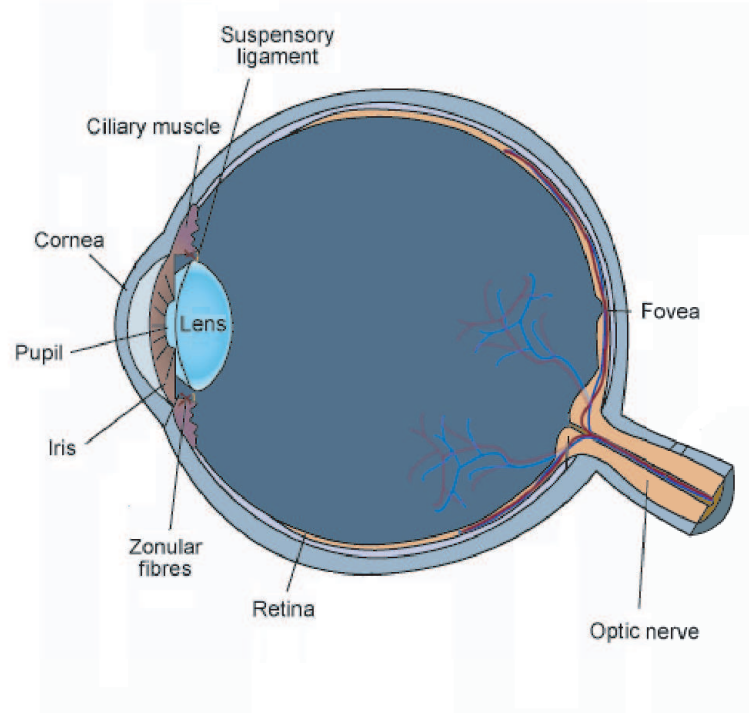
Figure 1.1: Schematic of the human eye.

around 40 dioptres (D) and a standard refractive index of $n_c \approx 1.37$ [3].

The next most significant refractive element in the eye is the lens, an epithelial tissue. The refractive index within the lens is non-uniform, being greater in the centre than in the periphery. Gullstrand [2] proposed an equation describing the refractive index distribution within the lens. A value of $n_{eq} = 1.42$ has been suggested as the refractive index for a theoretically equivalent uniform lens [9]. The function of the lens is to provide a means of adjusting the refractive power of the eye, in order to bring objects at different distances into focus. These adjustments are possible through changes in the shape of the lens [10]. This process is known as accommodation, and will be discussed further in Section 1.3.

In between the cornea and the lens is the iris, which forms the aperture stop of the eye. The opening in the iris is commonly known as the pupil. The pupil size is modulated by two antagonistic muscles, which are under reflex rather than voluntary control [9]. The most important factor affecting the pupil size is the level of illumination, with the response to an increase in illumination being a decrease in pupil size. The pupil size may naturally vary from about 2-8 mm in this manner, however the pupil size

can also be artificially altered (e.g. through the use of drugs such as Tropicamide). A detailed discussion of the various factors affecting pupil size can be found in the literature [11].

The retina is the sensing element of the eye. The image formed on the retina is sampled by light-sensitive cells known as photoreceptors. These cells are of two types, rods and cones. Rods have higher sensitivity than cones but poorer spatial resolution and a lower saturation level. They are typically associated with low-light vision [9]. In general, there are three types of cones, each of which have a different peak sensitivity wavelength. The largest concentration of cones is found in the region known as the fovea, which is important for performing tasks where visual detail is paramount. The central region of the fovea is known as the foveola, and contains only cones. In total, there are approximately 100 million rods and 5 million cones in the retina [3]. Visual information is transferred from the retina to the brain via the optic nerve. This is achieved through the retinal ganglion cells, which receive visual information from the photoreceptors and transmit them to the brain.

1.2 Ocular Aberrations

The quality of the image formed by an optical system is reduced by aberrations, and the human eye is no exception. Aberrations can be classed as either chromatic or monochromatic. Chromatic aberrations are related to dispersion, the variation of refractive index with wavelength (e.g., within a lens). Monochromatic aberrations occur even for light of a single wavelength. In this thesis we will concentrate on monochromatic aberrations, and so further references to "ocular aberrations" should be taken to refer to monochromatic aberrations.

In geometrical optics, the ideal situation is for all rays emanating from a point object to intersect at the point image. In practice, this is not achievable in most cases. Deviations from the common ray intersection point in the image plane are observed, and these are classified as aberrations [12]. Throughout the text we will make references to the *wavefront*, which can be considered as the locus of points of equal optical phase of a wave. The *wave aberration* is the optical deviation of the wavefront from a reference sphere measured along a particular ray. A detailed description of ray and wave aberrations can be found in Mahajan [13].

The wave aberration $W(\rho,\theta)$, with radial co-ordinate ρ and azimuthal angle co-ordinate

θ, can be represented using a polynomial expansion, of the form

$$W(\rho,\theta) = \sum_{n=0}^{\infty} \sum_{m=0}^{n} a_n^m \mathcal{P}_n^m(\rho,\theta) \tag{1.1}$$

where $\mathcal{P}_n^m$ denotes a polynomial term and a_n^m is the corresponding weight coefficient, with angular frequency m and radial order n. Throughout this thesis, we will use Zernike circle polynomials for expansion of the wave aberration. Zernike polynomials are a useful expansion for describing the aberrated wavefront in an optical system with a circular pupil, and have been used in many ocular aberration studies [3, 14–21]. Though they are only one of many possible representations for such a system [3], Zernike polynomials have a number of properties that make them particularly suitable. Firstly, they form a complete orthonormal set over the unit circle. Secondly, the polynomials in the Zernike expansion represent *balanced* aberrations. This means that each polynomial represents a combination of power series terms that is optimally balanced to give minimum variance across the pupil [22]. Another useful property is that the coefficient of each term in the Zernike polynomial expansion represents its standard deviation, and the sum of the squares of the coefficients yield the overall aberration variance. These factors have led to Zernike polynomials becoming accepted among the vision community as an ANSI standard for reporting wavefront aberrations of the eye [23].

We expand the phase aberration function in terms of a complete set of Zernike circle polynomials as follows [13]:

$$W(\rho,\theta) = \sum_{n=0}^{\infty} \sum_{m=0}^{n} c_n^m \left[\frac{2(n+1)}{1+\delta_{m0}} \right]^{\frac{1}{2}} R_n^m(\rho) \cos m\theta \tag{1.2}$$

$$= \sum_{n=0}^{\infty} \sum_{m=0}^{n} c_n^m Z_n^m(\rho,\theta) \tag{1.3}$$

where δ_{m0} is the Kronecker delta function, n and m are positive integers for which $n - m \geq 0$, and

$$R_n^m(\rho) = \sum_{s=0}^{(n-m)/2} \frac{(-1)^s (n-s)!}{s! \left(\frac{n+m}{2} - s \right)! \left(\frac{n+m}{2} - s \right)!} \rho^{n-2s} \tag{1.4}$$

is a polynomial of degree n in ρ containing terms in ρ^n, ρ^{n-2}, and ρ^m. The Zernike expansion coefficients c_n^m are given by:

$$c_n^m = \left(\frac{1}{\pi} \right) [2(n+1)(1+\delta_{m0})]^{\frac{1}{2}} \int_0^1 \int_0^{2\pi} W(\rho,\theta) R_n^m(\rho) \cos m\theta \rho d\rho d\theta \tag{1.5}$$

7
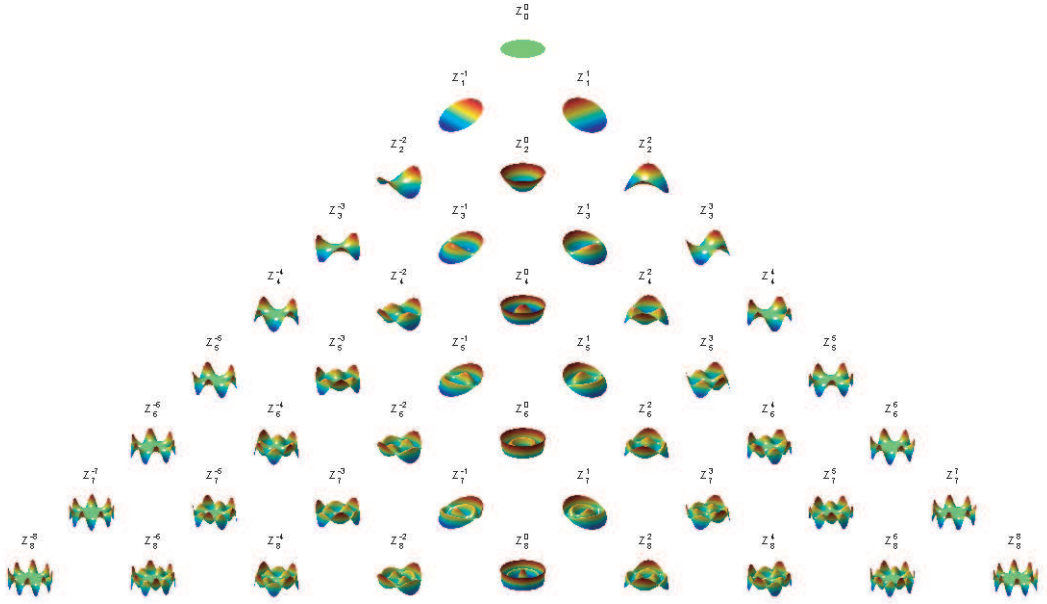
Figure 1.2: Periodic table of Zernike circle polynomials up to and including the 8th radial order. The author would like to thank Dr. David Lara for help in producing this image.

In practice, a finite number N of Zernike polynomials is used to represent the wave aberration function, which can be expressed as follows:

$$W(\rho,\theta) = \sum_{n=1}^{N} \sum_{m=0}^{n} c_n^m Z_n^m(\rho,\theta) + \epsilon(\rho,\theta) \tag{1.6}$$

where $\epsilon(\rho,\theta)$ denotes the modelling error. A pyramid representation of Zernike polynomials up to and including the 8th radial order is given in Figure 1.2. Table 1.1 gives the polynomial representations up to and including the 4th radial order. As mentioned previously, each aberration coefficient c_n^m also gives the standard deviation of its corresponding aberration term, and so once the expansion coefficients are known, the variance of the wave aberration function can easily be determined as follows [22]:

$$\sigma_W^2 = \left\langle W^2(\rho,\theta) \right\rangle - \left\langle W(\rho,\theta) \right\rangle^2 \tag{1.7}$$

$$= \sum_{n=1}^{N} \sum_{m=0}^{n} (c_n^m)^2 \tag{1.8}$$

The quantity σ_W^2 is sometimes known as the *RMS wavefront error*. Another feature

Table 1.1: Zernike polynomial terms up to and including the 4th radial order [24].

n	m	Zernike Polynomial	Name
0	0	1	Piston
1	-1	$2\rho\sin\theta$	y-tilt
1	1	$2\rho\cos\theta$	x-tilt
2	-2	$\sqrt{6}\rho^2\sin 2\theta$	Astigmatism ($\pm 45°$)
2	0	$\sqrt{3}(2\rho^2 - 1)$	Defocus
2	2	$\sqrt{6}\rho^2\cos 2\theta$	Astigmatism ($0°$ or $90°$)
3	-3	$\sqrt{8}\rho^3\sin 3\theta$	y-trefoil
3	-1	$\sqrt{8}(3\rho^3 - 2\rho)\sin\theta$	y-coma
3	1	$\sqrt{8}(3\rho^3 - 2\rho)\cos\theta$	x-coma
3	3	$\sqrt{8}\rho^3\cos 3\theta$	x-trefoil
4	-4	$\sqrt{10}\rho^4\sin 4\theta$	y-quadrafoil
4	-2	$\sqrt{10}(4\rho^4 - 3\rho^2)\sin 2\theta$	y-secondary astigmatism
4	0	$\sqrt{5}(6\rho^4 - 6\rho^2 + 1)$	Spherical Aberration
4	2	$\sqrt{10}(4\rho^4 - 3\rho^2)\cos 2\theta$	x-secondary astigmatism
4	4	$\sqrt{10}\rho^4\cos 4\theta$	x-quadrafoil

that makes Zernike polynomials particularly useful for studies of ocular aberrations is that certain terms in the expansion can be intuitively related to commonly known types of aberrations in the human eye. Standard ophthalmic prescriptions typically aim to correct for defocus and astigmatism in the eye. Due to the balanced nature of Zernike polynomials, these conditions are in fact distributed among multiple polynomial terms [25]. For example, the Zernike Z_2^0 term is related to the common focus error conditions in the eye (such as myopia and hypermetropia) and hence is often referred to as Zernike defocus, but the Zernike spherical aberration polynomial term, Z_4^0, also contains a defocus component. The lack of rotational symmetry of the optical system in the eye leads to astigmatism, and this is partly reflected in the Z_2^{-2} and Z_2^2 terms. Zernike terms of third order and above are commonly referred to as *higher-order aberrations*. These include aberrations that are well known in general optical systems and optometry, such as spherical aberration and coma [9]. Spherical aberration describes the phenomenon whereby rays from a point source that strike a spherical surface at varying distances from its centre are refracted by different amounts, with the result that they are not brought to a common focus. Coma is typically associated with the apparent distortion of off-axis sources, e.g. due to decentrations in the optical system [9].

Early studies of aberrations other than defocus in the eye include work by Thomas Young on astigmatism [1], as well as experiments later described by Gullstrand [2]. More recently, population studies have been carried out to assess the statistical occurrence of aberrations, including higher order aberrations [19, 20, 26]. The conclusion from these studies were that the higher order aberrations are generally much smaller in magnitude than defocus and astigmatism, though their contribution to the wave aberration variance is still significant. It was also interesting to note that when averaged across the population, the mean of the higher order Zernike aberrations tends to zero, except for the Z_4^0 spherical aberration term. Thibos et al. [19] also reported significant correlations between certain pairs of Zernike terms, as well as the presence of some bilateral symmetry between the left and right eyes.

Dynamics of Aberrations

Helmholtz provided early evidence that the aberrations of the eye fluctuate in time [2], with the aid of a demonstration that is reproduced in Figure 1.3. The figure shows a series of concentric circles. Due to the aberrations of the eye, some distortion will be seen in the image. This distortion pattern can be seen to fluctuate in time, and tends to be more noticeable at particular viewing distances. These fluctuations are related to the fluctuations in ocular aberrations, and occur with corresponding frequencies [7]. The causes of temporal changes in aberrations remain an open area of debate. It is known that the eye's focus generally fluctuates about its mean with amplitudes of $0.03 - 0.5$ D [27]. Though microfluctuations in accommodation are responsible for a proportion of this, they cannot explain the full amount. In particular, correlations between mean accommodative level and Zernike aberrations have been found [28]. The relationship between accommodation level and aberrations will be discussed further in Chapter 4. Hofer et al. [15] suggested several reasons for the fluctuations in ocular aberrations, including rotation of the eyes due to movements (drift, saccades, microtremor), misalignments due to instability of the head position during measurements, changes in tear-film thickness, and the influence of the heartbeat. The frequency range of the dynamics have been reported by several authors. While measurable power in fluctuations of defocus up to 5 Hz had been reported in the 1980s [27], more recent studies have suggested that temporal fluctuations of aberrations may have significant power up to 70 Hz or above [4].

The particular influence of the tear-film and its breakup on the dynamics of aberrations has attracted independent studies [29, 30], and it has been found that wavefront variance attributed to the tear film is significant when compared to the overall
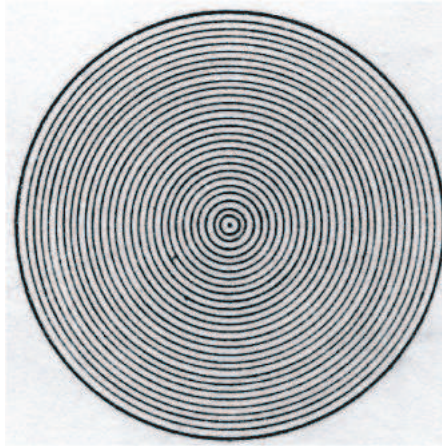
Figure 1.3: Helmholtz's viewing chart to demonstrate fluctuations in aberrations of the human eye. The phenomenon is generally best viewed with one eye, and with the target held at a steady distance within the subject's accommodative range. The time-varying distortions that can be seen are the result of the time-varying aberrations of the eye, and occur on corresponding time-scales.

wavefront variance induced by dynamic changes in aberrations. The influence of the cardiopulmonary system has also attracted interest in recent years. An early study by Winn et al. [31] found correlations between the arterial pulse and the frequency component of greatest amplitude found in the defocus signal (typically 1-2 Hz). This suggests significant influence of the pulse on ocular dynamics. Other studies have shown a further correlation between the instantaneous heart-rate (which is related to respiration) and a lower frequency defocus component (<0.6 Hz). The ocular pulse itself has been shown to cause changes in the axial length of the eye of approximately 3-5 μm [32]. Other studies used a combination of cross-correlation and coherence analysis to show that the influence of the cardiopulmonary system is apparent not only in the defocus signal, but in higher-order aberrations as well [18, 33]. Zhu et al. [18] suggested that the mechanisms linking the fluctuations of aberrations with heart-rate are likely to be the same as for fluctuations in accommodation, and that the origin of all these fluctuations may reflect changes in the lens shape or position due to blood flow or related changes in intraocular pressure. The authors noted that the correspondence was larger for the higher-order aberrations than for lower-order aberrations in some cases. However, it should be noted that correlations between certain pairs of Zernike modes are also known to exist [17]. These correlations may simply reflect the balancing of modes in the Zernike expansion rather than a physi-cally significant relationship [18]. Iskander et al. [16] presented analysis using a set of

tools that had not previously been used for dynamic aberrations of the eye, including a sophisticated method for removal of measurement artifacts and a time-frequency expansion. This subject will be treated in more depth in Chapter 3.

1.3 Ocular Accommodation

It was first demonstrated by Scheiner in 1619 that the human eye changes its refractive power when we focus at near objects [34]. However it was not until 1801 that this change in power was shown by Thomas Young to be due to the lens [1]. He concluded this in his Bakerian lecture on the mechanism of the eye by demonstrating that accommodation was not due to changes in corneal curvature or the axial length of the eye, and thus the lens was the only alternative [10].

The classical theory of accommodation is attributed to Helmholtz [2]. This theory describes how the zonular fibres, ciliary muscles, and the lens (see Figure 1.1) interact during accommodation. When the ciliary muscles are in a relaxed state, the zonular tension holds the lens (which is enclosed in a collagen capsule) in a comparatively flattened state. This is referred to as the relaxed or unaccommodated state of the eye. The contraction of the ciliary muscles leads to reduction in the zonular tension. This in turn leads to a change in shape of the lens, which becomes more spherical and therefore increases its optical power. This increased state of optical power is desirable for viewing near objects. An alternative theory of the accommodative mechanism was proposed by Schachar [35], in which the author states that contraction of the ciliary muscles leads to a stretching force along the equatorial zonular fibres, and it is this stretching force that increases the equatorial diameter of the lens. This in turn is said to cause the anterior and posterior surfaces to increase in curvature, giving the lens increased optical power. However, this theory is at odds with other studies that suggest the equatorial diameter of the lens in fact decreases during accommodation [10]. Presbyopia is the term used to describe the condition whereby the accommodative ability of the eye diminishes with age. The amplitude of accommodation that a person is capable of declines naturally starting from childhood, and around the age of 40-50 years it typically falls to a minimal level. There have been many population studies of the onset and prevalence of presbyopia, utilising both subjective and objective methods [10]. Some include empirical models of the relationship between accommodative amplitude and age, such as the study by Ungerer [36], which fitted a quadratic regression model to measured data. The physiological explanation of presbyopia is not universally agreed upon, however most theories involve some changes
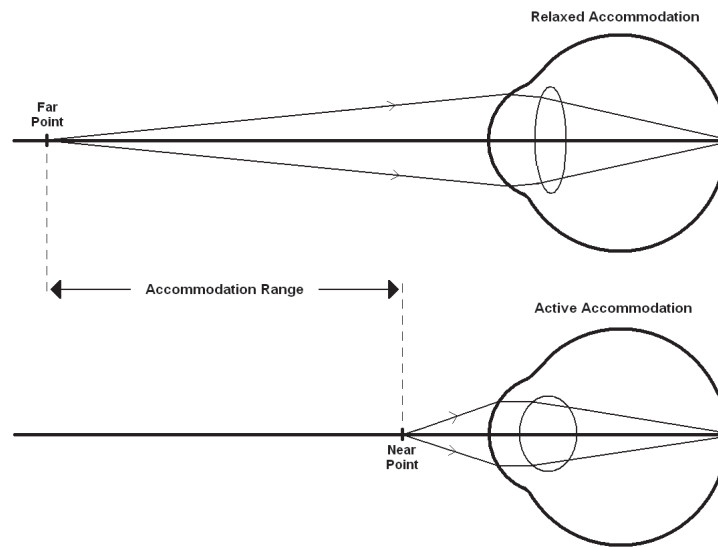
Figure 1.4: Illustration of the difference between the relaxed and accommodating states of the (non-presbyopic) eye. Note that this case represents a myopic eye, as the far point is defined on the optical axis. For an emmetropic eye, the far point is at infinity, and for hypermetropia it is behind the eye.

in the lens due to age, for example, hardening of the lens itself. A description of some of the different theories of accommodation is given by Atchison and Smith [9]. When conducting a study of accommodation involving several subjects, it is inevitable in practice that there will be some variation in their respective accommodative amplitudes. However, by limiting the age range of the subjects, one can assemble a sample that have amplitudes that are at least comparable (e.g., within 1-2 D of each other). In this thesis, we will sometimes refer to "young, healthy subjects". In the context of accommodation, this can be taken to refer to subjects who do not exhibit an advanced stage of presbyopia, or any known accommodative irregularities.

The spherical refractive error of the eye is an important consideration when conducting studies on aberrations or accommodation. The three common spherical refractive conditions are known as myopia (short sight), hypermetropia, and emmetropia ("normal" sight). To better understand how these conditions impact on vision, we will refer to the *far point* and *near point* of the eye. These points define the range of clear vision, and are illustrated (for a myopic eye) in Figure 1.4. When the accommodative system is not active (i.e., the ciliary muscles are fully relaxed), the eye is said to be focused on the far point, which is then conjugate to the retina. When the maximum amplitude of accommodation is being used, the eye is said to be focused on the near point (this

also means that the eye has its greatest possible refractive power. In an emmetropic eye, the far point is considered to be at infinity. In practice, such a situation is impractical to measure and so instead an eye with a far point of 4 m or more away can be considered to be emmetropic [9]. For hypermetropia, the far point lies behind the eye. Hypermetropic subjects may be able to view distant objects clearly by accommodating, however. For myopic eyes, the far point lies a finite distance in front of the eye. The near point for a young, healthy myopic or emmetropic subject is typically a short distance in front of the eye. To determine the *amplitude of accommodation*, one can simply measure the difference in vergence between the near point and far point [9]. For example, consider a subject whose near point is 0.2 m from the eye, and whose far point is at 1.25 m. The corresponding vergence in dioptres is given by the reciprocal of the distance, therefore the near point and far point vergences are 5 D and 0.8 D respectively. The amplitude of accommodation is given by the difference between the two, i.e., 4.2 D.

Accommodation is a dynamic process. As noted in the previous section, the microfluctuations of accommodation play an important part in the variability of the optical quality of the eye. Thus, these microfluctuations have attracted much study. Early work carried out by Campbell et al. [37] characterised the main features of the commonly recorded accommodation signal: a low frequency component (<0.5 Hz), which corresponds to the drift in the accommodation response, and a peak at higher frequency, usually observed in the 1-2 Hz band. This frequency composition was confirmed in later studies [27,38,39].

An area of continued debate is the possible roles that microfluctuations play in the function of accommodation, and the question of whether they are involved in the accommodative control system. It is clear that under steady-state conditions, a fluctuation in one direction tends to improve the image focus, while a fluctuation in the other direction makes it worse. This has led to the suggestion that the fluctuations could serve as a simple odd-error cue to optimise or "fine-tune" the initial accommodative response to a stimulus [40]. A review by Charman [27] found it unlikely that the microfluctuations play any role in guiding the initial response to a change in accommodative stimulus (which is normally characterised by a 0.36-0.4 s reaction time and a total response time of about 1 s [41]). The review identified three possible roles for the microfluctuations about a steady-state level:

- They could be intrinsically related to the accommodative control system, with characteristics that change according to the viewing conditions in order to opti-

mise performance.

- They could have characteristics that are independent of the control system, but still provide cues that assist control.

- They could simply represent state-dependent noise, and have no input to the control system.

Most authors, when referring to the frequency composition of the microfluctuations, distinguish between a low frequency (<0.5 Hz) band and a higher frequency band (1-2 Hz). Many of the researchers involved in these studies assert that the high frequency components are thus more likely to be a mechanical property of the accommodation system, rather than the response of a closed-loop system [27, 39]. In particular, it is known that much of the high frequency band can be attributed solely to the lens, as far less high frequency activity is seen in aphakic[1] subjects [31]. The relationship of the microfluctuations to the mean response of the accommodative system is of primary interest, because the physical nature of the process changes depending on the level of accommodative effort. Several authors have reported that the amplitude of the high frequency component increases with the target vergence [15, 28, 42, 43]. However, a study by Miege et al. [38], shows data obtained on two subjects for which the high frequency component (around 2 Hz) decreased when the target was brought closer than 5 D. This was attributed to the subjects having to accommodate at the upper limit of their range. In Chapter 4 we will investigate thoroughly the effect of accommodative effort on the dynamics of accommodative response.

There has also been debate as to whether the lower frequency microfluctuations have a role in the control of accommodation. The low frequencies are too slow to assist the dynamic response to a stimulus change in accommodation, however this does not rule out the possibility that they may assist the steady-state response. Another of Campbell's results was that the low frequency component is increased when the depth of field of the subject's seeing is increased. This was backed up by later work, and Charman's review summarised in detail the changes in measurements of this low frequency component depending on various viewing conditions [27]. These include pupil size [39, 44], luminance level [40, 44], contrast level [27], and mean accommodative response [4, 38]. It has been suggested that the slow drifts in the accommodation signal could play an active role as part of "accommodation correction cycles" [45].

An alternative functional role for the microfluctuations in accommodation was put

---

[1]Aphakia is the absence of the lens of the eye, usually due to surgical removal.

forward by Crane [46]. The author suggested that the microfluctuations could serve to improve the eye's depth of focus. If the microfluctuations do play a useful role, then intuitively it would follow that they should produce a detectable change in the retinal image. This was addressed in the original study by Campbell et al. [37], who found that sensitivity to the fluctuations was dependent on the mean accommodative level. The authors concluded however, that changes in the retinal image due to the microfluctuations (which they found to have an amplitude of about 0.2 D) could be detectable at least under certain conditions.

Kotulak et al. [43] proposed that accommodation may be able to respond to changes below the detectable threshold in the image. The authors were able to find accommodative responses with stimulus changes of as low as 0.12 D. In a subsequent work, the same authors also proposed that the accommodative control system could utilise information about both accommodation level and retinal image contrast to influence its output [47]. A study by Winn et al. [48] found that the RMS of typical accommodation microfluctuations was comparable to the threshold of blur perception under cycloplegia[2], and therefore could be detectable by a normal observer. Because portions of the accommodation signal were found to exceed the eye's depth of focus, the authors concluded that microfluctuations of accommodation are capable of providing information to control accommodation without the need for an additional mechanism. It is therefore possible that microfluctuations of accommodation are solely responsible for controlling the response to very small changes in the accommodative stimulus. The measurement, analysis, and interpretation of the microfluctuations of accommodation will be investigated in detail in Chapter 4.

---

[2]Cycloplegia is paralysis of the ciliary muscle of the eye, resulting in a loss of accommodative ability.

Chapter 2

Mathematical Background

The application of scientific and engineering principles to the study of biological and medical information has long been a distinct field of life science. Before the advent of modern digital computing, much of the interpretation of this data had to be performed by human inspection, for example, by medical professionals. This type of "manual" processing was severely limited in both accuracy and the number of different features that could be reliably extracted from measured data. Advances in sensing technology mean that large varieties and quantities of biological and medical data are now more readily available. Techniques that involve the application of mathematical approaches to interpret this data and extract diagnostic information is referred to as *biological* or *biomedical information processing* [49]. When the information in question takes the form of measured electrical signals, such as in electrocardiography (ECG) or electroencephalography (EEG), the term *biomedical signal processing* is often used. These concepts are at the core of the field of biomedical engineering.

The rationale behind any signal processing is typically either (i) to extract a priori information from the signal; or (ii) to interpret the nature of a physical process from which the signal arises, based on the signal's characteristics and/or how changes in the process affect these characteristics [50]. The latter forms the motivation behind much of the signal processing carried out in this research. We will employ some classical methods in signal processing such as spectral analysis. We will also utilise methods of *statistical signal processing*, which involves the treatment of signals as stochastic processes (containing both deterministic and stochastic components). In this chapter

17

we will introduce the mathematical and statistical tools that are central to the analysis presented later in the thesis. Papoulis (1991) [51] is a useful text regarding stochastic processes and is referred to throughout the chapter.

2.1 Stochastic Processes, Time Series, and Signals

Throughout the course of the thesis we will frequently deal with stochastic processes, time series, and signals, depending on whichever term is most appropriate to the situation. A *stochastic process* is a continuous or discrete sequence of random variables in time and/or space. Suppose an experiment has a number of possible outcomes i defined in a sample space S. With each possible outcome, we associate a function $x(t, \eta)$. A particular outcome leads to a different function $x(t)$, which we refer to as a *realisation* of the process x. The set of all possible realisations is known as the *ensemble* [52]. For a discrete stochastic process, t belongs to some set T, which can be for example a point in time, a point in space, or a space-time vector. A *time series* refers to a special case of a stochastic process where T represents only time. Typically, data points in a time series are uniformly spaced, e.g., $T = 1, 2, 3, \ldots$. Time series and time series models are often used to analyse and describe real processes, and to allow the prediction of future values of the process (known as *forecasting*) [53]. In the general sense, the term *signal* refers to a single-valued representation of information as a function of an independent variable (e.g., time or space). For physical processes, a signal (either continuous or discrete) typically represents a measure of some form of energy produced by the process [50]. Signals may be real or complex, and can be a function of more than one variable. In this thesis, all uses of the term "signal" refer to real-valued, scalar functions of time. The physical meaning of each stochastic process, time series, or signal will be be described as each is introduced in the text, and the terms will be used interchangeably in certain situations where it is considered appropriate.

2.1.1 Statistics of Stochastic Processes

Distribution and Density Functions

To understand the statistics of a random process, we can examine its first-order statistics. That is to say, we examine the random variable $x(t)$ at a particular value of t. The

cumulative distribution function (CDF) of this random variable is given by:

$$F(x,t) = P(x(t) \leq x) \tag{2.1}$$

where F denotes the CDF and P refers to the probability operator. The *probability density function* (PDF), denoted f, can be defined as the derivative of the CDF [52]:

$$f(x,t) = \frac{\partial F(x,t)}{\partial x} \tag{2.2}$$

Note that $f(x,t)$ is positive valued and normalised, i.e. the conditions $f(x,t) \geq 0$ and $\int_{-\infty}^{\infty} f(x,t)dx = 1$ must be satisfied for the PDF to be valid.

First and Second-Order Properties

To completely describe the first and second-order properties of a stochastic process, knowledge of the nth order joint distribution function $F(x_1, x_2, \ldots, x_n; t_1, t_2, \ldots, t_n)$ is required. This quantity is not of much practical use however [52], so we instead make use of the expected value, autocorrelation function, and autocovariance function.

The mean of $x(t)$ is the *expected value* of the random variable $x(t)$:

$$E\{x(t)\} = \langle x(t) \rangle = \int_{-\infty}^{\infty} x(t)f(x,t)dx \tag{2.3}$$

The *autocorrelation* $R_{xx}(t_1, t_2)$ of a real-valued process $x(t)$ is defined as the expected value of the product $x(t_1)x(t_2)$, i.e.

$$R_{xx}(t_1, t_2) = \langle x(t_1)x(t_2) \rangle \tag{2.4}$$

The *autocovariance* $C_{xx}(t_1, t_2)$ can then be defined by

$$C_{xx}(t_1, t_2) = R_{xx}(t_1, t_2) - \langle x(t_1) \rangle \langle x(t_2) \rangle \tag{2.5}$$

It is sometimes useful to refer to the *correlation coefficient* $r_{xx}(t_1, t_2)$, particularly when one wishes to use correlation to interpret the strength of linear relationship between two random variables. It is defined as:

$$r_{xx}(t_1, t_2) = \frac{C_{xx}(t_1, t_2)}{\sqrt{C_{xx}(t_1, t_1)C_{xx}(t_2, t_2)}} \tag{2.6}$$

Note that $\sigma^2(t,t) = C_{xx}(t,t)$ gives the variance of the process. For a complex random

process $z(t) = x(t) + iy(t)$, the autocorrelation function is given by

$$R_{xx}(t_1, t_2) = \langle z(t_1) z^*(t_2) \rangle \tag{2.7}$$

If two processes $x(t)$ and $y(t)$ are under consideration, the *cross-correlation function* is

$$R_{xy}(t_1, t_2) = \langle x(t_1) y^*(t_2) \rangle \tag{2.8}$$

2.1.2 Stationarity and Ergodicity

A stochastic process $x(t)$ is said to be *strictly stationary* if its statistical properties are invariant to a shift in the time origin. This means that the processes $x(t)$ and $x(t + \tau)$ have the same statistical properties for any value of τ. The definition requires that all n-point probability density functions are the same, regardless of time or position. This implies that

$$f(x_1, x_2, \ldots, x_n; t_1, t_2, \ldots, t_n) = f(x_1, x_2, \ldots, x_n; t_1 + \tau, t_2 + \tau, \ldots, t_n + \tau) \tag{2.9}$$

and so the probability density function of the process is invariant to a time origin shift. Thus, we can conclude that the PDF is independent of t altogether, i.e.

$$f(x, t) = f(x) \tag{2.10}$$

A process $x(t)$ is deemed to be *wide-sense stationary* (WSS) if its expected value $\langle x(t) \rangle$ is a constant and its autocorrelation function depends only on $\tau = t_1 - t_2$, i.e.

$$R_{xx}(t_1, t_2) = R_{xx}(\tau) = \langle x(t + \tau) x^*(t) \rangle \tag{2.11}$$

A useful property in this case is

$$\left\langle |x(t)|^2 \right\rangle = R_{xx}(0) \tag{2.12}$$

which shows that the average power of a WSS process is independent of t. It should be noted that although a strictly stationary process is also WSS, the converse is not necessarily true. The value τ is often known as the *lag* parameter. It follows from Eq. 2.11 that the autocovariance of a WSS process also depends only on τ:

$$C_{xx}(\tau) = R_{xx}(\tau) - \langle x(t) \rangle^2 \tag{2.13}$$

The correlation coefficient in this case is given by

$$r_{xx}(\tau) = \frac{C_{xx}(\tau)}{C_{xx}(0)} \tag{2.14}$$

Finally, if a WSS stochastic process $x(t)$ has the property $C_{xx}(\tau) = 0$ for $|\tau| > \tau_c$, the constant τ_c can be referred to as the *correlation time* of the process. It is defined as:

$$\tau_c = \frac{1}{C_{xx}(0)} \int_0^\infty C_{xx}(\tau) d\tau \tag{2.15}$$

Other Forms of Stationarity

A stochastic process $x(t)$ is sometimes referred to as *asymptotically stationary* if the n-point joint PDF $f(x_1, x_2, \ldots, x_n; t_1 + \tau, x_2 + \tau, \ldots, x_n + \tau)$ is independent of τ for large values of τ.

The term *stationary in an interval* or *quasi-stationary* can be used to refer to a process that is stationary within a limited range on t. *Cyclostationarity* refers to the case where statistical properties are invariant to a shift in the origin by integer multiples m of a certain period T. In this case, we can rewrite Eq. 2.9 as

$$f(x_1, x_2, \ldots, x_n; t_1, t_2, \ldots, t_n) = f(x_1, x_2, \ldots, x_n; t_1 + mT, t_2 + mT, \ldots, t_n + mT) \tag{2.16}$$

A process is said to be *stationary in the increments* if its increments form a stationary process. Finding the increments of a discrete process is known as *differencing*, which is analogous to differentiation for a continuous process. In some cases, the differencing operation may have to be performed several times to yield a stationary result [53]. Differencing will be discussed in more detail later in this chapter.

Ergodicity

At the beginning of this section, we associated a function $x(t, \eta)$ with a particular outcome η of a stochastic process, each outcome yielding a different $x(t)$, i.e., a different realisation of the process, where the set of all possible realisations is termed the ensemble. If N is the number of all possible realisations, the *ensemble average* can be written as

$$\mu(t) = \frac{1}{N} \sum_{i=1}^{N} x(t, \eta_i) \tag{2.17}$$

In many real-life applications, only a single realisation of the process is available. If the process is *ergodic*, we can still obtain an estimate of μ by using the time average of this single realisation. We form the time average $\mu_t = \hat{\mu}$ as follows:

$$\mu_t = \frac{1}{2T} \int_{-T}^{T} x(t)dt \tag{2.18}$$

If $x(t)$ is an ergodic process, μ_t will converge to μ as the length of the available realisation approaches infinity. In this manner, for an ergodic process one may exchange ensemble averages with time averages. An ergodic process must be stationary, but the converse is not necessarily true [51].

Testing for Stationarity in a Time Series

Though stationarity of a time series can be informally investigated by visual inspection [54], it is sometimes useful to test a given time series or signal to assess whether or not it is stationary. In general, it is not possible to test rigorously for strict stationarity, and so we instead focus on assessing wide-sense stationarity.

There are two general approaches to testing for stationarity - parametric and non-parametric. Parametric approaches typically involve the derivation of a parametric model of the time series, e.g., a time-varying ARMA model [55, 56]. This type of modelling approach is addressed further in Chapter 5. On obtaining such a model, one can track the changes in the system parameters over time to assess non-stationary behaviour. This typically requires making certain assumptions about the nature of the data e.g. that it has a Gaussian distribution. Non-parametric methods do not require the same assumptions [57]. These methods are generally based on the idea that one can look for stationarity (or lack thereof) in a given time series by computing one or more statistical measures over a moving time window [58].

The first step in performing a non-parametric test to check for stationarity is to choose a statistical property that the test will be based upon. For example, the **mean** of the time series can be tracked from one time window to another. If the value of the mean varies significantly, one may conclude that there is a wandering baseline or low-frequency component (possibly an artifact) present. This is common in biomedical signals such as ECG; however in many such applications a high-pass filter is employed to block these effects. Therefore, variation in the mean of the time series alone may not have consequences for the type of analysis being performed. The **variance** of non-stationary processes can also change significantly when examined over short

periods. This is a common feature of speech signals, and is symptomatic of systems that have time-varying filtering characteristics [58]. As stated in Eq. 2.11, for a process to be WSS, its **autocorrelation function** must be independent of shift in the time origin. The autocorrelation function for a non-stationary time series should vary when computed over different time windows.

The *runs test* is a simple method to ascertain time-invariance of statistical measures of a time series, and is used in such fields as econometrics [59], biomedical signal analysis [50], and electrical engineering [54]. A time series of length N is first divided into k non-overlapping segments. The statistic of interest, for example the sample variance, is calculated for each segment and denoted p_i where i is the index of the segment. The median value of p (denoted p_{med}) is found and removed from each p, yielding a sequence of values $q_i = p_i - p_{med}$. The number of changes in sign in this sequence is then found. This value plus one gives the *number of runs* for the test. Lessard [59] gives a table of acceptable bounds on the number of runs for a stationary random process, assuming certain confidence intervals. One can consult this table and if the test result for the number of runs does not fall within these bounds, the hypothesis of stationarity is rejected. As with all hypothesis tests, the runs test has limited power in that at best it can only enable one to *reject* a hypothesis of stationarity based on statistical significance. The performance of the test ultimately is dependent on the subjective selection of the test statistic and the segment size k.

2.1.3 Non-Stationary Processes

It can be said that conventional analysis of time series and signals is heavily dependent on stationarity. The reason why stationarity is such an attractive property is that it attaches a condition of "statistical stability" to a process. In practical situations however, the assumption of stationarity is usually an approximation. When non-stationarity becomes significant to the point that conventional analysis is rendered inadequate, we are required to relax this assumption. If we simply drop the concept of stationarity completely, there is very little we can say about a particular process. Instead, in many cases we replace the assumption of stationarity by a more general notion that still allows us to carry out meaningful analysis [60]. Thus, when we are presented with a non-stationary process for which an assumption of strict or wide sense stationarity is not feasible, we must first assess what "type" of non-stationary process it is.

A non-stationary process can be thought of as one which arises from a *time-variant*

system, i.e., a system with parameters that vary in time [58]. One of the simplest forms of non-stationary process occurs in the situation where the observed process $x(t)$ is the sum of a deterministic function $\psi(t)$ and a zero-mean stationary process $v(t)$:

$$x(t) = \psi(t) + v(t) \tag{2.19}$$

The function $\psi(t)$ can be thought of as a "trend", which allows the mean of the process $\langle x(t) \rangle$ to vary over time. For example, $\psi(t)$ could impose a steady growth or an oscillation corresponding to seasonal behaviour. This particular type of non-stationary process could be analysed by estimating the deterministic function $\psi(t)$, subtracting it from the time series, and then analysing the remainder as a stationary process. It may also be possible to remove the trend by *differencing*. The dth order difference Δ^d for a discrete time series $x(k)$ can be written as:

$$\Delta^d x(k) = \sum_{k=0}^{d} \binom{d}{k} (-1)^{d-k} x(n+k) \tag{2.20}$$

The order of differencing d required to render the time series stationary depends on the characteristics of the particular process [53]. If the non-stationarity in the series takes the form of "shifts" in the mean, then one order of differencing will typically suffice to remove the non-stationarity. A process with variations in local slope or a more complicated structure is more likely to require additional differencing.

Box and Jenkins [53] showed that autoregressive models with certain choices of parameters can generate non-stationary processes. Autoregressive processes will be described in more detail in Section 2.4. The non-stationary behaviour produced by this class of model is of a special type, which is referred to as "explosive behaviour" by Priestley [60]. Though the second-order properties of the process vary over time, the evolution of the process is completely determined by the model parameters. Therefore, the time series generated by such models are to a certain degree homogeneous, even if they do meet the criteria for non-stationarity. This may be an unnatural restriction if one's ultimate goal is the analysis and modelling of non-stationary processes whose statistical properties vary in an arbitrary manner over time. It would seem a natural progression to consider parametric models whose parameters can vary arbitrarily. This approach has been adopted by several authors [58, 60–62], and will be discussed further in the coming sections.

2.2 Frequency Domain Analysis

2.2.1 Power Spectrum

The *power spectrum* or *power spectral density* (PSD) describes how the power of a signal or time series is distributed with frequency. The Wiener-Khinchin theorem states that the power spectrum (denoted P) of a WSS process $x(t)$ is the Fourier transform of its autocorrelation function:

$$P_{xx}(\omega) = \mathcal{F}\{R_{xx}(\tau)\} = \int_{-\infty}^{\infty} R_{xx}(\tau)e^{-i\omega t}d\tau \tag{2.21}$$

where ω is the angular frequency. Though $x(t)$ may be real or complex, $P_{xx}(\omega)$ is a positive real function of ω, since $R_{xx}(-\tau) = R_{xx}^*(\tau)$. If we consider a discrete time series $x(n)$, we must rewrite the above definition, based on a discrete representation of the autocorrelation function $R_{xx}(m)$, where m is the sample lag. In this case, the power spectrum is defined as:

$$P_{xx}(\omega) = \sum_{m=-\infty}^{\infty} R_{xx}(m)e^{-i\omega m} \tag{2.22}$$

Note that in this case $P_{xx}(\omega)$ is the discrete time Fourier transform (DFT) of $R_{xx}(m)$.

In practical applications involving stochastic processes, only a finite portion of the signal or time series is available, and thus we cannot fully stipulate $R_{xx}(m)$. For a signal of length N (in samples), $R(m)$ is defined for $-(N-1) < m < (N-1)$. We must instead estimate the power spectrum, a technique commonly known as *spectral estimation*. There are two general approaches to spectral estimation: parametric and non-parametric. Parametric spectral estimation involves modelling the signal as the output of a filter, such that values of the autocorrelation for $|m| \geq N-1$ can be extrapolated and used to estimate the filter coefficients. This is particularly useful in situations where little data is available i.e. N is small. Non-parametric methods of spectral estimation are implemented directly on the signal and do not require model parameters to be estimated. These methods are limited by the fact that they are performed on a *windowed* autocorrelation sequence i.e. the autocorrelation function is assumed to be zero for $|m| \geq N-1$. In many cases, $R_{xx}(m)$ is very small for large values of m, and so non-parametric methods can lend themselves well to larger amounts of data. In this thesis we generally have large N, and thus we will employ mainly non-parametric methods of spectral estimation.

The *periodogram* is a method widely used in non-parametric spectral analysis. Consider a time series $x(n)$ of finite length N. We attempt to obtain an estimate of $P(\omega)$. From Eq. 2.22 it is clear that we first need to estimate $R_{xx}(m)$ based on available data. An estimate is obtained via:

$$\hat{R}_{xx}(m) = \frac{1}{N - |m|} \sum_{n=0}^{N-1-|m|} x^*(n)x(n+m) \tag{2.23}$$

where $m = 0, 1, 2, \ldots, N - 1$. An estimate of the power spectrum (called the periodogram) can be obtained via:

$$\hat{P}_{xx}(\omega) = \frac{1}{N} \left| \sum_{n=0}^{N-1} x(n)e^{-in\omega} \right|^2 \tag{2.24}$$

This method is typically implemented on a computer using the fast Fourier transform (FFT). It should be noted that

$$\lim_{N \to \infty} \langle \hat{P}_{xx}(\omega) \rangle = P_{xx}(\omega) \tag{2.25}$$

and so the expected value of the power spectrum estimate converges to the true spectrum as the length of the time series increases. However, the variance of the power spectrum does not converge to zero with increasing N[1], and so the periodogram is not a consistent estimate of the PSD [63]. The variance of the periodogram can be reduced by averaging a number of statistically independent estimates. This can be performed using estimates based on different observations of the time series. If only a single realisation is available, the time series can be divided into segments and an estimate of the PSD can be performed on each and then averaged. This procedure is commonly known as Bartlett's Method [58], and can be implemented as follows:

$$\hat{P}_{B,xx}(\omega) = \frac{1}{N} \sum_{j=0}^{K-1} \left| \sum_{n=0}^{L-1} x(n+jL)e^{-in\omega} \right|^2 \tag{2.26}$$

where $K = N/L$ is the number of segments used. This modification reduces the variance of the periodogram by a factor of $1/K$ in exchange for a loss in resolution. A further reduction in variance can be achieved by allowing the segments to overlap. This modification is known as Welch's Method, and the periodogram in this case is

---

[1] In fact, $Var\left(\hat{P}_{xx}(\omega)\right) \approx P_{xx}^2(\omega)$ for large N [51].

given by:

$$\hat{P}_{W,xx}(\omega) = \frac{1}{KL} \sum_{j=0}^{K-1} \left| \sum_{n=0}^{L-1} x(n+jD)e^{-in\omega} \right|^2 \tag{2.27}$$

where $D = (N+L)/(K-1)$. The periodogram can also be smoothed by "windowing" the time series with a window function $w(n)$ of length N. Windowing also serves to reduce *spectral leakage*, an artifact resulting from the use of a finite length time series in the Fourier transform calculation. Using a window function, Eq. 2.24 is rewritten as follows:

$$\hat{P}_{w,xx}(\omega) = \frac{1}{NU} \left| \sum_{n=0}^{N-1} x(n)w(n)e^{-in\omega} \right|^2 \tag{2.28}$$

where

$$U = \frac{1}{N} \left| \sum_{n=0}^{N-1} w(n) \right|^2 \tag{2.29}$$

The choice of window function is typically made depending on the particular requirements (e.g., in resolution). A table of window functions and their properties is given by Bruce pg. 252 [50].

Cross-Spectral Density

For two jointly stationary processes $x(t)$ and $y(t)$, one can define the *cross-spectral density P_{xy}* as the Fourier transform of their cross-correlation function:

$$P_{xy}(\omega) = \mathcal{F}\{R_{xy}(\tau)\} = \int_{-\infty}^{\infty} R_{xy}(\tau)e^{-i\omega t}d\tau \tag{2.30}$$

2.2.2 Least-Squares Spectral Analysis

Least squares spectral analysis (LSSA) refers to a method of spectral estimation that employs least squares fitting of sinusoids to time series. It is sometimes referred to as the Vaníček method, after the author who first described it in detail [64]. It has many similarities to Fourier-based spectral estimation [65, 66], but has several properties that make it preferable to these methods in certain circumstances. The principle of the method is that a discrete time series can be represented by a weighted sum of sinusoids. Though the sinusoidal frequencies can be chosen arbitrarily, one can improve the fit by choosing frequencies that minimise the residual error after fitting. The number of sinusoids used must be less than or equal to the number of data samples [67]. One of the most attractive features of this method is that it can be ap-

plied to non-uniformly sampled signals, such as discrete signals with missing data points, whereas Fourier-based methods generally only apply to continuous signals or discrete signals with evenly spaced data points [68]. In fact, the least squares spectrum can be considered to be a natural extension of Fourier methods to non-uniform series [65, 69]. The potential advantage of LSSA in the low-frequency range is particularly noticeable [64].

The method proposed by Vaniček was subsequently simplified by Lomb [65]. Scargle [66] showed that Lomb's method was akin to a modification of the definition of the classic periodogram for unevenly sampled signals. This "modified periodogram" is commonly known as the Lomb-Scargle periodogram [69], and is defined as:

$$\hat{P}_{LS,xx}(\omega) = \frac{1}{2} \left\{ \frac{\left[\sum_k x(k) \cos \omega \left(t(k) - \tau \right) \right]^2}{\sum_k x(k) \cos^2 \omega \left(t(k) - \tau \right)} + \frac{\left[\sum_k x(k) \sin \omega \left(t(k) - \tau \right) \right]^2}{\sum_k x(k) \sin^2 \omega \left(t(k) - \tau \right)} \right\} \qquad (2.31)$$

where $x(k)$ is the value of the kth data point, and τ is defined by

$$\tan(2\omega\tau) = \frac{\sum_k \sin 2\omega t(k)}{\sum_k \cos 2\omega t(k)} \qquad (2.32)$$

It was shown by Scargle that this periodogram (given certain modifications) is in fact equivalent to Vaniček's original least squares method. A comprehensive analysis of the statistical properties of the Lomb-Scargle periodogram and a comparison to the DFT-based periodogram were also given by the author [66].

2.2.3 Time-Frequency Analysis

Non-stationary processes emerge from systems whose parameters vary in time, and thus the frequency content of these processes is not constant. Fourier-based spectra have zero time resolution; they give us information about *what* frequencies existed throughout the entire duration of the signal, but not *when* they existed. Consequently for non-stationary processes, the power spectrum as we have treated it up until now is of limited interest [51]. For processes of this type, any form of "spectrum" must be allowed to become time-dependent, regardless of how it is defined.

The *time-bandwidth relation* is an important consideration in time-frequency analysis [58]. Consider a signal $x(t)$, with frequency domain representation $X(\omega)$. The instantaneous energy $\mathcal{E}$ is sometimes defined as $\mathcal{E}(t) = |x(t)|^2$, or in the frequency domain as $\mathcal{E}(\omega) = |X(\omega)|^2$. The two representations can be related by the classical

Fourier transform:

$$X(\omega) = \frac{1}{\sqrt{2\pi}} \int_{-\infty}^{\infty} x(t)e^{-i\omega t}dt \tag{2.33}$$

Thus, $|x(t)|^2$ and $|X(\omega)|^2$ cannot be changed independently [70]. The time-bandwidth relation for all signals can be stated as

$$\Delta t \Delta \omega \geq \frac{1}{2} \tag{2.34}$$

This inequality is sometimes described as an "uncertainty principle" [58,62,70], however it should be noted that this does not refer to uncertainty in measurement. Rather, it is a result imposing that both the time *and* frequency resolution of a particular signal cannot be arbitrarily small at once.

For a non-stationary signal, obtaining representations of $\mathcal{E}(t)$ and $\mathcal{E}(\omega)$ may not give sufficient information. The general aim of time-frequency analysis is to obtain some joint distribution $\mathcal{W}(t,\omega)$, which represents the instantaneous energy in both time and frequency [70]. The total energy is then given by

$$\int \int \mathcal{W}(t,\omega)dtd\omega = \int |x(t)|^2 dt = \int |X(\omega)|^2 d\omega \tag{2.35}$$

The corresponding marginal distributions of time and frequency are

$$\mathcal{W}_t(t) = \int \mathcal{W}(t,\omega)d\omega = |x(t)|^2 \tag{2.36}$$

and

$$\mathcal{W}_\omega(\omega) = \int \mathcal{W}(t,\omega)dt = |X(\omega)|^2 \tag{2.37}$$

The Short-Time Fourier Transform

Perhaps the simplest and most intuitive method for performing time-frequency analysis is the short-time Fourier transform (STFT). The basic principle is that the signal under examination $x(t)$ is split into segments, and then Fourier analysis is performed on each segment in turn. The STFT is given by

$$X(\tau,\omega) = \frac{1}{\sqrt{2\pi}} \int_{-\infty}^{\infty} x(t)w(t-\tau)e^{-i\omega t}dt \tag{2.38}$$

where $w(t)$ is a window function centred around zero, with τ being known as the *running time* (effectively a lower resolution version of time t). The magnitude squared

of the resultant spectrum $X(\tau, \omega)$ is known as a *spectrogram* i.e.

$$\mathcal{W}_{STFT,xx} = |X(\tau, \omega)|^2 \tag{2.39}$$

Note that the spectrogram is a function of τ rather than t. The resolution of the spectrogram is dependent on the size of the window function, as well as the type of window function (often a Gaussian or Hann window) used. For a discrete signal $x(n)$, the STFT can be calculated as follows:

$$\mathcal{W}_{STFT,xx} = |X(m, \omega)|^2 = \left| \sum_{n=-\infty}^{\infty} x(n)w(n-m)e^{-i\omega n} \right|^2 \tag{2.40}$$

where $w(n)$ is the discrete version of the window function. The simple nature of the STFT makes it easy to implement and interpret, however it has inherent disadvantages. The most apparent is the necessary trade-off between time and frequency resolution [58]. It should be noted that in the case of the STFT, this trade-off is artificially imposed due to the introduction of the window function rather than inherent properties of the signal itself. Also, the spectrogram is not unique, and is not necessarily zero when the signal itself is zero [70].

The Wigner-Ville Distribution

The Wigner-Ville distribution is a generalised spectrum for time-frequency analysis. It was developed as a spectral analysis technique from the well-known Wigner function in quantum mechanics, and is a member of the more general *Cohen's class* of time-frequency distributions [70]. The Wigner-Ville distribution is defined as:

$$\mathcal{W}_{WV,xx}(t, \omega) = \frac{1}{2\pi} \int_{-\infty}^{\infty} x\left(t + \frac{\tau}{2}\right) x^*\left(t - \frac{\tau}{2}\right) e^{-i\omega\tau} d\tau \tag{2.41}$$

Intuitively, its calculation can be thought of as follows. At a particular time of interest t, we multiply a segment of the signal of length τ to the left of t by a similar portion to the right, giving $x\left(t + \frac{\tau}{2}\right) x^*\left(t - \frac{\tau}{2}\right)$. We then take the Fourier transform with respect to τ, and repeat the process for all desired values of t. The Wigner-Ville distribution is real, unique, and satisfies the conditions for obtaining marginal distributions of time and frequency given in Eq. 2.36 and Eq. 2.37, respectively. For a finite duration signal, it is zero outside the end points and the band limit (if any). However, like the STFT, it is not necessarily zero when the signal is zero [70]. The discrete implementation of

the Wigner-Ville distribution can be written as:

$$\mathcal{W}_{WV,xx}(n,m) = \frac{1}{\pi}\sum_k x^*(n+k)x(n-k)e^{-\frac{2imk}{N}} \tag{2.42}$$

where N is the length of the data vector, and n and m are discrete points in the time and frequency domains respectively. In practice, to implement the algorithm one forms the quantity $x^*(n-k)x(n+k)$ and then performs a fast Fourier transform (FFT). This procedure is then repeated for each value of n, i.e., each discrete time point.

It can be seen from Eq. 2.41 that the Wigner-Ville distribution is a non-linear transform. As a consequence it does not admit superposition, i.e., the spectrum of a multi-component signal is not equal to the sum of the individual spectra of each component. The spectrum of a multi-component signal will contain "cross-terms", which can be considered artifacts. This effect can be suppressed by amending Eq. 2.41 to include a smoothing kernel [16,62]. The choice of this kernel can be tailored to suit the particular application. Choi and Williams [71] proposed the following kernel function,

$$\Phi(\eta,\tau) = e^{-\alpha(\eta\tau)^2} \tag{2.43}$$

with which we can rewrite Eq. 2.41 as follows:

$$\mathcal{W}_{WVC,xx}(t,\omega) = \frac{1}{2\pi}\int_{-\infty}^{\infty}\Phi(\eta,\tau)x\left(t+\frac{\tau}{2}\right)x^*\left(t-\frac{\tau}{2}\right)e^{-i\omega\tau}d\tau \tag{2.44}$$

The introduction of $\Phi(\eta,\tau)$ has a "low-pass" effect on the resulting spectrum, by suppressing the higher-frequency cross-terms. The Wigner-Ville distribution is typically computed using a fast Fourier transform algorithm [72]. The *cone-shaped kernel* is an alternative kernel function, which also attempts to smooth cross-terms while maintaining good time and frequency resolution [73]. In this case, the kernel function is defined as

$$\Phi(\eta,\tau) = g(\tau)\,|\tau|\,\frac{\sin\alpha\eta\tau}{\alpha\eta\tau} \tag{2.45}$$

where $g(\tau)$ is a smoothing function. With this kernel, we can rewrite the time-frequency distribution of Eq. 2.41 in a form known as the *Zhao-Atlas-Marks (ZAM) distribution* [70]. The ZAM distribution for a non-stationary process $x(t)$ is given by

$$\mathcal{W}_{ZAM,xx}(t,\omega) = \frac{1}{4\pi}\int_{-\infty}^{\infty}g(\tau)e^{-i\omega\tau}\int_{t-|\tau|}^{t+|\tau|}x^*\left(u+\frac{\tau}{2}\right)x\left(u-\frac{\tau}{2}\right)du d\tau \tag{2.46}$$

Similarly, the cross-ZAM distribution for two non-stationary processes $x(t)$ and $y(t)$ is given by

$$\mathcal{W}_{ZAM,xy}(t,\omega) = \frac{1}{4\pi} \int_{-\infty}^{\infty} g(\tau) e^{-i\omega\tau} \int_{t-|\tau|}^{t+|\tau|} x^* \left(u + \frac{\tau}{2} \right) y \left(u - \frac{\tau}{2} \right) du d\tau \qquad (2.47)$$

The ZAM distribution has the advantage that it can completely remove the cross-term between two components that have the same center frequency [73].

The major advantages of the Wigner-Ville spectrum include its strong ability to resolve components in multi-component signals, and the fact that it reduces to the ordinary spectral density if the signal under examination is stationary. Aside from the cross-terms described previously, another disadvantage of the Wigner-Ville spectrum is that it can produce negative values, which are not physically meaningful [62].

Time-Frequency Coherence

In the context of signal processing, the *coherence function* is a useful normalised measure of the cross-correlation of the spectral components of two jointly stationary processes. For two such processes $x(t)$ and $y(t)$, the coherence function can be defined as:

$$\Gamma_{xy}(\omega) = \frac{P_{xy}(\omega)}{\sqrt{P_{xx}(\omega)P_{yy}(\omega)}} \qquad (2.48)$$

where P_{xx} and P_{yy} denote the PSD of $x(t)$ and $y(t)$ respectively, and P_{xy} is the cross-spectral density of $x(t)$ and $y(t)$. The coherence function satisfies

$$\left| \Gamma_{xy}(\omega) \right|^2 \leq 1 \qquad (2.49)$$

with $\left| \Gamma_{xy}(\omega) \right|^2 \equiv 0$ if $x(t)$ and $y(t)$ are uncorrelated, and $\left| \Gamma_{xy}(\omega) \right|^2 \equiv 1$ if they are related by an invertible, linear time-invariant system [74].

The coherence function can also be extended to the non-stationary case [74, 75]. For two non-stationary processes $x(t)$ and $y(t)$, the time-frequency coherence function can be written as:

$$\Gamma_{xy}(\omega,t) = \frac{\mathcal{W}_{xy}(\omega,t)}{\sqrt{\mathcal{W}_{xx}(\omega,t)\mathcal{W}_{yy}(\omega,t)}} \qquad (2.50)$$

where $\Gamma_{xy}(\omega,t)$ is a complex function, which must satisfy the condition:

$$0 \leq \left| \Gamma_{xy}(\omega,t) \right|^2 \leq 1 \qquad (2.51)$$

White and Boashash [76] showed that the only choice of time-frequency distributions that yield meaningful estimates of $\Gamma_{xy}(\omega, t)$ are positive time-frequency distributions of Cohen's class. Muma et al. [75] proposed an estimator for the time-frequency coherence function, based on the ZAM distribution. We are grateful to the authors for providing us with the MATLAB code for the implementation of this estimator. It is defined as:

$$\hat{\Gamma}_{ZAM,xy}(\omega, t) = \frac{\mathcal{W}^{(c)}_{ZAM,xy}(\omega, t)}{\sqrt{\mathcal{W}^{(c)}_{ZAM,xx}(\omega, t)\mathcal{W}^{(c)}_{ZAM,yy}(\omega, t)}} \tag{2.52}$$

for all $(t, \omega) \in \mathcal{R}$. Note that $\mathcal{W}^{(c)}_{ZAM,xy}(\omega, t)$ refers to the cross-ZAM distribution, which is smoothed by a Gaussian smoothing kernel $c(t, \omega)$.

2.3 Statistical Properties

Power-Law Distributions

A quantity x obeys a power law if it is drawn from a probability density function $f(x)$, where

$$f(x) \propto x^{-\alpha} \tag{2.53}$$

where α is a constant parameter known as the *power law exponent* or *scaling parameter* [77]. In most real situations $2 < \alpha < 3$, though this is not exclusively the case. It is difficult to show that an observed quantity is drawn from a power-law distribution, instead one can attempt to show that the observed data is consistent with a model of the form given in Eq. 2.53. It is of interest in some situations to determine the power law exponent α of an empirical data set that exhibits power-law behaviour. Taking the log of both sides, Eq. 2.53 can be rewritten as

$$\log_{10} f(x) \propto -\alpha \log_{10} x \tag{2.54}$$

This implies that if one plots a representation of a particular PDF on a doubly logarithmic plot, a straight line with slope $-\alpha$ would be expected if the data follows a power-law distribution. Though α could be estimated by performing a linear regression, it should be noted that this method can lead to significant bias under commonly observed conditions [77]. The Hill estimator is an alternative approach to estimating

α that can give improved results. The Hill Estimator can be computed as follows:

$$\hat{\alpha} = 1 + n \left[\sum_{i=1}^{n} \ln \left(\frac{x_i}{x_{min}} \right) \right]^{-1} \tag{2.55}$$

where x_i, $i = 1, 2, \ldots, n$ are the observed values of x such that $x_i \geq x_{min}$. This gives an asymptotically unbiased and consistent estimate [77]. It is commonly found that a lower bound on the region of power-law behaviour x_{min} exists, such that the distribution does not follow the power-law form for $x < x_{min}$. This can be seen in e.g. the symmetric Lévy-stable distribution where a power-law is the dominant influence in the tail region [78].

A notable feature of processes with power-law distributions is the presence of *self-similarity*. An object is said to have *geometrical self-similarity* if it can be related to parts of itself by similarity transformations. Self-similarity is a key concept to the study of fractal objects. The sum of N random variables with a power-law type probability density function is known to have a self-similar structure [78]. If one looks at a graph as a geometrical object, conceptually the notion of self-similarity could be applied to the graph of a function of time. This is not strictly applicable as the ordinate and abscissa of such a plot are dependent on the units used, and scaling would be an issue. Under these circumstances, the term *self-affine* is more appropriate than self-similar [50]. A *strictly self-affine* process can be defined as a process whose PDF is scale-invariant[2] [79], i.e.,

$$f(x,t) = b^{-H} f(x,t) \tag{2.56}$$

where H is a constant and b is an arbitrary scaling factor. As with the definition of stationarity, it is also possible to define a process that is *wide-sense self-affine*. This refers to a process where only the first and second-order moments are scale-invariant. For Gaussian processes, wide-sense self-affinity is equivalent to strict self-affinity. To find a function of time that could be exactly geometrically reconstructed from a union of transformations of itself under scaling in time and amplitude would not be a realistic situation. Instead, one can aim to measure a degree of statistical self-similarity in a process. In general, a random process $x(t)$ can be said to be *statistically self-similar* if the processes $x(t)$ and $b^{-\alpha} x(t)$ are statistically indistinguishable. A well-known example of a self-similar process is ordinary one-dimensional Brownian motion. An illustration of this, along with a description of some methods to measure statistical

---

[2]The term "scale-invariance" generalises the concept of fractals. In our case, scale-invariance refers to the observation that fluctuations appear to occur on all time-scales, regardless of amplitude. The interested reader is directed to Sornette Pg. 148 for a more detailed treatment [78].

self-similarity in time series is given by Bruce [50].

"1/f" Behaviour and Long-Term Correlation

Self-similarity has been reported in the spatial and temporal structure of many physiological processes [80], such as heart-rate [81, 82], auditory nerve firings, lung inflation, breathing, walking, and blood pressure. Many of these processes exhibit a property whereby their power spectral density $P(\omega)$ is inversely proportional to frequency, a phenomenon commonly known as $1/f$ *noise* (where $f = \frac{\omega}{2\pi}$ refers to the cyclic frequency). As it is generally referred to, $1/f$ noise implies that

$$P(f) \propto \frac{1}{f^\gamma} \tag{2.57}$$

where γ is a constant. In loose terms, γ is not necessarily required to equal unity for the process to be described as $1/f$ noise. However, given that $\gamma = 0$ is the condition for *white noise* and $\gamma = 2$ for *Brownian noise*, it can be safely assumed that for the process to be classed as $1/f$ noise or "$1/f$-like", one should at least expect that $0 \leq \gamma \leq 2$. This type of relationship implies that the current state of the process depends not only on its most recent values, but with its long-term history in a self-affine manner [78]. The random $1/f$ process is in general self-affine [79]. Several different explanations have been proposed for the ubiquity of $1/f$ noise in nature, such as intermittent behaviour and self-organised criticality, but the origin is unknown in many cases [80].

2.4   Signal Modelling

Signal modelling is the use of mathematical models to represent a particular signal, or the system that generates this signal. The parameters of these models can then be used in signal analysis, and in some applications are useful in pattern recognition or diagnostics. Depending on the application, the model parameters may give us insight into physical or physiological aspects of the system. Signal models are also useful for the generation of surrogate data, which can be used as a basis for further statistical study [83]. Signal models often include noise or other artifacts along with the "true" signal in order to make the model more realistic [58]. A simple model of a biomedical signal $x(t)$ could be given as

$$x(t) = s(t) + v(t) \tag{2.58}$$

where $s(t)$ denotes the true signal and $v(t)$ is additive noise (often assumed to be Gaussian white noise). The inclusion of $v(t)$ is intuitive, as in effect it means that if the same measurement of $x(t)$ was performed multiple times under identical conditions, each measurement would be different due to the noise. However, in reality $s(t)$ itself may be a stochastic process and therefore the value of $s(t)$ can also vary with repeated measurements. For this reason, Eq. 2.58 may constitute an unrealistic model.

Modelling a Stochastic Signal Using a Discrete-Time Linear System

The future values of a stochastic process (or signal) cannot be predicted exactly [53]. This may be due to the fact that the mechanisms of the system that generated the signal may be randomly changing, or due simply to the fact that we do not fully understand their behaviour. In any case, we can attempt to model the signal by making an assumption that the unexplained variability in the signal is due to the presence of random disturbances [50]. Assuming the process is stationary, we can construct a parametric model in the form of a general *linear time-invariant* (LTI), discrete time system. This type of system can be represented by the difference equation

$$y(n) = -\sum_{k=1}^{p} a_k y(n-k) + \sum_{k=0}^{q} b_k x(n-k) \tag{2.59}$$

where $x(n)$ is the input, $y(n)$ is the output, and a_k and b_k are the system parameters. The order of the system is determined by p and q. Intuitively, the above equation specifies that the output of an LTI system is a weighted linear combination of its input, as well as of its own past states. The system can also be described by its z-domain transfer function $H(z)$, where

$$H(z) = \frac{\sum_{k=0}^{q} b_k z^{-k}}{1 + \sum_{k=1}^{p} a_k z^{-k}} \tag{2.60}$$

An illustration of the general form of a discrete-time LTI system is given in Figure 2.1. For the signal modelling problem, the input is unknown and instead we aim to model a discrete-time observable process $x(n)$ as the output of a linear system driven by a random disturbance $v(n)$. We assume that $v(n)$ is a white noise process with mean $\mu_v = 0$ and variance σ_v^2 equal to its power spectral density. This leads us to the following model for $x(n)$, known as an *autoregressive moving average (ARMA)* model [53].

$$x(n) = -\sum_{k=1}^{p} a_k x(n-k) + \sum_{k=0}^{q} b_k v(n-k) \tag{2.61}$$
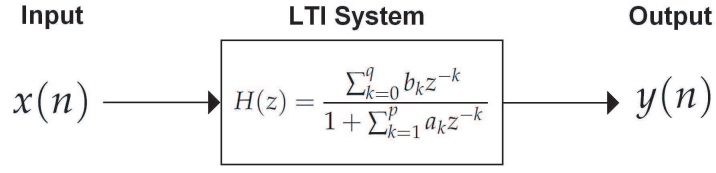
Input   **LTI System**   **Output**

$$x(n) \longrightarrow \boxed{H(z) = \frac{\sum_{k=0}^{q} b_k z^{-k}}{1 + \sum_{k=1}^{p} a_k z^{-k}}} \longrightarrow y(n)$$

Figure 2.1: Illustration of the input-output relationship for a standard linear time-invariant (LTI) discrete-time system.

White Noise Disturbance   **LTI System**   **Modelled Signal**

$$\nu(n) \longrightarrow \boxed{H(z) = \frac{\sum_{k=0}^{q} b_k z^{-k}}{1 + \sum_{k=1}^{p} a_k z^{-k}}} \longrightarrow x(n)$$
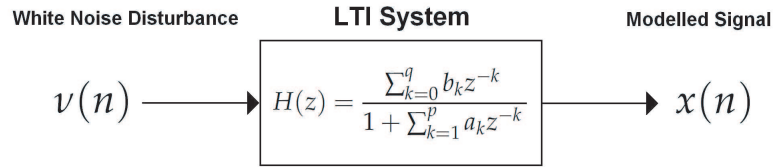
Figure 2.2: Illustration of the input-output relationship for the signal modelling problem. Note that the observed process $x(n)$ is modelled as the output.

Thus, we can redraw the standard discrete-time LTI configuration of Figure 2.1 to illustrate the signal modelling configuration; the result is shown in Figure 2.2.

In some cases, only the current state of the disturbance $\nu(n)$ is included in the model equation, in which case only the a_k terms need to be estimated. This is known as an autoregressive (AR) model. The objective is to obtain the best possible linear system model that will transform $\nu(n)$ into a process that has the characteristics of the measured signal.

The model parameters a_k and b_k can be estimated by solving linear equations constructed from the autocorrelation function of the observed process. For an AR process, we can find values for a_k using the *Yule-Walker* or *autocorrelation method* [50]. We attempt to model a process $x(n)$ as:

$$x(n) = -\sum_{k=1}^{p} a_k x(n-k) + G\nu(n) \tag{2.62}$$

But the input $\nu(n)$ to the process is unknown, therefore we must estimate $x(n)$:

$$\hat{x}(n) = -\sum_{k=1}^{p} a_k x(n-k) \tag{2.63}$$

The error in this prediction can be written as:

$$e(n) = x(n) - \hat{x}(n) = x(n) + \sum_{k=1}^{p} a_k x(n-k) \tag{2.64}$$

Next, we look to optimise the model by choosing the parameters a_k that minimise the total squared error ϵ_p:

$$\epsilon_p = \sum_{n=0}^{\infty} e^2(n) = \sum_{n=0}^{\infty} \left(y(n) + \sum_{k=1}^{p} a_k x(n-k) \right)^2 \tag{2.65}$$

Minimisation is achieved by solving the following:

$$\frac{\partial \epsilon_p}{\partial a_k} = 0, \quad 1 \le k \le p \tag{2.66}$$

This yields the following set of equations for $1 \le i \le p$

$$\sum_{k=1}^{p} a_k \sum_{n=0}^{\infty} x(n-k)x(n-i) = -\sum_{n=0}^{\infty} x(n)x(n-i) \tag{2.67}$$

This gives us a set of non-linear equations to solve. To simplify, we assume that the signal is zero outside the available data range N. Therefore the autocorrelation sequence can be written as follows:

$$R_{xx}(i) = \sum_{n=i}^{N-i-1} x(n)x(n-i) \tag{2.68}$$

Substituting into the previous result, we get the *normal equations*:

$$\sum_{k=1}^{p} a_k R_{xx}(i-k) = -R_{xx}(i), \quad 1 \le i \le p \tag{2.69}$$

The autocorrelation sequence R_{xx} can be estimated from the measured data. Therefore we can solve for a_k, completing the AR model.

One limitation of the ARMA approach is that in general it can only produce stationary output[3]. The problem of non-stationarity could be addressed more directly by extending a model such as the ARMA type described above to encompass the non-

---

[3]ARMA-type models can generate non-stationary output if the parameters fulfill certain conditions. However, this non-stationary behaviour is of a special type. This issue is dealt with in detail by Priestley (1984) [60].

stationary case. This could be achieved for example by allowing the coefficients of the ARMA model to be time-varying [56], or by constructing an *autoregressive moving average (ARIMA) model*. ARIMA models are an extension of the standard ARMA model [53]. Differencing is applied to the data (as described in Eq. 2.20 in order to render it stationary. After differencing, the Yule-Walker (autocorrelation) method can again be used to extract ARMA parameters from the data, leading to the completed model:

$$z(n) = \Delta^d x(n) = -\sum_{k=1}^{p} a_k x(n-k) + \sum_{k=0}^{q} b_k v(n-k) \qquad (2.70)$$

where d is the level of differencing.

2.5   Non-Stationary Signal Models

Following on from the stationary models introduced in the previous section, we now discuss non-stationary signal models. In Section 2.1.3 we discussed the notion of non-stationarity and how it is manifested in signals and systems. One of the simplest such models was given in Eq. 2.19, which could be deemed a "trend plus stationary residual" model [60]. The deterministic function $\psi(t)$ further determines the type of model. For example, $\psi(t)$ could impose a steady growth or decay in the long-term behaviour of the signal, or impose some "seasonal" constraint.

In the previous section, we intimated that ARMA or ARIMA-type models could be used to model non-stationary signals and produce non-stationary output. The non-stationary behaviour produced by these models is of a specific type, known as "explosive" behaviour [60]. Though the second-order statistics of these processes do vary, their complete future evolution is governed by the parameters fitted to the initial data. ARMA models with freely varying time-dependent parameters (rather than fixed parameters) would therefore be required to more accurately model processes whose second-order statistics vary arbitrarily in time. Grenier (1985) described how the ARMA approach could be adapted for non-stationary signals [56]. As in Eq. 2.62, the process $x(t)$ is considered to have been generated by a linear system, however the impulse response terms of this system are assumed to be time-varying. A finite-order discrete ARMA representation of this arrangement can be expressed as

$$x(n) = -\sum_{k=1}^{p} a_k(n-k)y(n-k) + \sum_{k=0}^{q} b_k(n-k)v(n-k) \qquad (2.71)$$

if and only if the impulse response satisfies certain conditions [56]. The model parameters $a_k(n)$ and $b_k(n)$ can be approximated by a weighted combination of known deterministic functions, whose coefficients can in turn be estimated using more familiar approaches such as the Yule-Walker method.

An alternative methodology is to use a linear model structure such as the AR process of Eq. 2.62, but allow the random input $v(n)$ to be non-stationary. This approach has been implemented in the modelling of non-stationary EEG [83], where a piecewise linear frequency modulated sawtooth input is applied to an ARMA model, which is then passed through a non-linear shaping function. Though the linear and non-linear parts of the model are both static, the frequency modulation of the input signal enables it to be used for processes that exhibit both non-linearity and non-stationarity.

Two common features exhibited by non-stationary processes are amplitude modulation (AM) and frequency modulation (FM). These features can be identified via time-frequency representations, and can be exploited to develop parametric models of signals. This approach was adopted in the modelling of ocular aberration dynamics by Iskander et al. [84]. Motivated by findings of AM and FM characteristics in the dynamics of Zernike coma and spherical aberration, the authors sought to model Zernike aberration components as AM-FM signals. Each aberration signal c_i was deemed to be a sum of distinct frequency components:

$$c_i(n) = \sum_{l=1}^{L} u_{i,l}(n) \tag{2.72}$$

where $u_{i,l}$ are the frequency components and n is the discrete sample time. Each $u_{i,l}$ was fitted with a parametric model of the form:

$$u_{i,l}(n) = \left(\sum_{p=0}^{P} g_p \left(\frac{n}{N} \right)^m \right) \cos \left(\sum_{q=0}^{Q} r_q n^q \right) \tag{2.73}$$

where N is the signal length, P and Q are model orders, g_p are the amplitude modulation parameters, and r_q are the frequency modulation parameters. Using an analytic signal representation, the authors obtained estimates of g_p and r_q by performing linear regressions. The authors reported the dynamics of short data samples (5 s) could be well fitted with the AM-FM model, with a low model order of $P < 20$ and $Q < 5$.

Chapter 3

Dynamics of Ocular Aberrations

In Chapter 1, we introduced the concept of ocular wavefront aberrations, and briefly discussed their dynamic features. We will now address the measurement and quantification of these dynamic changes in aberrations, and present some analysis of their spectral content and statistical properties. This section of the project was part of a collaboration with Charles Leroux, who was responsible for designing and building the hardware and software for an aberrometer in the Applied Optics Group, as well as developing the wavefront reconstruction algorithm.

3.1 Ocular Wavefront Sensing

One can define the wavefront of a light beam as the locus of points in space that are of equal optical phase. For a collimated beam, this is a plane perpendicular to the axis of propagation of the beam. In an aberrated optical system (such as the eye), the wavefront will have departures from this plane. While *wavefront sensing* is the term used to describe the measurement of wavefront aberrations in general, the measurement of wavefront aberrations in the eye is typically referred to as *aberrometry* [7].

Ocular aberrometry was first directly performed by Smirnov in 1961, using a sub-

jective technique [85]. Subsequent methods included approaches based on laser ray tracing, the Foucault knife edge test, and double-pass intensity images. The Shack-Hartmann sensor was first used for ocular wavefront sensing in 1994 [86]. Shack-Hartmann sensors have since become established as the method of choice for many researchers, due in part to their reliability and ease of use [3]. For these reasons, Shack-Hartmann sensing is the method we used in this thesis.

Shack-Hartmann Wavefront Sensing

The basic operating principle of the Shack-Hartmann sensor involves a point source at infinity that is imaged onto the retina, and is then considered as a secondary light source (effectively consisting of backscattered light). The wavefront of this source is then sampled with a lenslet array placed in a conjugate plane of the pupil. Each lenslet focuses part of the wavefront onto a CCD camera, forming an array of image spots. These spots are used to determine the aberrations of the wavefront.

An in-depth physical description of Shack-Hartmann wavefront sensing in the eye is given by Bara [87]. This treatment defines the wavefront $W(\mathbf{r})$ via the complex amplitude distribution $u(\mathbf{r}) = A(\mathbf{r})e^{ikW(\mathbf{r})}$ of a monochromatic wave at a given plane. It is assumed that each lenslet can be treated independently. One can define the Fresnel approximation of the propagation of the optical field along the optical axis (z-axis) from the pupil plane $z = 0$ of the lenslet to the detector plane $z = z_0$. This yields the equation of propagation of the centroid $\rho_c(z)$ of the light irradiance distribution $I(\mathbf{r})$ along the z-axis:

$$\rho_c(z) = \rho_c(0)\left(1 - \frac{z}{f}\right) + \frac{z}{E_S}\int_S I(\mathbf{r})\nabla W_a(\mathbf{r})d^2\mathbf{r} \tag{3.1}$$

where $\mathbf{r}$ is the radial distance from the center of the corresponding spherical wave, S refers to the subaperture area on the sensor, $E_S = \int_S I(\mathbf{r})d^2\mathbf{r}$, f is the focal length of each lenslet, and $W_a(\mathbf{r})$ is the wavefront incident on each lenslet. The centroid position $\rho_c(z)$ of the irradiance distribution $I(\mathbf{r})$ in the infinite detector plane is proportional to the spatial integration of the gradient of the wavefront $W(\mathbf{r})$ over the lenslet, provided that $I(\mathbf{r})$ in the pupil plane is homogeneous over the lenslet. The estimated gradient of the wavefront is scaled by the effective distance z_0, which in practice requires calibration.

The displacements of each spot with respect to a reference is proportional to the local slope of the wavefront. This relationship is illustrated in Figure 3.1. After the irradi-
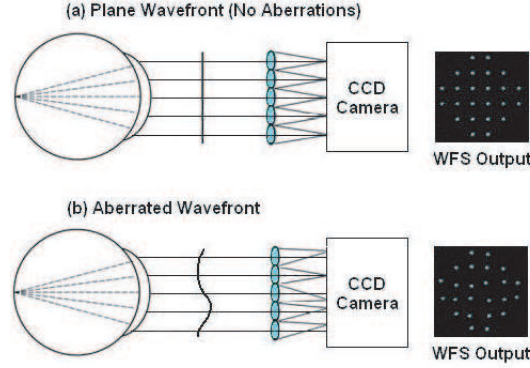
Figure 3.1: Principle of Shack-Hartmann Wavefront Sensor.

ance data measured at the detector is processed, the position of the centroid of each lenslet can be determined. Given that there are N lenslets, the wavefront sensor slope measurements at the ith lenslet can be modelled as [87]:

$$m_i = \frac{\rho_c(f)}{f} + v_i = \frac{1}{E_S} \int_S I(\mathbf{r}) \nabla W_a(\mathbf{r}) d^2\mathbf{r} + v_i \tag{3.2}$$

where v_i is a noise term that accounts for readout, quantisation, and other noise sources. As shown in Eq. 1.6, the incoming wavefront W_a can be expanded as a linear combination of Zernike polynomials (though other orthonormal bases could also be used). For ease of implementation, one can use a single-index arrangement of Zernike polynomials, such as the system proposed by Thibos et al. [23]. We can thus write

$$W_a(\mathbf{r}) = \sum_{j=1}^{N} c_j Z_j(\mathbf{r}) \tag{3.3}$$

This arrangement is convenient in that it facilitates us to rewrite Eq. 3.2 in a matrix form:

$$\mathbf{m} = \mathbf{Ac} + \mathbf{v} \tag{3.4}$$

where $\mathbf{m}$ is a vector of length $2M$, with the first M elements corresponding to the x-components of each m_i and the remaining M elements corresponding to the y-components. The column vector $\mathbf{c}$ contains the coefficients c_i, $i = 1, \ldots, N$ of the Zernike expansion. A is a $2M \times N$ matrix, defined by

$$A_{ki} = \frac{1}{E_S} \int_S I(\mathbf{r}) \nabla_k Z_i(\mathbf{r}) d^2\mathbf{r} \tag{3.5}$$

We cannot solve Eq. 3.4 exactly [88,89], so we adopt an alternative approach whereby we attempt to find a solution to:

$$\hat{c} = \mathbf{Rm} \tag{3.6}$$

where R is known as the *reconstruction matrix* and is calculated in order to minimise the norm $\|\hat{c} - \mathbf{Rm}\|$ [88]. Provided that $2M > N$, Eq. 3.6 can be solved using an approximate least-squares fit:

$$\mathbf{R} = (\mathbf{A^T A})^{-1}\mathbf{A^T} \tag{3.7}$$

Assuming that the slope measurements m_i and incoming wavefront W_a are correctly modelled, Eq. 3.7 provides an unbiased estimate of the Zernike coefficients [87]. The sensitivity and dynamic range of a Shack-Hartmann sensor depend on the particular design and lenslet geometry. Estimation of the wavefront from the measured local slopes is subject to fitting error, and the centroiding algorithm used to pinpoint the position of the spots on the CCD is subject to several sources of error, including photon noise and readout noise [3].

It is important to remember that the light source used in the Shack-Hartmann sensor actually passes through the eye twice, and as such can be considered a double-pass problem. In a sensor with equal entrance and exit pupils, this potentially leads to underestimation of the odd aberrations of the eye [90]. This problem can be effectively reduced, however, by the use of a small (≤ 1 mm) pinhole to restrict the incoming beam, which allows the beam to be considered unaberrated when it is focused on the retina [21].

3.2 Experimental Setup and Procedure

Data was collected using a custom-built aberrometer based on a Shack-Hartmann wavefront sensor. The experimental setup is shown in Figure 3.2. This section describes work carried out in collaboration with Charles Leroux of the Applied Optics Group, who designed and implemented the aberrometer, developed the experimental procedure for measuring the dynamics of aberrations, and also contributed to the data processing.

3.2.1 The Aberrometer

Sensor Specifications

The aberrometer used a state-of-the-art CMOS detector, the NIR Microvista^{TM} manufactured by Intevac® for near infrared applications. The number of pixels of the detector used to map the measured pupil fixed the frame rate that could be achieved. We used three different configurations of the detector: 440×440, 396×396, and 286×286 pixels for frame rates of 80 Hz, 100 Hz, and 173 Hz respectively. The array of lenslets was a square grid with a 200 mm pitch. Each lenslet corresponded to 18.5×18.5 pixels of the detector, which was enough to maintain linearity on the estimated centroid positions of the Shack-Hartmann spots. The pupil of the eye was imaged onto the Shack-Hartmann lenslets with a magnification of 0.8, so the pupil of the eye was effectively sampled with a spatial resolution of 250 μ m. The sampling properties of the aberrometer are summarized in Table 3.2.1.

Table 3.1: Sampling properties of the aberrometer for 3 different configurations.

Measured Pupil Diameter (mm)	No. of Lenslets Across Diameter	Frame Rate (Hz)
3.9	15	173
5.4	21	100
6.0	23	80

Optical Layout

The optical layout of the system is shown in Figure 3.2. We used a scanning mirror (conjugated to the pupil plane) to reduce the speckle effect linked to the scattering properties of the retinal layers and to obtain time-resolved and low noise measurements. A 4-f system relayed the exit pupil of the eye to the scanning mirror. We chose the smallest scanning mirror possible, in order to maximise the scanning frequency allowed by the galvanometer on which it was mounted. A second 4-f system conjugated the scanning mirror with the Shack-Hartmann sensor. All the lenses used in the system were achromatic doublets, optimised for near infrared applications.

A field stop, placed in a plane conjugated with the retina, allowed us to cut the small portion of the probing beam that was directly reflected by the lenses. These reflections, and the reflection from the cornea, were also controlled by translation of the probing beam parallel to the optical axis of the instrument. This was done by tilting
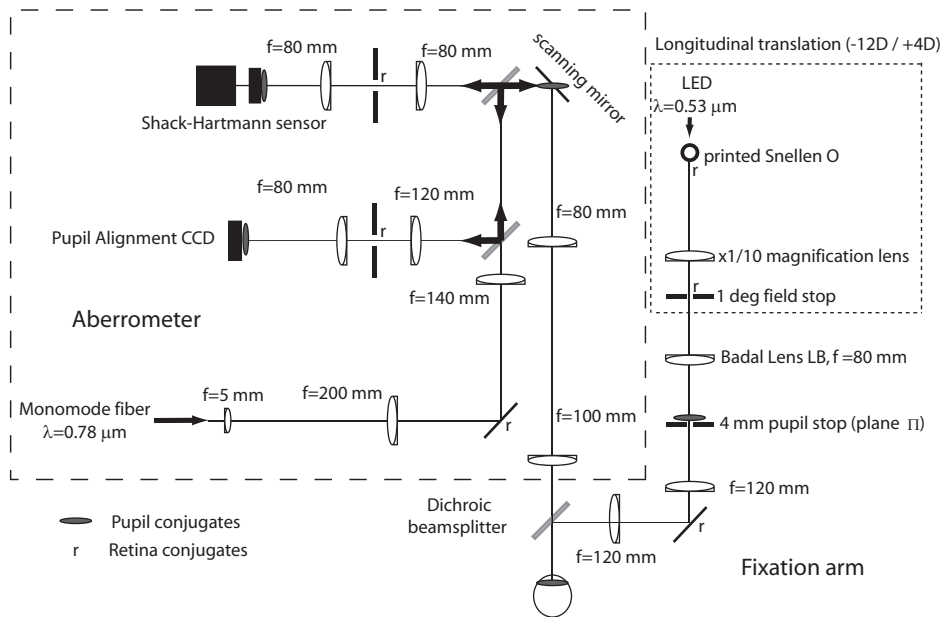
Figure 3.2: Aberrometer setup. A fixation arm is included, which allows a target to be translated longitudinally. Figure reproduced courtesy of Charles Leroux.

the mirror, which was placed in a plane conjugated with the retina. When adjusting the position of the probing beam, it was important to make sure that it was far away from the position that maximises the Stiles-Crawford effect, which is typically less than 2 mm away from the center of the pupil [91]. This reduced the amount of light scattered from the fundus of the eye, but allowed us to collect data that had a signal-to-noise ratio that was homogeneous over the entire pupil.

The aberrometer was calibrated using a point source located at a distance of 938 ± 1 mm away from the measurement plane. This meant that the power of the measured wavefronts was reliably measured after removing the divergence of the reference, to an accuracy of 0.001 D. Because of the chromatic effect of the optics of the eye, the measured accommodative response values were biased by approximately -0.5 D compared to the 0.53 μm central wavelength of our stimulus [19,92]. This bias was not removed from our measurements, so the values given throughout this thesis can be assumed to correspond to the absolute output of the aberrometer in the near infrared.

Fixation Arm

The aberrometer setup included a fixation target on a separate arm capable of longitudinal translation, as shown in Figure 3.2. Figure 3.3 shows the composition of the
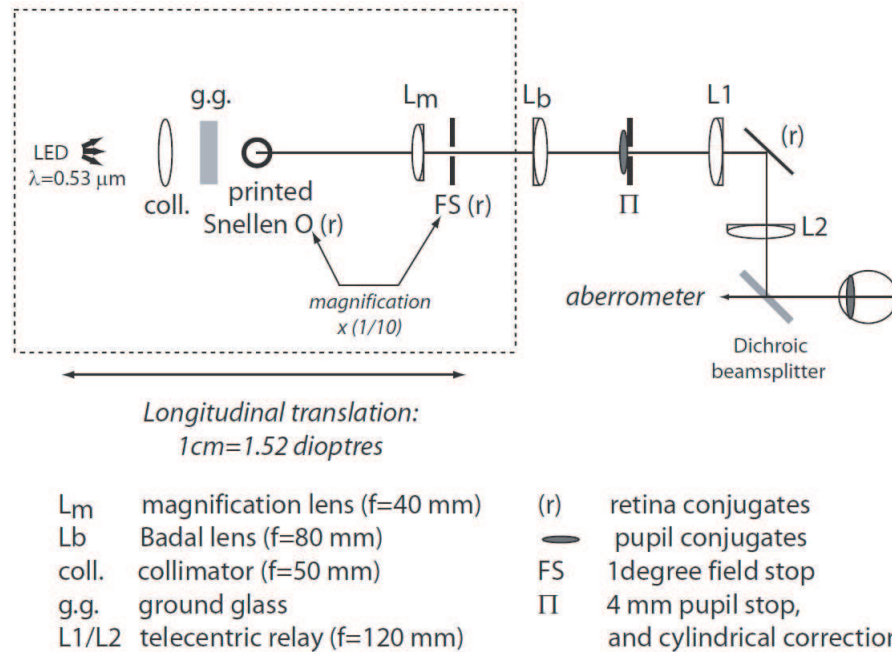
Figure 3.3: Optical setup of the fixation arm. Figure reproduced courtesy of Charles Leroux.

fixation arm in more detail. The fixation arm was connected with the aberrometer via a dichroic beamsplitter. The source was a LED with central wavelength 0.53 μm (green), which illuminated the fixation target. The target itself was a 6/12 Snellen "O" letter with an angular size of 10 arcmin and stroke of 2 arcmin. It was printed with a 600 dpi printer, giving a letter size of 2.5 mm (stroke 0.5 mm). The field of view of the entire target (including the green background) was a circle of 1°. The probing beam was centered slightly off axis, so that it was seen by the subject just outside of the green circular field.

The target vergence could be varied linearly with the translation stage, and so the ocular wavefront aberrations could be measured when the subject was fixating at a range of viewing distances. The dioptric demand induced by a 1 cm displacement of the target towards the Badal lens L_b was +1.52 D. The maximum possible accommodation demand that could be set in this way was approximately +12.5 D. The front plane of the Badal lens L_b was conjugated to the pupil of the eye, thus the fixation target had the same extent on the retina, regardless of the target vergence. Some subjects required an astigmatism correction for comfortable viewing of the target. This was provided by the insertion of a trial lens at plane Π. The effective pupil of the eye was conjugated with plane Π on the fixation arm, where it was limited to 4 mm by a

field stop.

Experimental Procedure

In all cases, the subject's dominant eye was measured, while the non-dominant eye was covered with an eye-patch. Eye dominance was assessed through an eye examination by a qualified optometrist prior to the experiments. The subject was aligned using a bite-bar for stabilisation. The probing beam of the aberrometer was a laser source set at a power approximately equal to 15 μW ($\lambda = 0.78$ μm), and was scanned over a 1° field angle to remove speckle on the raw frames recorded by the sensor. For measurements of aberrations, we generally acquired 4,000 data points per trial. The temporal sampling frequency was set to 100 Hz, meaning each trial was approximately 40 s in duration. An active pupil diameter of 5.4 mm was used for all measurements; only subjects with a rest pupil diameter of greater than or equal to this value were measured. The spatial sampling across the pupil was 250 μm. This corresponded to 21 active lenslets across the diameter of the pupil.

3.2.2 Experimental Conditions and Variability in Measurement

There are a number of sources of variability in ocular wavefront sensor measurements. These take the form of both experimental conditions over which we have some degree of control (such as head movement, wavelength of the probing beam, luminance level, subject fatigue), and other sources of variability that influence measurements but cannot be controlled (cardiopulmonary influence, certain eye movements, tear-film dynamics etc.). It is important to understand the many sources of variability in the measurements and where possible, to limit their influence. In Chapter 1, we introduced some of the factors that affect ocular aberrations. We will now discuss a selected few of these factors in the context of how we can change or limit the way they affect our measurements.

Eye Movements

Though some method of restricting head movement (such as a bite-bar) is sometimes used in ocular wavefront sensing in order to help maintain alignment of the eye with the optical system, there is still scope for significant misalignment due to eye movements. Though some attempts to reduce misalignments due to eye movements can be made (e.g., by using a stationary fixation target [16]), they are still always present

to some degree. As a whole, although fixational eye movements are large enough for us to perceive, we are generally unaware of them. If fixational movements are eliminated (such as by use of a restraint on the eye itself [93]), our visual perception fades away as a result of neural adaptation. These movements are therefore essential to our vision. Eye movements are a source of error in the aberrometer measurements, and they can be classified as having three distinct types: tremor, drift, and microsaccades [93].

- **Ocular tremor** (also known as *microtremor* or *physiological nystagmus*) is a wave-like (but aperiodic) motion of the eyes. It has a low amplitude of 25 nm to 2.5 μm. Its frequency content has been reported to range from 90 Hz to 150 Hz [94]. The contribution of tremor to the maintenance of vision is unclear, but it is generally thought to be independent in the two eyes.

- **Ocular drifts** are slow motions of the eye that occur during fixation. They generally last for 0.2-1 s. During this time, the image under fixation is moved through 1 arcmin as a result [93]. Drifts can be used to maintain accurate fixation in the absence of microsaccades in the visual system.

- **Microsaccades** are abrupt, jerking movements of the eye that occur during voluntary fixation. They are approximately 25 ms in duration, and their amplitude can carry the retinal image across 5 arcmin (or several hundred photoreceptors). Microsaccades generally play an important role in foveal vision, in helping to correct fixation errors. For example, if drift moves the image away from the fovea, microsaccades tend to bring it back. Unlike tremor, microsaccades in the two eyes have been found to be conjugate [93].

Fluctuations in Accommodation

Though the steady-state fluctuations of accommodation cannot be actively controlled, we can still adjust their impact on our measurements by taking advantage of the fact that the amplitude of steady-state fluctuations in accommodation is affected by the mean accommodative response [27, 38, 39, 42], and so it follows that one could reduce their impact on the measurement of aberrations by keeping the mean accommodative response at a minimum, i.e., by measuring aberrations at the subject's far point. The amplitude of the fluctuations can be reduced further by the use of cycloplegic drops, such as Cyclopentolate or Tropicamide. These drugs also lead to pupil dilation, which can allow improved spatial sampling of the backscattered light from the

retina. However, one may argue that for vision studies the use of these drugs imposes unrealistic conditions on the eye. For example, ocular aberrations are known to vary spatially over the pupil, and are often more pronounced in the periphery [3]; a dilated pupil size may therefore lead to an unrealistic representation of a subject's aberrations in a functional sense. The nature of accommodation and its effect on vision will be addressed in more detail in Chapter 4.

Tear Film

The influence of the tear film on aberrometer measurements has been acknowledged by several authors [7, 29, 30, 95]. Though it consists of three different layers (a lipid layer, aqueous layer, and mucous layer) of varying function, refractive index, and thickness, it is convenient from an optical point of view to consider the tear film as having a standard refractive index of $n_{tf} \approx 1.337$. There has been some debate regarding the thickness of the tear film, with reported estimates ranging from 4 μm [96] to 40 μm [97]. An interesting issue is whether or not the tear film is thick enough to produce a level of variability in wavefront sensor measurements that would be significant compared to other sources of variability. Gruppetta [29], found that the contribution of the tear film to curvature sensor measurements of accommodation was non-negligible. This was backed up by Dubra [7], who showed that for a conservative estimate of tear film thickness (3 μm), a small sag in the tear film surface could lead to a significant change in the Zernike defocus coefficient. The author went on to show that this difference is significant enough to take a theoretically ideal eye out of the diffraction limit, and to have a noticeable impact on vision. Zhu [95], performed measurements of the ocular surface topography using a high-speed videokeratoscope with a sampling frequency of 50 Hz. Results showed that the Zernike prism, coma, and astigmatism coefficients exhibited the most change following a blink. The author noted that the time taken for these coefficients to regain a semblance of stability varied from 0.4 s to 3 s, suggesting that there is an inherent instability in the tear-film build-up after a blink. It was also noted that the tear film dynamics are generally associated with low-frequency components in the overall dynamics of aberrations, while variations originating from the crystalline lens give rise to both high and low frequency components.

It can be concluded that the tear film plays a role in affecting dynamic ocular aberrations. In this thesis, we did not consider the tear film dynamics independently. Though tear film dynamics vary from subject to subject [30], we did not take measures to account for this effect, apart from only including young, healthy subjects in

our studies, with no known problems relating to tear film (such as dry-eye).

3.2.3 Data Processing

Analysis of dynamic ocular wavefront sensor measurements often takes the form of analysis of the Zernike coefficients as time series [4, 14–17, 29, 30, 33, 98, 99]. The dynamics of individual Zernike terms are often studied, as well as the time evolution of the RMS wavefront error (see Section 1.2). Using the modal wavefront reconstruction of Zernike polynomials introduced in Chapter 1, we can obtain temporal representations of each Zernike coefficient. This temporal reconstruction can be represented by rewriting Eq. 1.6 as follows:

$$W(\rho, \theta; t) = \sum_{n=1}^{N} \sum_{m=0}^{n} c_n^m(t) Z_n^m(\rho, \theta) + \epsilon(\rho, \theta; t) \tag{3.8}$$

For our studies of aberration signals, we used an expansion of Zernike terms up to and including the 8th radial order.

Dynamic ocular wavefront sensor measurements are often complicated by the presence of spurious values. For example, if the alignment of the eye is sufficiently disturbed due to large head or eye movements, the sensor signal may be significantly disrupted or lost altogether. The most common occurrences of spurious or missing values, at least from the point of view of this thesis, are the result of the subject's blinking. The average rate of blinking for typical subjects with healthy eyes has been stated as 12 blinks per minute [100]. For acquisition times of more than a few seconds, it is therefore inevitable that the subject will blink during measurement. The subject should not refrain from blinking, as doing so would disrupt the consistency of the tear-film distribution and give distorted measurements. Subjects should therefore be encouraged to blink naturally in a way that keeps the eye comfortable.

Removal of Blinks

For the pursuit of analysing the dynamics of ocular aberrations, we consider blinks and other spurious sensor output values as interference. Therefore, it is desirable that we remove them from the measured signal. Blinks often manifest themselves as sudden, large discontinuities in the sensor signal[1]. Perhaps the most obvious approach to

---

[1]Blink discontinuities are normally most apparent in the lower order Zernike terms or the RMS wavefront error signal [16].

remove the data samples corresponding to blinks would therefore be to apply some threshold (e.g., a number of standard deviations from the mean) to the signal and remove the extraneous data points [101]. This method would be very suitable for a stationary, Gaussian process, but in practice it suffers from the non-stationary nature of ocular aberration signals (which we will discuss later). Because the mean of these signals tends to vary, and particularly so after a blink, it is difficult to apply a constant threshold in an effective way.

Iskander et al. [16] suggested a more complex method of searching for impulsive behaviour in measured aberration signals, similar to the removal of data that do not fall into a 95 % confidence interval. The authors showed improved results when compared to the threshold method. However, blinks vary significantly in their duration, and they often have an impact on the steady-state level of the aberration signal, as well as the transient effect during the blink itself. This could be explained by differences in the redistribution of tear-film with each blink, as well as eye movement. With any algorithm based on thresholding or confidence intervals, there is always some chance of failing to detect the presence of a blink, or detecting "false positives". Therefore, the only certain way of removing blinks and other artifacts from ocular wavefront sensor measurements is to do so manually. This can be achieved by inspecting aberration signals for discontinuous or impulsive behaviour, and then checking the corresponding Shack-Hartmann image frames to determine whether or not there was valid input to the sensor. In this manner, one can remove as many artifacts as possible from the measurements. In this project, this manual method of artifact removal was used for all data.

Interpolation of Missing Values

The tear-film build up and eye movements associated with blinking had a noticeable impact on the measured signal up to 1 s after the beginning of a blink (e.g., due to tear-film re-organisation, vignetting of the pupil by the eyelid, eye movements, and secondary blinks). These transient phenomena are not related to the true aberration signal, and thus they were generally treated as interference and removed from the data. When all blinks and other artifacts (with their associated transient behaviour) are removed from aberration signals, there is a significant loss of data from the total number of samples obtained with the sensor. In a later study (See Section 4.3) involving 9 young, healthy subjects, where 8,000 data samples were obtained over a time of 46.24 s, we found that approximately 12.5% of the samples were lost on average after the removal of artifacts.

For analysis purposes, it is often considered undesirable to have missing data points in a time series or a signal. This is because discontinuities or intermittencies cause problems for some analysis techniques (for example Fourier analysis). This problem can be alleviated by using interpolation to replace the missing samples [102–104]. A typical method of achieving interpolation is to assume the missing values are zero (or some other constant level), and calculate the Fourier transform. The frequency domain signal is then band-limited according to an arbitrary limit. The inverse Fourier transform is then computed, giving the interpolated signal. This method is not ideal, as the interpolated values do not provide any new information about the dynamics of aberrations, and in fact introduce false information. When the number of missing points to be interpolated is very large, interpolation can become unreliable and inconsistent. It is also possible to remove discontinuities through the use of digital filtering [16], though this again becomes problematic when a large amount of data is missing. For this reason, the use of interpolation for aberration and other signals was avoided whenever possible throughout the project.

3.3 Results

Figure 3.4 shows the time-evolution of several Zernike coefficients for subject CML (a myope). The sensor measurements were recorded from the subject's dominant eye (in this case, the right eye) under partial cycloplegia[2], with the subject viewing a target at his far point. Data was collected over 40 s, with an active pupil diameter of 5.4 mm. The sampling frequency was 100 Hz, giving a total of 4,000 samples per trial. As expected, the defocus term had the greatest magnitude, but there were some contributions from astigmatism, coma, spherical aberration, and other higher-order terms. Note that though the spherical aberration term as illustrated in Figure 3.4 is positive, we observed a negative shift as the fixation target was moved towards the near point. Significant shifts in accommodation were also observed. This is in good agreement with previous studies [28].

---

[2]We use the term "partial cycloplegia", as the cycloplegic effect was introduced using 1% Tropicamide. However, the cycloplegic effect is not total and only lasts for approximately 30 minutes after insertion. Cyclopentolate is a more effective drug for inducing cycloplegia, but this was not used as it has a significantly prolonged effect on the subject [105].
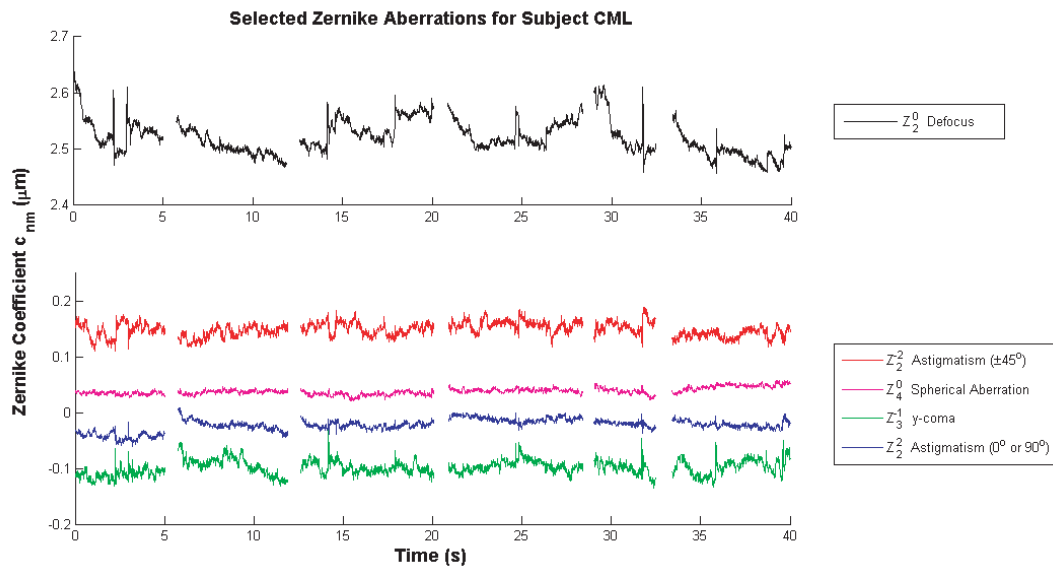
Figure 3.4: Dynamics of selected Zernike aberrations for subject CML. The data was acquired over an active pupil of 5.4 mm, with a frame rate of 100 Hz. 4,000 data samples were taken in total. Spurious data points related to blinks were manually removed.

3.4 Analysis

3.4.1 Spectral Analysis

Figure 3.5 shows PSD estimates (via the Lomb-Scargle periodogram) for the dynamics of Zernike aberrations. The subject was CML, measured under the same conditions as in Figure 3.4. The traces shown are the average of 5 separate measurements. Measurable power is found right up to the Nyquist frequency of 50 Hz, at which point the noise of the system is still 75 times below the measured signal level [91].

Previous authors have established that the temporal dynamics of ocular aberrations are non-stationary [15, 16]. It is therefore appropriate to accompany any frequency-domain analysis with time-frequency analysis to give us information about how the frequency content is varying over time. Figure 3.6 shows a spectrogram of Zernike astigmatism ($\pm 45^o$) for subject CML (the same trial that was shown in Figure 3.4). The spectrogram was evaluated at 1,000 uniformly spaced frequencies from 0.005 Hz to 5 Hz using the Goertzel algorithm [106]. A Hamming window of length 1,600 samples was chosen, with 95% overlap. We already know from the PSD estimate that the spectral power is dominated by low frequencies ($< 2\ Hz$), but the spectrogram
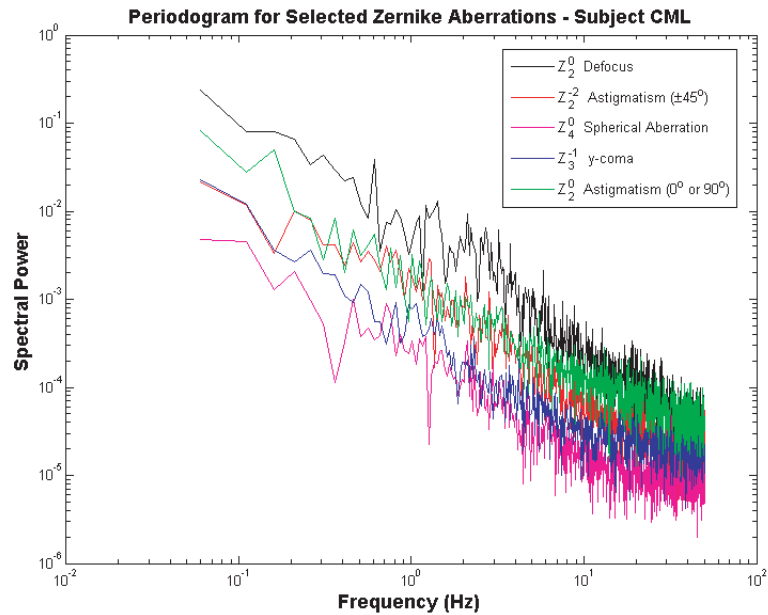
Figure 3.5: Periodograms of selected Zernike aberrations for subject CML.

shows us that this low frequency content is modulated in the $< 0.5 Hz$ range over the 40 s trial. A peak at approximately 1 Hz is also evident, which also varies in frequency. This peak is likely to be related to cardiopulmonary activity [27, 31], but we did not independently verify this with measurements of heart-rate or breathing-rate. We will discuss this issue in further detail with regards to accommodation, in Chapter 4. The ZAM distribution of Figure 3.7 gives a similar picture of the time-frequency content, but with higher resolution. The ZAM distribution was computed in MATLAB using the Time-Frequency Toolbox of Auger et al. [107]. The ZAM distribution plot gives the advantage of allowing us to see the time-frequency content over the full 40 s trial; this is not possible with the spectrogram due to the sliding window function. Note that the colour scaling in both time-frequency representations is relative, and so we are looking for concentrations of energy in the signal rather than absolute measures. For all the time-frequency plots, interpolation in the original signal had to be used, as both the spectrogram and Wigner-Ville based methods like the ZAM distribution are implemented using the fast Fourier transform and therefore do not readily admit non-uniformly sampled data.
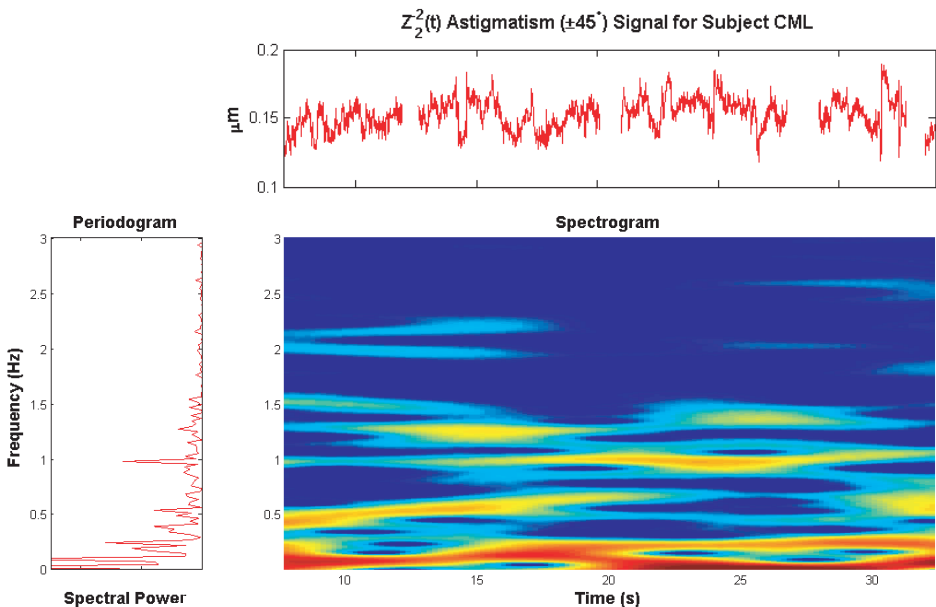
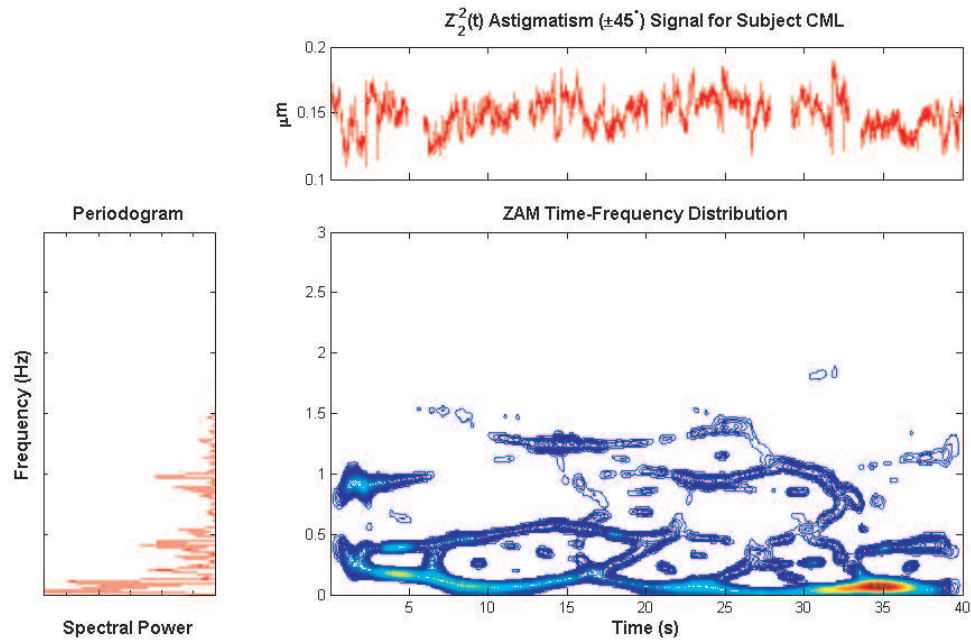Figure 3.6: Spectrogram of Zernike astigmatism for subject CML.

Figure 3.7: ZAM distribution of Zernike astigmatism for subject CML. Improved resolution is achieved using this Wigner-Ville based approach, when compared to the STFT based approach of the spectrogram.

3.4.2 Statistical Characteristics

The PDF and CDF are among the first statistical properties that one tends to examine when dealing with stochastic processes. However, because we are dealing with non-stationary processes, the PDF is not invariant to time as in Eq. 2.9. Therefore, we look to other properties to characterise the statistical nature of our measured data. From Figure 3.4, we can see that the estimated PSD of the aberrations roughly follows a straight line in the region below 10 Hz, when viewed on a doubly logarithmic plot. Using the Hill Estimator (which we will discuss in detail in Chapter 5), we estimated that the slope of the PSD estimates on the log-log scale typically fell in the region of -1.2 to -1.5. This agrees with fitting carried out by previous authors [15, 98]. Overall, we can therefore postulate that dynamic aberration measurements exhibit $1/f$ behaviour (at least over a limited frequency range), in a style similar to other physiological processes [80].

3.5 Conclusions

In Section 1.2, we discussed the influence of the heartbeat on ocular aberrations. Though we have not addressed this relationship here, it has been well established and studied through means such as correlation and coherence analysis [18]. It is believed that the heartbeat dynamics have a significant effect on modulating the aberrations of the eye, possibly resulting from changes in the eye's axial length due to the retinal pulsation. It is interesting to note that heartbeat dynamics have also been shown to exhibit $1/f$ behaviour [82, 108].

The non-stationary nature of the dynamics of ocular aberrations has been established by previous authors [15, 16]. Kasdin [79] stipulated that for $1/f$-like processes, a power-law exponent of greater than unity at low frequencies suggests that the underlying process is non-stationary. For all of our aberration measurements with the subject fixating at the far point, the estimated slope of the PSD on a log-log scale is greater than unity, which agrees well with the statement that dynamic aberrations are non-stationary by nature. However, when the subject was actively accommodating on a target (without cycloplegia), we found that many of the aberrations became more "stable" in terms of their statistical behaviour. This issue of the accommodative effort of the subject having an effect on the statistics of measured aberration signals will be discussed in more detail in the following chapter.

Chapter 4

Dynamics and Statistics of Ocular Accommodation

Accommodation is the process by which the eye changes its refractive power in order to bring objects of regard at different distances into focus. As mentioned in Chapter 1, accommodation is a dynamic process. It can operate as a reflex or be controlled consciously. The dynamics of accommodation in the eye have been the subject of many studies [27,31,37–40,42,43,101]. This is perhaps partly due to the fact that the accommodative mechanism borders on several different fields of study. The behaviour of the lens and the components of the eye that interact with it (particularly the zonule and ciliary muscles) are of physiological interest. The advent of modern cataract surgery has encouraged much new research into these components, to the extent that some new designs of artificial intraocular lenses are claimed to be capable of functional accommodation [109]. Because accommodation is essentially a closed-loop system with sensory input, it has also attracted study from a signals and systems point of view [110]. In particular, the microfluctuations (i.e., small fluctuations about a steady-state level) of accommodation have attracted much interest [27,37–44,47,101,111,112]. In this chapter, we aim to characterise the temporal behaviour of ocular accommodation signals, and in particular the manner in which their statistics vary according to different levels of accommodative effort. The full body of work described in this chapter, apart from Section 4.5, was conducted in collaboration with Charles Leroux of the

Applied Optics Group and Dr. Luis Diaz-Santana of City University, London.

4.1   Measurement of Accommodation

Many studies of the dynamics of ocular accommodation have made use of infrared optometers to track the changes in refractive power of the eye [27,31,37,42,113]. This technique possessed the advantage of enabling high temporal sampling frequencies (up to 100 Hz). In contrast, many Shack-Hartmann sensors used for dynamic ocular wavefront measurements have sampling frequencies of less than 20 Hz. An example is the Complete Ophthalmic Analysis System (COAS^{TM}, Wavefront Sciences Inc.), a commercial Shack-Hartmann based ocular wavefront sensor with sampling capability up to approximately 11.5 Hz [16]. Our aberrometer combines good spatial sampling with temporal sampling of up to 173 Hz, and so is well equipped to measure accommodation as well as aberration dynamics.

Accommodation Through a Lens

In Chapter 1 we introduced the concepts of the far point and near point of the eye. These points are different for an eye viewing through an ophthalmic lens than for the eye alone, as the presence of the lens changes the apparent position of the object being viewed. The accommodative demand, i.e., the amount of accommodative amplitude required to focus clearly on an object, is also affected by the introduction of a lens. For example, a myopic subject will find that wearing corrective negative lenses pushes their near point away from the eye, while their far point should ideally be placed at infinity (having previously been located at a finite distance in front of the eye). A detailed discussion of accommodative demand in the presence of correcting lenses is given by Atchison [9].

The Accommodation Signal

To analyse the dynamics of ocular accommodation, we need to compute a quantity from our aberrometer measurements that represents the accommodative response as it varies over time. This quantity can be derived from the temporal expansion of the Zernike aberrations given in Eq. 3.8. Because of the balanced nature of Zernike polynomials (as discussed in Section 1.2), the Zernike spherical aberration in fact combines a spherical aberration (ρ^4) term with a defocus (ρ^2) term in order to minimise the vari-

ance of the aberration across the circular exit pupil [22]. If we consider only Zernike terms up to fourth radial order (i.e., $n = 4$), we can make use of the relation given by Thibos et al. [20] to compute the defocus wave aberration, from which we infer accommodation. We therefore define the *accommodation signal $A(t)$* as follows:

$$A(t) = \frac{4\sqrt{3}}{r^2} \left(c_2^0(t) - \sqrt{15}c_4^0(t) \right) \tag{4.1}$$

where r gives the pupil radius. Thus, the accommodation signal is computed using the Zernike defocus and Zernike spherical aberration terms of the fourth-order expansion. Using a higher order Zernike expansion, one could rewrite Eq. 4.1 to include higher-order terms, such as secondary spherical aberration (c_6^0) [114]. We found that in general, as radial order increased, the amplitude of the Zernike coefficients tended to decrease. Therefore, Zernike coefficients of higher orders suffer greater impact from noise. In the interests of restricting the noise in the accommodation signal, it was decided to compute the accommodation signal only from Zernike terms of up to and including the 4th radial order.

4.2 Context of Study

The main aim of our experiments involving the measurement of accommodation was to investigate the dependence of microfluctuations of accommodation on the mean accommodative effort. The traditional approach to achieving variation of the mean accommodative effort is through variation of the stimulus vergence $V = -\frac{1}{d}$, where d is the distance from the eye to the target in metres. A Badal optical system is often used to allow the vergence to be adjusted without affecting the angular subtence of the target itself [27].

Though early work by Campbell et al. included measurements of microfluctuations at two target vergences [113], the first systematic study of the effects of target vergence on the properties of the microfluctuations was made by Arnulf and Dupuy [115]. The results indicated that the amplitude of microfluctuations are increased as the target vergence is increased. A study by Denieul [42] made use of an infra-red optometer to measure accommodation microfluctuations at several different stimulation vergences, noting the effects of the vergence on the mean accommodative response, microfluctuations, and optical quality of the eye. However, only three subjects were measured, and the spectral analysis only considered the 0-6 Hz range. There appears to be a general consensus that the RMS amplitude of the microfluctuations increases

by a factor of approximately 3-4 over the stimulus range -0.5 to -4 D [27]. Miege and Denieul [38] extended earlier studies by investigating the behaviour of microfluctuations over the full accommodative range. The authors reported that for target vergences closer than -4 D, the amplitude of microfluctuations eventually begins to decrease as the subject's near point is approached. This decrease for very near viewing was also reported by Stark and Atchison [39].

In this research, we aimed to characterise the temporal statistics of microfluctuations of accommodation for different levels of accommodative effort, using the custom-built aberrometer setup shown in Figure 3.2. The goal was to look for consistent trends from subject to subject, independently of their refractive error, in order to characterise some features of the accommodation signal.

4.3 Experimental Setup and Procedure

As with the dynamic aberration measurements described in Chapter 3, all data was collected using the custom-built aberrometer design of Charles Leroux (see Figure 3.2). Since this study was concerned specifically with accommodative effort, the use of translation of the fixation arm was prominent in the experimental procedure.

Experiment Subjects

A total of 9 subjects were included in the accommodation study. All subjects were members of the Applied Optics Group at NUI Galway. The subjects were aged between 26 and 38 years, with a mean age of 29.9 years and standard deviation of 3.4 years. The mean sphere correction required by the subjects was -0.31 D, with a standard deviation of 0.35 D. The mean cylinder correction required by each subject was -0.06 D, with a standard deviation of 0.41 D. None of the subjects had any known relevant ocular pathology. Subject DDB had undergone photorefractive keratectomy (PRK) surgery several years previously. Having been myopic before surgery, subject DDB was now slightly hypermetropic. All other eyes were either emmetropic or slightly myopic. At 38 years of age, subject EL could have been classified as an early presbyope, however the subject was found to have accommodative amplitude that was more than sufficient for the required task and so was admitted to the study.

Experimental Procedure

The general measurement approach we adopted was similar to that of Denieul [42], in that we chose to measure accommodation at a number of vergences within the subject's accommodative amplitude, from the near point to the far point. Analysis would then allow us to distinguish between the characteristics of the accommodation dynamics at different vergences. Our principal results consisted of 4 trials measured at each of the 4 viewing conditions, for all 9 subjects. Performing 4 trials at each viewing condition enabled us to monitor the consistency of the subjects' performance, as well as to perform averaging to reduce the impact of noise on our results.

All experiment trials were carried out with a retinal illuminance in the photopic regime (80 cd m^{-2}). Data was collected from the subject's dominant eye. The non-dominant eye of the subject was covered with an eye patch, and the subject was aligned using a bite-bar for stabilisation. Each measurement trial provided 8,000 data points. The temporal sampling frequency was 173 Hz, meaning each trial was approximately 46.24 s in duration. An active pupil diameter of 3.9 mm was used for all measurements; all subjects were required to have a natural pupil size of greater than this diameter for all viewing conditions. The spatial sampling across the pupil was 250 μm. This corresponded to 15 active lenslets across the diameter of the pupil.

Some subjects reported significant distortion of the retinal image when focusing at the near point. We attributed this at least in part to an increase in astigmatism associated with increased accommodative effort [28]. If required, a cylindrical ophthalmic lens was introduced in the fixation arm (plane P, conjugated with the pupil of the eye) to partially correct for the subject's astigmatism. The lens was chosen according to the subject's cylindrical refractive error, and was oriented by the subject according to their own subjective assessment of best image quality.

Throughout the course of the experiments, we performed measurements at four distinct viewing conditions that were of the greatest interest. We refer to these in our results and analysis as follows:

- **Far Point:** The far position was first found by the subject by manually translating the target away from the Badal lens L_B of the fixation arm. The subject was instructed was to find a comfortable far viewing position.

- **Intermediate Point:** Starting with the far viewing position, we then introduced a -4 D ophthalmic lens in the plane Π. This defined the intermediate point for the trials, which corresponded to comparable accommodative demand for all

subjects (4 D from the subject's far point).

- **Near Point:** The subject's near point was found by directing the subject to translate the target towards L_B. We encouraged the subject to find the limit of his/her accommodative range.

- **Partial Cycloplegia:** This used the same fixation arm position for the far point, but in this case 1 % Tropicamide drops were utilised to induce partial cycloplegia.

Maintaining fixation at the near point for the full duration of the trials proved to be difficult for some subjects. The matter was further complicated by the differing accommodative amplitudes of all the subjects. Preliminary measurements were taken to make sure that the accommodative response at the near point of viewing was at least 1 D greater than for the intermediate point. If the subject was not capable of at least this level of accommodation, they were excluded from the study. For this reason, 2 subjects were excluded from the original group of 11 subjects. Given that the pupil tends to constrict noticeably when viewing at the near point, we monitored the pupil constriction using the pupil imaging camera during measurements to ensure that this effect was maintained during near viewing. If a significant loss in accommodative effort occurred during the trial, or if the subject reported a sudden drop in the retinal image quality, the trial was discarded and repeated.

4.4   Results

Accommodation Signal

From the aberrometer measurements (in the form of Shack-Hartmann CCD frames), we applied the methods described in Section 3.1 to obtain the local wavefront slopes and subsequently the Zernike coefficient values. This gave us a temporal reconstruction of the wavefront aberration as described in Eq. 3.8. The accommodation signals contained blinks at the same times as found in the aberrometer measurements. We removed spurious data points corresponding to instances of blinks, as described in Section 3.2.3. The Zernike coefficient time series were examined for discontinuous or impulsive behaviour, and then the corresponding CCD frames were checked to determine whether or not there was valid input to the sensor. This ensured that analysis was performed only on "clean" signals. A 4th radial order Zernike reconstruction was used in this study. This enabled us to compute the accommodation signal as given in
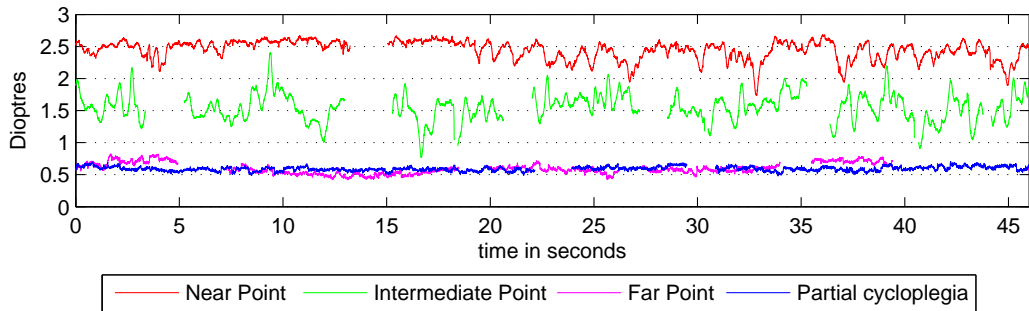
Figure 4.1: Accommodation signals for subject ED at the 4 viewing conditions. During the near point measurement, the subject was unable to fully hold fixation from approximately $t = 19$ s onwards.

Eq. 4.1. Figure 4.1 shows typical accommodation signal measurements recorded for subject ED at each of the 4 viewing conditions. For the near point (red) trace, the amplitude of fluctuations of accommodation are initially noticeably reduced compared to at the intermediate point (green). However, for $t > 19$ s, the difficulty in maintaining this level of effort can be observed. A small relaxation of the accommodative effort leads to increased amplitude of the fluctuations. This is in good agreement with the results of Denieul [42]. For the remainder of the trial, the near point signal exhibited the type of behaviour that we typically would observe at the intermediate point. Changes of behaviour like this within a single trial at the near point were observed quite often, and we consider them to be representative of a separate phenomenon. In general, if a subject was unable to maintain fixation at the near point for the duration of a trial, the trial was repeated. We suggest that the measurement of accommodation in subjects at the near limit of their accommodative range might be better achieved through open view conditions.

Mean Accommodative Effort

Figure 4.2 compares the mean accommodative effort of the 9 subjects at the 3 natural (i.e., without cycloplegia) viewing conditions. The effort performed by all subjects at the far point was on average 0.6 ± 0.4 D (magenta bars), and corresponds to the accommodation lead usually observed for a relaxed accommodative state. At intermediate viewing, the mean effort is 4.1 ± 0.6 D (green). The effort at near viewing corresponds to the maximum accommodative effort that the subject is able to maintain consistently, and is on average 5.9 ± 0.8 D (red).
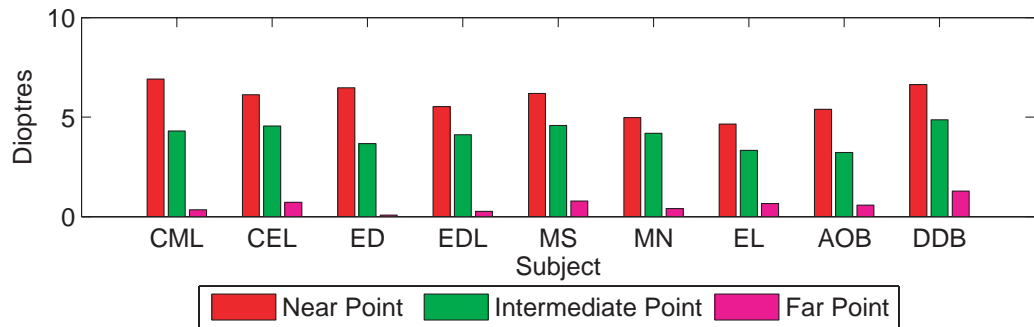
Figure 4.2: Comparison of the mean accommodative effort of the 9 subjects at the 3 natural viewing conditions.

Mean of RMS Fluctuations

A simple approach to quantifying the microfluctuations of accommodation for each measurement trial is to compute the root mean square (RMS) fluctuations of the accommodation signal [38, 39, 42, 43]. This approach does not show much difference between the intermediate and the near point, as we found mean RMS values of 0.18 ± 0.09 D (near), 0.22 ± 0.07 D (intermediate), 0.16 ± 0.05 D (far), and 0.11 ± 0.08 D (partial cycloplegia). The RMS is very sensitive to drifts[1] of the signal, and is consequently not adequate to quantify non-stationary signals, such as those observed at conditions other than the intermediate point. We therefore pursued other methods to quantify our observations, through spectral analysis and assessing the autocorrelation function of the time series increments.

4.5 Analysis

4.5.1 Stationarity

Temporal non-stationarity has been identified as a significant concern in the analysis of aberrometer data [15, 16]. We tested all accommodation measurements for the presence of non-stationarity. The runs test was chosen because as a non-parametric method it does not require any knowledge about the nature of the system, unlike many model-based methods which require an assumption that the data is normally distributed [57]. As discussed in Section 2.1.2, the runs test can be based on many

---

[1]When dealing with other non-stationary physiological signals, such as EEG, it is common to apply low-pass filtering before analysis in order to remove drifts. We considered drifts to be an important part of our measured signals that convey useful information, and so we chose not to remove them.

different sample statistics, e.g., sample mean, sample standard deviation, or mean square error. We chose the sample mean as the statistic for testing the accommodation time-series. Though this test does not conclusively prove non-stationarity, it is a useful indicator, particularly when large amounts of data are available [50]. Alternatively, one can often receive strong indications on whether or not a time series is non-stationary by simply examining the data, and noting the presence of any trends, discontinuities, transients, or impulsive behaviour. Both the runs test and visual inspection approaches were used, and the outcomes are shown in Figure 4.3.
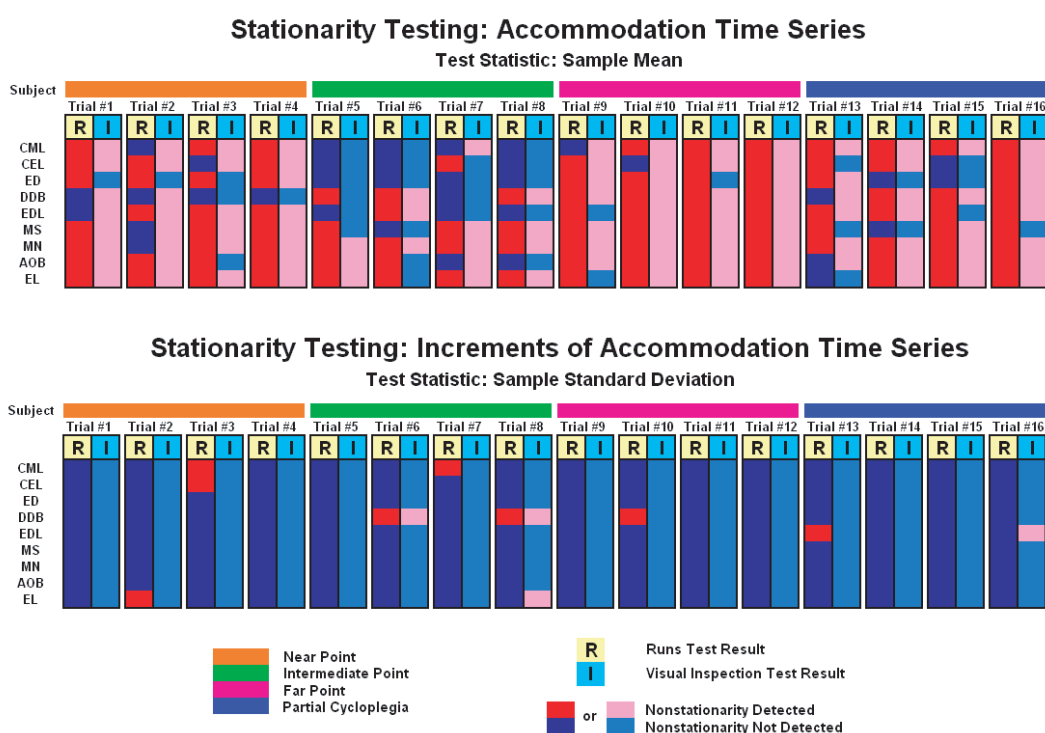
Figure 4.3: Assessing the stationarity of the accommodation measurements.

Given a 99% confidence interval, the runs test detected non-stationarity in 75% of the measured time series, while visual inspection led to the conclusion that 73% were non-stationary. There was an overall discrepancy of 16.7 % between the two testing methods. We note that when subjects were fixating at the intermediate point, only 50% of the measured time series were found to be non-stationary. For the three most experienced subjects (CML, CEL, and ED), only 1 out of 12 trials contained non-stationarity.

As discussed in previous chapters, when dealing non-stationary processes, traditional methods of analysis such as Fourier analysis are of limited use [16, 50]. Also, the autocorrelation cannot be expressed as the function of a single variable, as in Eq. 2.11. Many types of commonly observed non-stationary processes are known to have stationary increments. The increments of a time series can provide information about the underlying physical process, and are useful in the removal of some non-stationary trends [53]. We tested the increments of our measured accommodation time series in the same manner as the raw time series, as seen in Figure 4.3. Given that the increments are generally zero-mean processes, the sample mean was deemed to be an unsuitable choice of statistic in this case, and so the sample standard deviation was used instead. The runs test identified only 8 trials (5%) that were non-stationary, while 4 trials (3%) were deemed to be non-stationary using visual inspection. The discrepancy between the two testing methods was 6%. Thus, we conclude that it is safe to assume that our accommodation measurements were generally non-stationary. However, non-stationarity was generally not detected in the in the increments series.

4.5.2 Spectral Analysis

Despite the fact that accommodation time-series are in general non-stationary, PSD analysis has been used in their analysis by many authors [31,37,39,42,43,101]. In Section 2.2.3 we noted that the PSD can be of limited use when applied to non-stationary processes. It has been suggested however that estimates of the PSD, even for non-stationary processes, are in many cases a legitimate basis for formulating system models for stochastic processes [79]. In practice, statistical characteristics of a measured signal will almost always vary over the duration of interest, at least to some degree. If these variations are minor, then we can assume that measures or transformations computed over the entire duration of the signal still carry useful information. In such situations, it may be more useful to employ Fourier methods and other stationary techniques to analyse the signal, even though it technically does not completely satisfy the conditions for strict or wide-sense stationarity. Reasons include the relative ease and intuitiveness of frequency-domain analysis, compared to alternatives such as time-frequency analysis. Such a simplification can sometimes be more easily justified by analysing only signals of short duration, over which an assumption of stationarity may be more plausible. Ultimately, the decision regarding which types of analysis techniques are appropriate for a particular type of signal may not be clear, and requires individual judgement. In this section, we will demonstrate analysis with and without the assumption of stationarity. This dual approach to the treatment of

ocular dynamics has also been adopted by other researchers [16, 116]. We balance our PSD analysis by also performing time-frequency analysis on the accommodation signals, which gives us a description of the spectral power as a function of both frequency and time, as described in Section 2.2.3.

Estimation of Power Spectral Density

We used the Lomb-Scargle periodogram to estimate the PSD of accommodation signals. This was deemed to be the most suitable method of PSD estimation due to its particular properties, which allow it to be applied to time series with missing data points. All of our time series were afflicted by missing data points, due to blinks. The flexibility in frequency resolution was also a useful feature. Given that 4 measurement trials were taken for each subject at each viewing condition, we made use of periodogram averaging to reduce noise and aid in the interpretation of results.

Periodograms were obtained for each trial. The periodograms were estimated from trials with approximately 27% missing data points on average. The spectra were evaluated at 3,000 uniformly spaced frequencies in the range 0.01-86.5 Hz, however we were most interested in the 0.01-10 Hz region due to the fact that PSD of the accommodative response under all the viewing conditions tends to converge at values of 10 Hz and above [4]. For this reason, we also computed periodograms evaluated at 1,000 uniformly spaced frequencies in the 0.01-10 Hz range. Using the Lomb-Scargle periodogram, this flexibility in frequency resolution could be achieved without having to filter or sub-sample our data. In least-squares spectral analysis, the number of invalid points in the time series does not impact on the resolution, because the spectrum is evaluated at arbitrary frequencies [66].

The fitting of a linear slope to the periodograms can be performed using a linear regression algorithm or the Hill Estimator, as discussed in Section 2.3. However, given the nature of our data, a bilinear fit was more appropriate. A bilinear fit can be performed by adopting a regression approach and imposing a constraint on the regression function [117]. For example, one can fit the line $f(x) = mx + c$ to a curve, with the constraint $f(1) = d$, where m is the slope and c and d are constant values. Thus, the fitted line is constrained to pass through a specified point.

We performed bilinear fits to each of the computed PSD estimates. The starting point of the second line was in each case constrained to coincide with the last point of the first line. This point is then regarded as the breaking point, with its x-intercept deemed the breaking frequency f_{br}. In order to estimate the optimal value of f_{br}, we

performed an iterative process whereby each point between 0.2 Hz and 2.5 Hz was tested as the breaking frequency. We then sought the frequency value for which the RMS fitting error was at a minimum. This value identified our estimate of the optimal breaking frequency $\hat{f}_{opt}$.

Figure 4.4 shows periodograms for 3 subjects on a log-log scale, for frequencies up to 10 Hz. We computed slope fits m_1 and m_2 for two different frequency regions
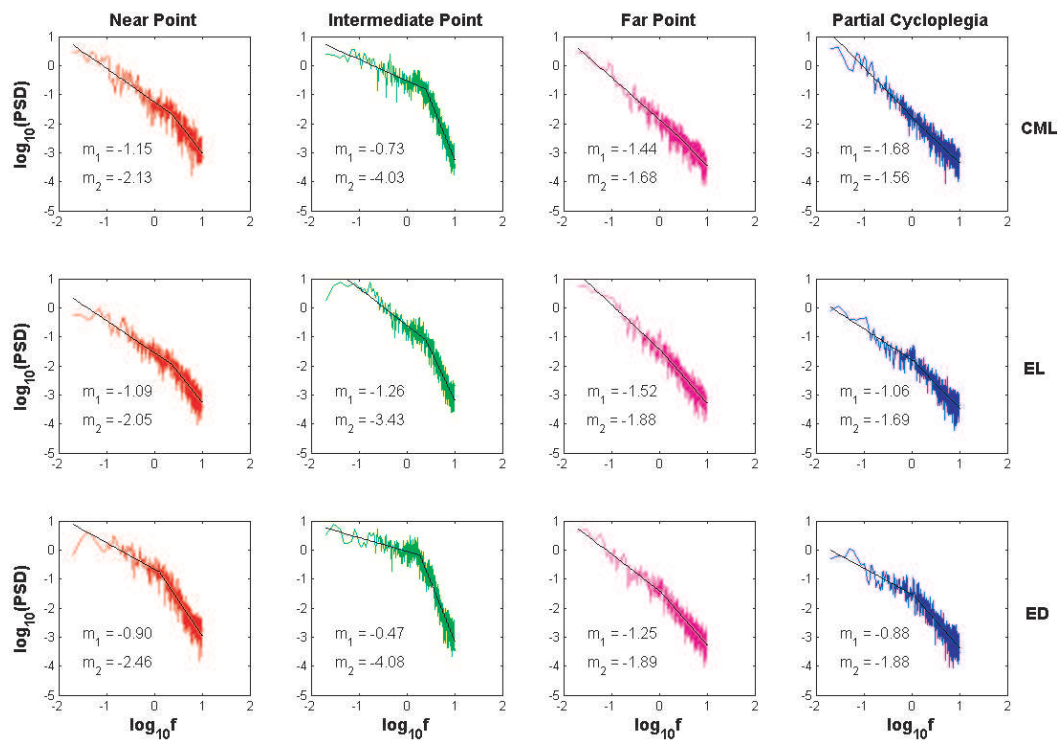
Figure 4.4: Periodograms of the accommodative response for 3 subjects at each of the viewing conditions with fitted slopes. The values m_1 and m_2 denote the fitted slopes for the lower and higher frequency regions respectively.

(i) Below 2 Hz; (ii) 2-10 Hz. Each trace was computed from 4 trials and averaged. Table 4.1 shows the estimated optimal breaking frequency values for all nine subjects at each of the viewing conditions. Table 4.2 shows the fitted slope values for all nine subjects at each of the viewing conditions, along with the average value across subjects. Figure 4.5 shows the periodogram averaged across 8 subjects, with the 4 viewing conditions overlaid on a single plot. Subject DDB was not taken into account in the averaging process, because the periodograms computed for this subject were

Table 4.1: Optimal breaking frequency for the 9 subjects.

Subject	$\hat{f}_{opt,near}$ (Hz)	$\hat{f}_{opt,int}$ (Hz)	$\hat{f}_{opt,far}$ (Hz)	$\hat{f}_{opt,cyc}$ (Hz)
CML	2.38	2.50	2.50	1.90
CEL	0.78	1.87	0.90	2.02
ED	1.26	1.89	1.07	1.09
DDB	0.65	1.72	1.94	2.50
EDL	0.51	1.20	0.83	1.00
MS	1.02	2.10	1.03	1.33
MN	1.66	2.20	1.73	2.50
AOB	1.84	2.27	2.17	2.34
EL	2.28	2.47	1.05	1.11

Table 4.2: Fitted slopes for the 9 subjects.

| Subject	$m_{1,near}$	$m_{2,near}$	$m_{1,int}$	$m_{2,int}$	$m_{1,far}$	$m_{2,far}$	$m_{1,cyc}$	$m_{2,cyc}$
CML	-1.15	-2.13	-0.73	-4.03	-1.44	-1.68	-1.68	-1.56
CEL	-0.98	-2.30	-0.89	-3.89	-1.17	-2.07	-1.16	-2.10
ED	-0.90	-2.46	-0.47	-4.08	-1.25	-1.89	-0.88	-1.88
DDB	-0.23	-1.85	-1.61	-2.50	-1.18	-2.51	-1.43	-1.83
EDL	-0.55	-1.85	-0.48	-3.99	-1.42	-2.39	-1.06	-1.89
MS	-1.09	-2.21	-1.07	-3.57	-1.23	-2.22	-0.61	-1.92
MN	-1.59	-2.27	-1.42	-3.5	-1.71	-2.30	-1.33	-2.84
AOB	-1.24	-2.78	-0.96	-4.14	-1.15	-3.22	-0.96	-3.02
EL	-1.09	-2.05	-1.26	-3.43	-1.52	-1.88	-1.06	-1.69
Average	-0.98	-2.21	-0.99	-3.68	-1.34	-2.24	-1.13	-2.08
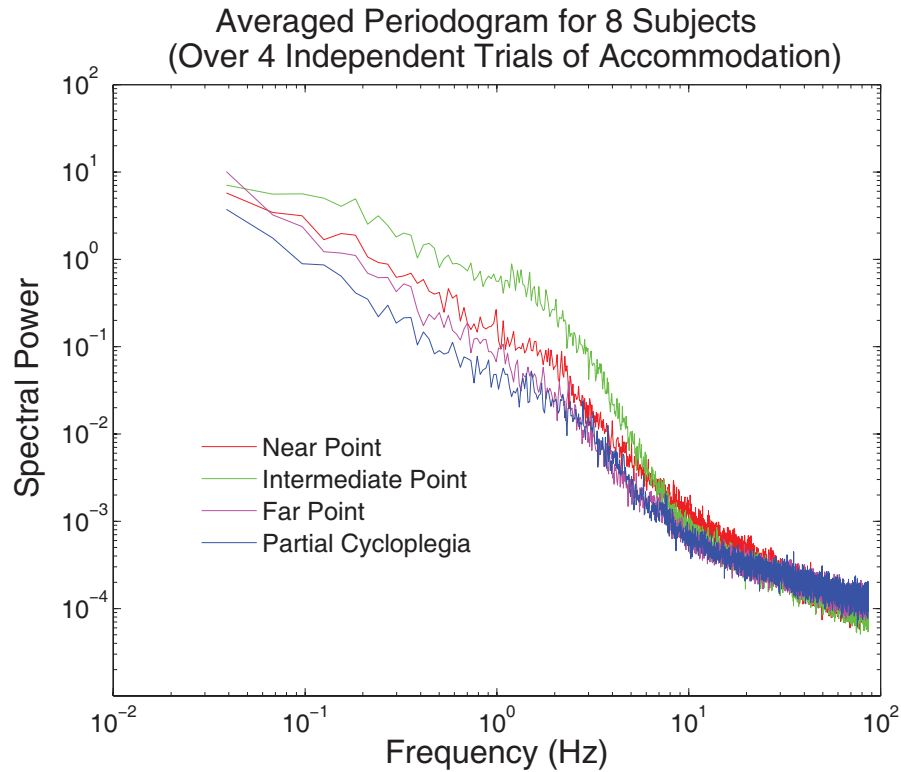
Figure 4.5: Averaged periodograms of the accommodation signal for different accommodative conditions. Each trace represents the average estimated spectral power across 8 subjects.

substantially different to those computed for all the other subjects. The reasons for this are unknown, but may be related to the fact that the subject had previously undergone PRK surgery. PRK changes the bio-mechanical properties of the cornea and can affect tear-film dynamics. It is possible that the differences we observed in the periodograms may be related to the surgery.

Time-Frequency Analysis

We performed time-frequency analysis on the accommodation signals, in order to gain more detailed information about their spectral composition and the extent of the non-stationarity involved. Discontinuities cause problems for time-frequency distributions, and so missing data points due to blinks were replaced by interpolated data (using the Fourier transform method of interpolation [102–104]). Figure 4.6 shows the spectrogram via the short-time Fourier transform (as described by Eq. 2.38) for subject ED from a measurement at the intermediate point. The time domain and frequency
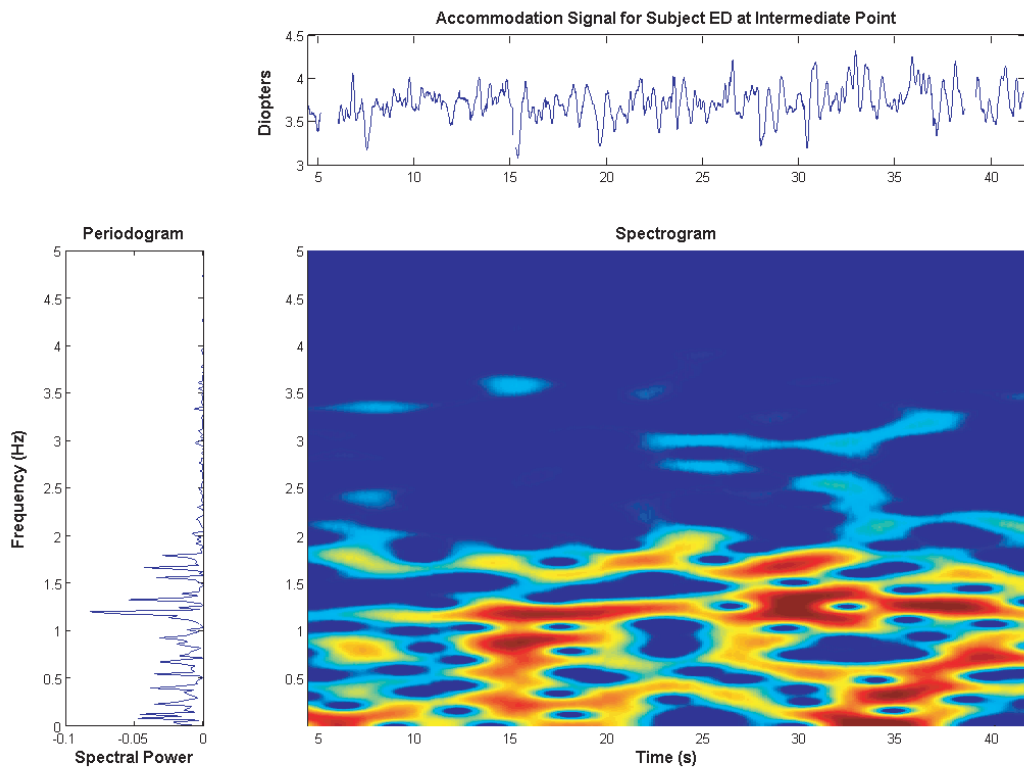
Figure 4.6: Time-frequency analysis using the Short-Time Fourier Transform for Subject ED at the intermediate point. Multiple components can be seen in the 0-5 Hz range. Some appear to vary in frequency, while others suggest the presence of harmonic distortion.

domain (via the Lomb-Scargle periodogram) are also shown. The spectrogram was evaluated at 1,000 uniformly spaced frequencies from 0.005 Hz to 5 Hz using the Goertzel algorithm [106]. A Hamming window of length 1,600 (in samples) was chosen, with 95% overlap. Figure 4.7 gives a time-frequency representation of the same signal as in Figure 4.6, but in this case the ZAM distribution was used.
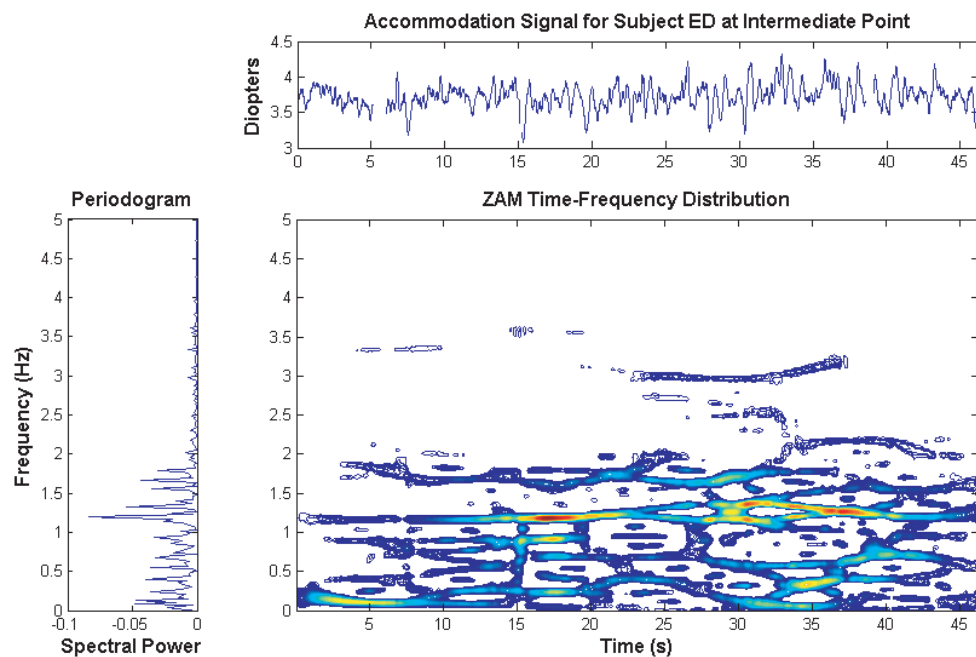

Figure 4.7: Time-frequency analysis using the ZAM distribution for Subject ED at the Intermediate Point. Improved resolution is achieved using the Wigner-Ville based approach as opposed to the STFT based spectrogram.

From the spectrogram and periodogram plots of Figure 4.6, it can be seen that the frequency content of the signal is dominated by components below 2 Hz. The signal appears to be multi-component, containing both components that vary in frequency and those that remain constant. There is also evidence of harmonic distortion, as well as some amplitude modulation. There appears to be an abundance of activity in the 1-1.5 Hz region. This manifests itself as a distinct peak in the periodogram, but in the spectrogram it appears that there may be more than one component involved around the 30-35 s region, while the activity appears to be significantly weaker at other times. All these observations serve to illustrate how time-frequency analysis can give more information than a periodogram alone.

Figure 4.7 illustrates the point that the improvement in resolution obtained through using the ZAM distribution is significant (the advantages of this method were discussed in detail in Section 2.2.3). The time-frequency representation is noticeably improved compared to that obtained using the STFT. Note that the colour scaling is relative, and so we are looking at concentrations of energy in the signal, rather than absolute measures. The finer detail seen using this plot would seem to indicate that a steady component of approximately 1.2 Hz was present in the signal. Given that previous studies have highlighted the presence of heartbeat peaks in the frequency content of accommodation signals [18, 31], and also that the subject's rest heart-rate was approximately 70 beats/minute, we conclude that the 1.2 Hz component is likely to be related to the cardiopulmonary influence.

Figure 4.8 shows the spectrogram for subject ED when measured at the far point. The time trace is visibly affected by slow trends and intermittent behaviour. The pe-
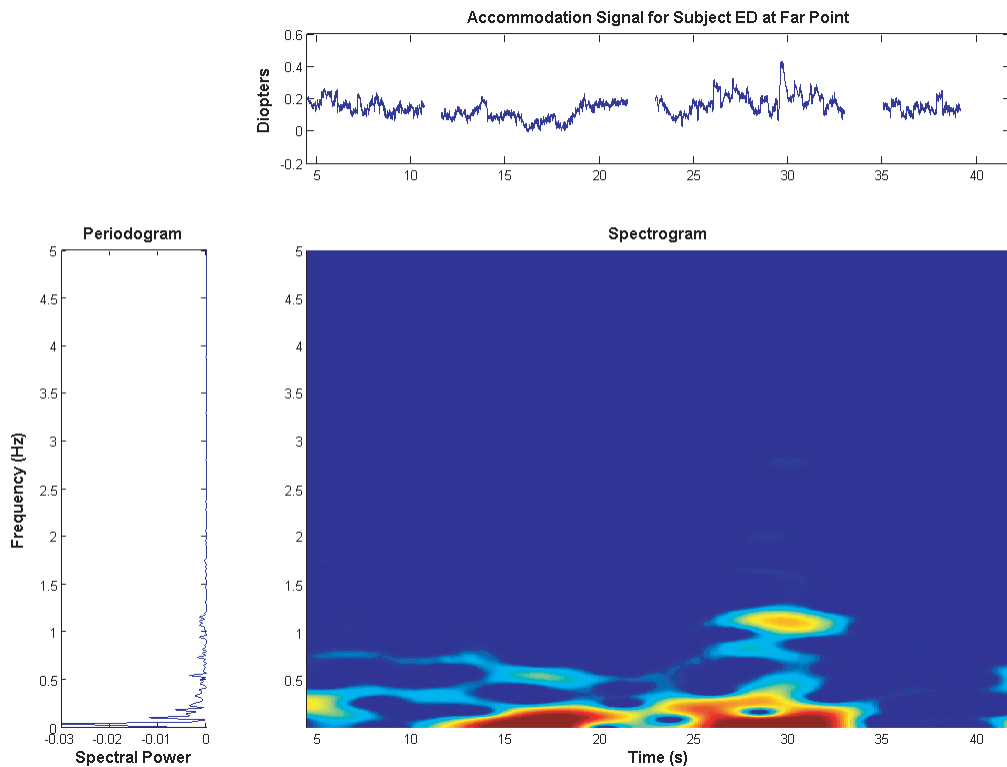

Figure 4.8: Time-frequency analysis using the Short-Time Fourier Transform for Subject ED at the far point. Low-frequency drifts dominate the signal.

riodogram and STFT are consequently dominated by low-frequency content. Some

intermittent behaviour occurring at around 29 s (possibly due to eye movement) produces a burst of high frequency on the STFT. This effect could not easily be identified using the periodogram alone.

4.5.3 Statistical Characteristics

Increments of the Accommodation Signal

Figure 4.9 shows an accommodation signal measured at each of the four viewing conditions for subject AOB. As described previously, taking the increments of accom-
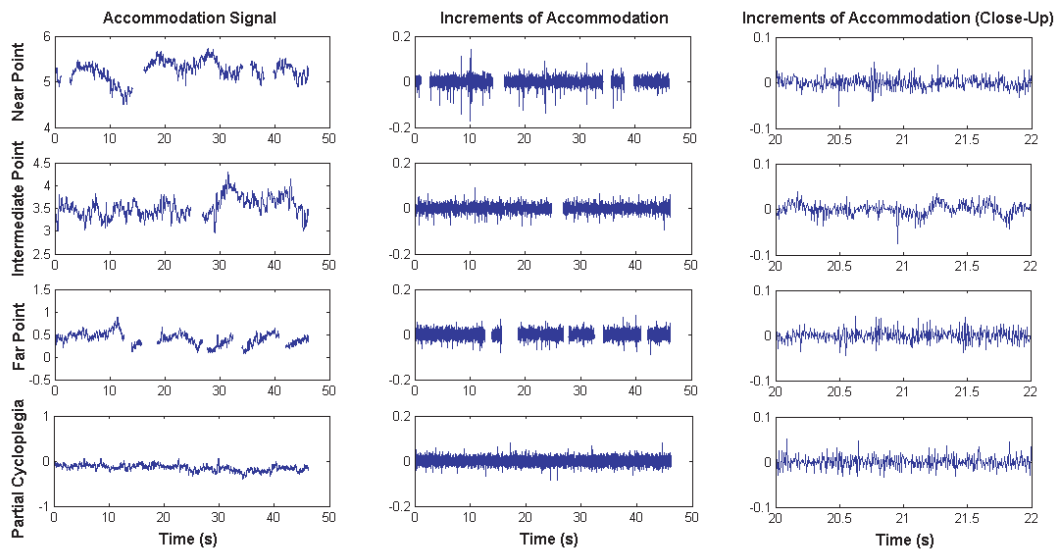
Figure 4.9: Accommodation signals and their corresponding increments for subject AOB, at each of the 4 viewing conditions. A close-up of the increments (showing a period of 2 seconds) is also shown (right).

modation signals typically yields a stationary process. However, it also has the effect of amplifying the higher frequency components in the signal, including noise. The structure of the increments signal differs from the other viewing conditions, as can be seen in the close-up traces. For the near point, far point, and partial cycloplegia cases, positive increments tend to be succeeded by negative ones and vice-versa. This is an indication that there is no significant correlation in the signal, i.e., it is reminiscent of white noise. For the intermediate case, there is a clear structure to the increments signal, which suggests that it is not simply a noise process. This effect was seen to some degree for all subjects, but was most apparent for the three most experienced

subjects (CML, CEL, and ED).

PDF of Increments

We also looked to examine the probability density function (PDF) of the increments in Zernike defocus. We chose to examine the Zernike defocus signal $Z_2^0(t)$ rather than the accommodation signal $A(t)$ in this respect, due to the fact that Zernike spherical aberration Z_4^0 is typically much smaller in amplitude than Zernike defocus, and so is more adversely affected by noise. Eq. 4.1 shows that Z_4^0 is increased in the accommodation signal by a factor of $\sqrt{15}$. Since we were aiming to get a general idea of the shape of the PDF for increments in accommodation, we choose in this case to neglect the spherical term and minimise the effect of noise on the PDF. Figure 4.10 shows normalised PDFs of the increments in Zernike defocus for three subjects at each of the four viewing conditions on a semi-logarithmic scale. Each PDF was computed
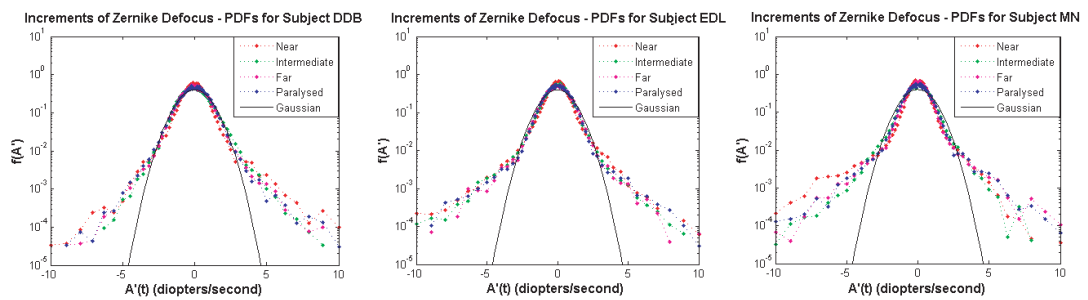

Figure 4.10: PDFs of the increments of Zernike defocus for 3 subjects, at each of the four viewing conditions. A Gaussian PDF with zero mean and unit variance is also shown as a reference, to illustrate that the measured PDFs are non-Gaussian in nature.

using the increments of data from 4 trials collected at that particular viewing condition. A Gaussian PDF with zero mean and unit variance is also shown as a reference. We noted that the PDFs in all cases appeared to be non-Gaussian, exhibiting signs of heavy tails and skewness. Since this effect was noted in all nine subjects included in the study, we attempted to use averaging across subjects to identify any consistent differences between viewing conditions in terms of the shape of the PDF. Figure 4.11 shows the averaged PDF for the nine subjects. The heavy tails are represented clearly, and appear to be significantly more pronounced for near viewing than for the other viewing conditions. Heavy-tailed PDFs suggest that there are many large deviations in the series in question [118]. Thus, our results suggest that the increments of Zernike defocus exhibit more large deviations for near viewing. This can be confirmed by vi-
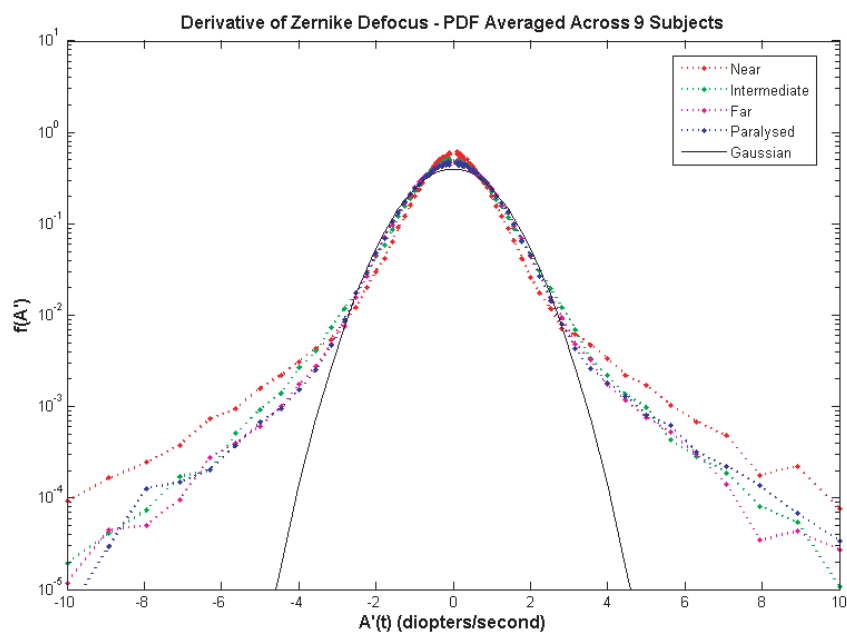
Figure 4.11: PDF of Increments of Zernike defocus, averaged over 9 subjects, at each of the four viewing conditions. A Gaussian PDF with zero mean and unit variance is also shown as a reference, to illustrate that the measured PDFs are non-Gaussian in nature.

sually examining the increments of the Zernike defocus directly, as can be seen in Figure 4.12. There is a relative abundance of large deviations at the near point com-
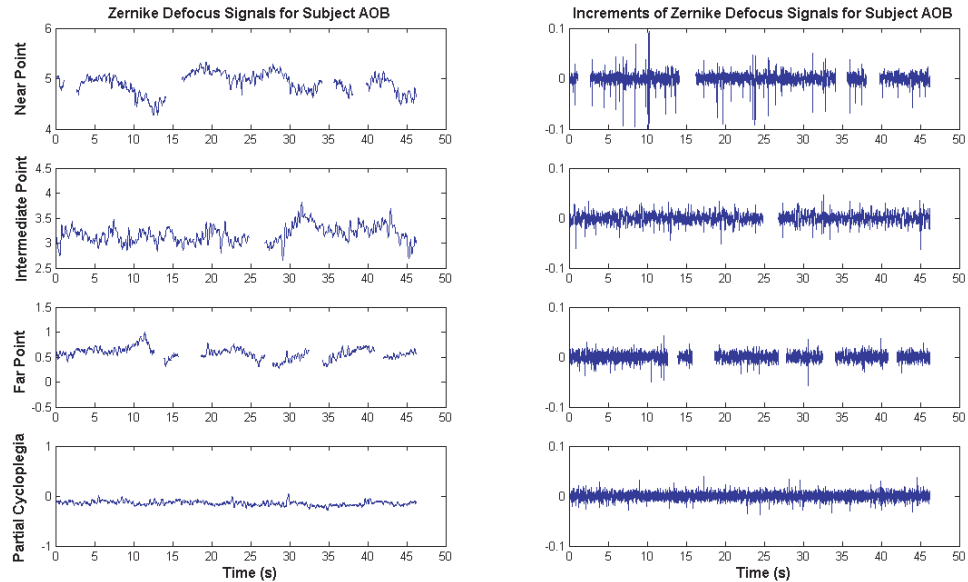
Figure 4.12: Zernike defocus signals and their corresponding increments for subject AOB. The difference in the amount of large deviations observed in the increments series is apparent.

pared to the other viewing conditions. Many of these deviations exceed the standard deviation and would be unlikely to be exhibited by a linear Gaussian process. Large deviations of this kind have been observed in systems with intermittent behaviour, and they are often associated with heavy-tailed[2] processes [118, 119].

Autocorrelation Function of the Increments in Accommodation

We computed the autocorrelation function (ACF) of the increments in our measured signals. In general, the ACF of a signal may be used as a quantitative measure of the memory in the system from which the signal arose [50]. In this study, we computed estimates of the ACF over blocks of 500 samples. This enabled us to obtain multiple estimates from a single trial. Any blocks containing missing data points (due to blinks) were discarded. These estimates were then averaged to give a single ACF estimate for each subject at each viewing condition.

---

[2]"Heavy-tailed" refers to a class of probability density functions whose tail regions are not exponentially bounded. The Lévy-skew alpha-stable distribution is an example of this type of PDF [78].

As described earlier, the Zernike spherical aberration term in Eq. 4.1 can be detrimental if one wishes to minimise noise for analysis purposes. Figure 4.13 shows a comparison of calculating the autocorrelation function of the increments of the accommodation signal, the increments of Zernike defocus, and the increments of Zernike spherical aberration. Again, we concentrate our analysis on increments in defocus
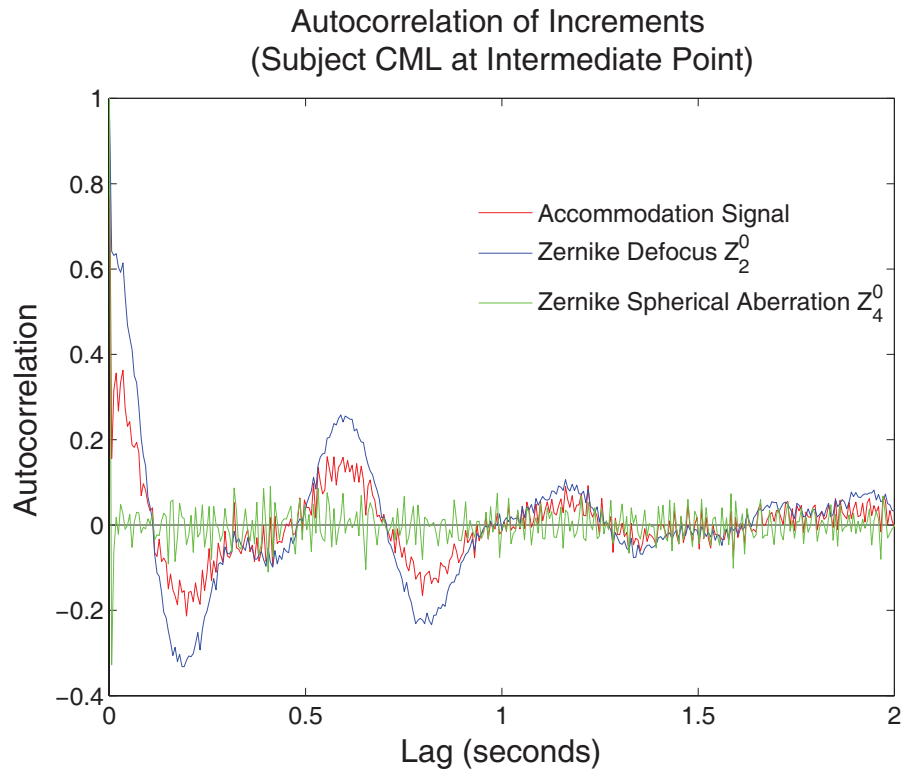
Figure 4.13: Illustration of the effects of noise on the autocorrelation of the increments. The spherical aberration term Z_4^0 is more greatly affected by noise than the Zernike defocus Z_2^0 term.

rather than the accommodation signal $A(t)$. Figure 4.14 shows the normalised ACF of increments of Zernike defocus Z_2^0 for 3 subjects, at each of the 4 viewing conditions. Each plot is averaged over 4 separate trials.

4.6   Conclusions

In this chapter, we have presented measurements of ocular accommodative response, consisting of a large amount of data measured for 9 subjects. We found good repeatability over separate trials, and good consistency in our results from subject to subject
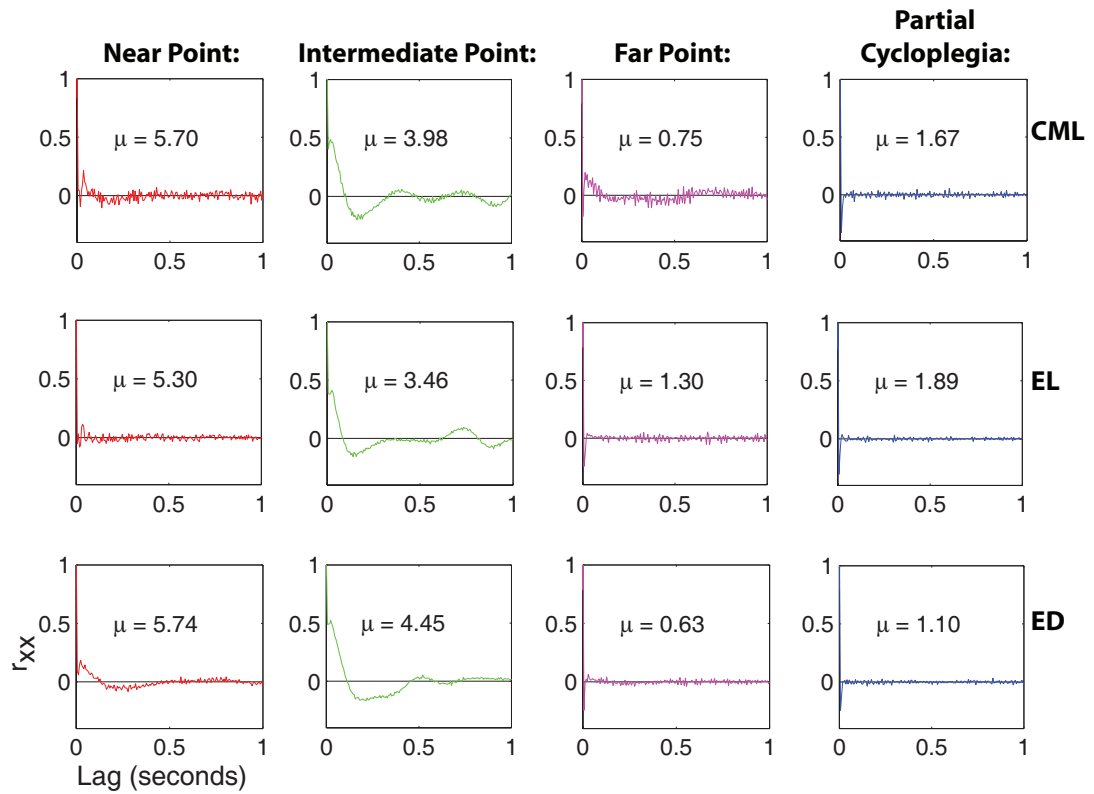
Figure 4.14: Normalised ACF of the increments of Zernike defocus Z_2^0 for 3 subjects at each of the 4 viewing conditions. The mean accommodative effort for each trial (in dioptres) is also shown.

in terms of mean accommodative effort.

Accommodation Signal for Intermediate Viewing

The difference in the shape of the periodogram (Figure 4.4) for the different viewing conditions is still clear after averaging (Figure 4.5). The periodogram for near viewing is comparable in shape to the periodogram for the far viewing condition. At the intermediate point, we computed a systematically more negative slope of the periodogram in the higher frequency region, with an average slope of around -3.68 (on a doubly logarithmic scale). This observation is in agreement with previous studies involving PSD estimates of temporal variations in Zernike defocus [15] and RMS wavefront error [4].

At the far point (and with partial cycloplegia), the values of m_1 are more similar to the values of m_2, with an average value of $m_1 = -1.34$. This is comparable to that obtained for the dynamic aberration measurements in Chapter 3. It is interesting to note that the estimated PSD at the near point is to some degree a mixture of the estimated PSD obtained for the far point and the intermediate point, with a slope of approximately -2 in the higher frequency range. This similarity is illustrated by the averaged PSD estimates (Figure 4.5).

At the intermediate point, we computed a systematically more negative slope of the periodogram in the higher frequency slope range, with an average value of $m_2 = -3.68$. We found average slope values of $m_1 = -1.34$ and $m_2 = -2.24$ for the far point, and $m_1 = -1.13$ and $m_2 = -2.08$ for the partial cycloplegia condition. These slope values are comparable to those obtained in other studies [4, 15, 99].

Looking at the periodogram on a log-log plot emphasises the global shape of the PSD, rather than finer details like peaks associated with the heartbeat and breathing. Such peaks are known to vary in frequency over short periods of time and can be better observed using linear periodogram plots or time-frequency analysis [16].

Non-Stationarity of Temporal Accommodation Signals

The non-stationary behaviour of accommodation signals was illustrated both by the non-parametric test results of Figure 4.3 and the time-frequency analysis (Figures 4.6, 4.7, and 4.8). The time-frequency results also illustrate that the accommodation signals contain multiple components and display non-linear characteristics, such as harmonic distortion and harmonic amplitude modulation.

To quantify the stability of the accommodative signal, some previous authors referred to the amplitude of the low frequency component of the estimated PSD [39,40,44,111]. As mentioned in Chapter 3, for $1/f$-like processes, a power-law exponent in the PSD (on a log-log scale) of greater than unity at low frequencies suggests that the underlying process is non-stationary. Thus, if a process is statistically stable/stationary, one would expect this slope to be less than unity. This fits well with our estimated slopes of the PSD of the accommodation signal for low frequencies (i.e., m_1), which are below or just above unity for most of the 9 subjects. For the three most experienced subjects (CML, CEL, and ED), the value of m_1 is indeed below unity. This suggests that these subjects have a more stable accommodative response at the intermediate point, and this assertion is backed up by the non-parametric tests of Section 4.5.1. It is possible that this improved stability is due to the subjects becoming more adept at the visual task with experience.

As illustrated by Figure 4.1, occasionally a subject struggled to maintain steady-state accommodation at the near limit of their accommodative range (e.g., due to fatigue). This contributes to increased negative slope of the periodogram. As stated previously, subject DDB was found to differ greatly from the other subjects, in that the slope of the periodogram was found to be "flatter" for the near point as well as for the intermediate point. Drifts of the accommodative signal contribute to the < 1 Hz region of the estimated PSD. The relative absence of these components for intermediate viewing suggests that the accommodation signal could be stationary in this case.

Scaling and Long-Term Memory

The fact that there is a piecewise linear relationship between spectral power and frequency on a logarithmic scale (i.e., a $1/f$-type relationship) suggests that the signals may have a degree of self-affinity [50,78,79]. Self-affinity and self-similarity have been reported in the temporal fluctuations of many biological processes, including heartbeat [108], blood pressure [81], and balancing [120]. Many of these diverse physiological processes exhibit power-law behavior in the PSD. This implies that the current value of the signal depends not only on its most recent value but also with its long-term history in a scale-invariant, fractal manner [80]. We observed different slopes in the periodogram depending on the mean accommodative response, in a manner that was consistent from subject to subject. We conclude that the scaling of the microfluctuations is related to the accommodative state of the eye, and is significantly altered when the accommodative system is in its active range, i.e., between the near and far point.

The difference between intermediate viewing and the other viewing conditions can also be seen in the ACF of the increments in accommodative response, as illustrated in Figure 4.14. Slower decay in the ACF suggests longer lasting correlation of the increments of the process for intermediate viewing. This suggests that there is some memory in the process in the case of intermediate viewing [50], whereas for the other viewing conditions the ACF more closely resembles that of a random walk. It appears from Figure 4.13 that the noise on the measured accommodative signal has an important impact on the ACF.

The ACF of the increments of the Zernike defocus Z_2^0 shows a smoother profile and a longer lasting decay than the full accommodative signal, because the noise on the measured spherical aberration Z_4^0 is multiplied by a factor of $\sqrt{15}$ in Equation 4.1. For Z_2^0, we note significant ACF values at lags below 0.1 s (as shown by Figure 4.14), while Figure 4.5 indicates that the estimated PSD of the accommodative response under all the viewing conditions tends to converge at values of 10 Hz and above. It is possible that the memory in the system could play a role in stabilising the accommodative response when the subject is fixating upon a target at their intermediate point.

Chapter 5

Modelling of Dynamic Ocular Aberrations and Accommodation

In Chapter 2, we introduced the topic of signal modelling and discussed some of the general motivations for its use. There are several different motivations behind developing models of ocular aberration and accommodation signals, some of which have been discussed by previous authors. To aid the continued advancements in refractive surgery, it is important to address the fluctuations in the aberrations of the eye [84]. Accurate models of the dynamics could assist in making estimates of these aberrations and the corresponding optimal refractive correction. Such models would also be of interest in the study of the relationship between dynamics and visual performance [4], the development of customised contact lenses [121], and in the design of ocular adaptive optics systems with real-time correction [122].

Signal models of physiological processes are commonplace [50]; however there has been very little research regarding models of dynamic ocular aberrations other than defocus. Iskander et al. [84] proposed a methodology for modelling the dynamics of higher-order ocular aberrations using a parametric, amplitude-modulated, frequency-modulated (AM-FM) approach. This study focused in particular on the spherical

aberration and coma Zernike coefficients. Galetskiy et al. [122] demonstrated a potential application of a model of dynamic aberrations, by employing a deformable mirror to generate aberrations in real time. This approach was dedicated to reproducing aberrations from real measurements; however such a system could also be readily driven by aberration data simulated from a model. A model incorporating realistic spatial and temporal information could be utilised in this way, e.g. for testing of aberrometers, customised contact lenses, or other ophthalmic devices.

A model of the microfluctuations of accommodation has potential use in the study of the perceptual detectability of accommodation microfluctuations. A study by Winn et al. [48] utilised measurements of accommodation microfluctuations to drive a Badal stimulus optometer, while paralysing the subject's accommodation. A stimulus was then presented to the subject. Subjective tests were then performed to determine the perceptual threshold of the accommodation signal, with the authors concluding that the accommodation signal is capable of providing information to the accommodative control system, at least under certain conditions. However, this study included only two subjects and was performed under a limited range of experimental conditions with a simple test of perception. We believe there is scope for further study in this area, and that such studies could be assisted by a dynamic model of accommodation. This would give a standard framework for studies of accommodation dynamics without requiring large databases of measurements.

The association between sustained near accommodative work and the development of myopia, particularly late-onset myopia[1] (LOM), has been well documented [123, 124]. Culhane and Winn [123] showed that LOM subjects exhibit significantly altered dynamic accommodative response to changes in stimulus after sustained near work. Specifically, response times after 3 minutes of sustained near vision were longer than for other groups when the stimulus was changed from near to far. Thus, there is potential for gaining information about subjects' refractive error development based on the dynamics of their accommodative response. This relationship between dynamic accommodation and myopia warrants more study in the form of signal processing and feature extraction, and it is felt that signal modelling could play a useful role.

In this chapter, we discuss signal modelling in the context of ocular aberrations and accommodation. We discuss different modelling strategies, and present a detailed description of a frequency-domain power-law based model. We present results of simulations based on this modelling approach, for both aberration and accommoda-

---

[1]Late-onset myopia is the term applied to be myopia that emerges later in life (e.g. after 15 years of age). It is generally assumed to be environmental in origin rather than hereditary [123].

tion signals. Finally, we present a discussion of possible modifications to the model, and some potential applications.

5.1 ARIMA and Other Parametric Methods

In our initial approach to modelling of dynamic ocular aberration signals, we used ARIMA models, which we described in detail in Section 2.4. We were encouraged to use this approach by several factors:

- ARMA and ARIMA models are well-established and understood tools for modelling and gaining understanding of a wide variety of signals [53], and have been widely used in biomedical signal research [58].

- ARIMA models lend themselves easily to non-stationary processes where the non-stationarity can be removed through differencing. As discussed in Chapter 4, a single order of differencing (or none at all) was sufficient for almost all of our measured signals in order to render them stationary.

- The parameters of ARIMA models can easily be estimated using a wide variety of methods, including the Yule-Walker method discussed in Section 2.4. The resultant models can provide considerable flexibility if the model order is sufficiently high.

- Simulation is easily performed using an ARMA model [125]. Simulation is carried out by seeding Eq. 2.70 with a white noise process $v(n)$. For the ARIMA case, the "undifferenced" simulated sequence $x(n)$ is obtained from $z(n)$ by taking partial sums.

The ARMA/ARIMA approach also has several major drawbacks. These methods attempt to model stochastic signals by approximating the one-dimensional autocorrelation properties of the signal. There is a problem with this ideology when considering the dynamics of ocular aberrations, as the autocorrelation is not expressible as a function of a single variable. On the other hand, given the notion that stationarity can be considered to be a relative term when dealing with non-deterministic processes, and the prevalence of ARIMA models in biomedical signal literature, this was not seen as a decisive argument against their use.

Visual inspection of the results of our ARIMA modelling and simulation indicated at an early stage that the approach suffered from significant limitations. One of the key

problems of this approach with regard to modelling ocular aberration dynamics is the long-term memory associated with these processes (as discussed in Chapters 3 and 4). In particular, a relatively fast decrease in autocorrelation at short lags combined with a slow decline at longer lags is difficult to model with an ARIMA approach. This difficulty is explained in Bruce Ch. 10 [50], in pole-zero model terms[2]. At longer lags, the autocorrelation function of an ARMA process is dominated by the pole closest to the unit circle. However, this pole will lead to slow decay at shorter lags. The ARMA estimation weights errors in the ACF at shorter lags more heavily, and thus the model is likely to underestimate the ACF at higher lags. This conflict makes it difficult to retain significant autocorrelation at short lags while incorporating the slow decay in the ACF at higher lags. Kasdin [79] asserted that an infinite number of poles would be required to reproduce the $1/f$ form with an ARMA representation. The author also pointed out that simulated data generated using these models cannot be scale-invariant, and thus such models cannot incorporate self-similarity.

The parametric AM-FM model described in Eqs. 2.72 and 2.73 was demonstrated to perform well with ocular aberration dynamics when used to fit a model to a small data sample that had undergone low-pass filtering [84]. This method could be well suited to the problem of model-based predictive control, which has previously been proposed for adaptive optics control systems [126], though not specifically for applications relating to the eye. However, to accurately represent the long-term behaviour of ocular aberration dynamics using this model would require a very large model order and thus great computational complexity.

As detailed in Section 2.3.2, signals possessing long-term correlation and $1/f$ behaviour have been observed in many areas of physiology. Given that we have observed similar characteristics in ocular aberration and accommodation signals, it was felt that an alternative signal modelling approach that explicitly incorporates these features is required. This is presented in the following section.

5.2   Power-Law Model

Given all that we have learned about the nature and characteristics of dynamic ocular aberrations and accommodation, and having considered modelling approaches with their respective strengths and weaknesses, we now proceed to develop the best model that we can. The model is based on the assumption of a linear or piecewise-

---

[2]Here we refer to poles and zeros of a z-transform transfer function representation.

linear power law structure of the PSD. Synthesis of signals is based on a modification of an algorithm for the generation of power-law processes or *coloured noise*[3], described by Billah and Shinozuka [127]. This algorithm has also been utilised as the basis of modelling approaches used in the field of EEG research. This is no surprise, given that EEG signals have many similarities to ocular signals in terms of their non-stationarity, power-law form of the spectral density, and dynamic range [128]. In particular, we refer to elements of the non-stationary EEG modelling technique presented by Rankine et al. [129].

The requirements we have for our models of dynamic aberrations and accommodation can be summarised as follows:

- The model should reflect closely the spectral structure of our measured ocular dynamics, i.e., it should have a (piecewise) linear power-law spectral density up to approximately 10 Hz.

- The model should be capable of representing and generating non-stationary signals in the manner of the measured data.

- The model should be capable of accounting for self-affine behaviour.

- As many characteristics of the measured data as possible should be represented in simulated data generated from the model. These include the presence of multiple components, harmonic distortion, amplitude modulation, and frequency modulation.

The piecewise power-law structure of the PSD is one of the most prominent and enduring features of all the aberration and accommodation measurements gathered throughout this thesis, and thus it constitutes a suitable basis for developing the model.

Model Structure

We initially assume that the power spectral density of the process to be modelled can be approximated by a power-law of the form:

$$P(f) \approx \frac{c}{|f|^{\gamma}} \tag{5.1}$$

---

[3]The term "coloured noise" refers to a loose characterisation of certain types of random signals based on the form of their spectral density [79].

where $f = \frac{\omega}{2\pi}$ is the cyclic frequency[4], γ is the power-law exponent, and c is a constant. In general, for a finite-length, continuous-time signal $x(t)$, the power spectral density can be written as [50]

$$P(f) = \frac{1}{T}|X(f)|^2 \tag{5.2}$$

where $X(f)$ is the Fourier transform of $x(t)$. Combining this representation of the PSD with our proposed model, we set

$$P_m(f) = \frac{c}{|f|^\gamma} = \frac{1}{T}|X_m(f)|^2 \tag{5.3}$$

where P_m refers to the modelled PSD. For synthesis, we write $X_m(f)$ in complex exponential form, i.e.,

$$X_m(f) = |X_m(f)|e^{i\arg(X_m(f))} \tag{5.4}$$

The magnitude of $X_m(f)$ can be written as

$$|X_m(f)| = \frac{\sqrt{Tc}}{|f|^{\frac{\gamma}{2}}} \tag{5.5}$$

The *phase spectrum* is given by

$$\arg(X_m(f)) = \phi_m(f) \tag{5.6}$$

This leads us to the following expression for $X_m(f)$:

$$X_m(f) = \frac{\sqrt{Tc}}{|f|^{\frac{\gamma}{2}}}e^{i\phi_m(f)} \tag{5.7}$$

Synthesis of the time-domain signal from $X_m(f)$ can be achieved simply by taking the inverse Fourier transform, i.e.,

$$x_m(t) = \frac{1}{\sqrt{2\pi}}\int_{-\infty}^{\infty} X_m(f)e^{2\pi ift}df \tag{5.8}$$

In practice, the method described above can be implemented on a computer using an FFT algorithm. A detailed discussion of the discrete implementation of the algorithm is given by Billah and Shinozuka [127]. Rankine et al. [129] suggested that the "roughness" of real-world power spectra (as opposed to the "smooth" power-law form of the model) could be approximated by implementing Eq. 5.7 for several different realisa-

---

[4]It is common in signal processing and control theory literature to use the angular frequency ω, but for the sake of clarity we use the cyclic frequency f in this section.

tions of $\phi_m(f)$, and then summing together the resultant synthesised signals in the time-domain.

Parameter Estimation

Perhaps the simplest method to estimate γ from a real signal is to estimate the negative gradient of the linear least-squares fit to a log-log plot of the PSD, with some lower bound f_{min} on the region of power-law behaviour. This approach appears frequently in the literature [77,78]. However, as we discussed in Section 2.3, standard regression approaches can lead to significant bias. The problem can be mitigated somewhat by averaging multiple power spectrum estimates and choosing f_{min} conservatively, however least-squares regression of this type should generally be avoided [77]. As discussed in Section 2.3, the Hill Estimator provides an alternative approach that yields an asymptotically unbiased and consistent estimate. For modelling scenarios where the PSD exhibited a linear slope, we employed the Hill Estimator to compute an estimate of γ.

Billah and Shinozuka [127], as well as Kasdin [79], asserted that the phase spectrum $\phi(f)$ of a $1/f$ process can be assumed to be composed of random phase angles uniformly distributed over the interval $[0,2\pi]$. For simulation purposes, a "surrogate" phase spectrum can thus be provided using uniform random variates. We can therefore choose $\phi_m(f) \propto U(0,1)$ for simulation purposes, where the PDF of the continuous uniform distribution $U(a,b)$ on the interval $[a,b]$ is defined by

$$f(x) = \begin{cases} \frac{1}{b-a} & \text{for } a \leq x \leq b \\ 0 & \text{otherwise} \end{cases} \tag{5.9}$$

Two-Slope Model

As discussed in Chapter 4, the shape of the power spectrum of the accommodation signal is state-dependent, i.e., it varies with the level of accommodative effort. For the cases where the estimated PSD can be well approximated by two separate slopes, we can adapt our model to allow for this. This is achieved simply by rewriting Eq. 5.7, setting $\gamma = \gamma(f)$, with:

$$\gamma(f) = \begin{cases} \gamma_1 & \text{if } f \leq f_{br} \\ \gamma_2 & \text{if } f > f_{br} \end{cases} \tag{5.10}$$

where γ_1 and γ_2 are constants representing estimates of the PSD slope for lower and higher frequencies respectively. The two slope regions are separated by the breaking frequency f_{br}. To estimate γ_1 and γ_2, we employed a constrained bilinear optimal fit to the estimated PSD. This approach was discussed in detail in Section 4.5.2.

The two-slope model allows for good flexibility. Kasdin [79] stipulated that for $1/f$ processes, the stationarity of the process is related to the PSD slope on a log-log plot as follows:

- A value of $\gamma > 1$ at low frequencies implies inherent non-stationarity of the underlying process.

- Conversely, a value of $0 \leq \gamma \leq 1$ at these lower frequencies implies that the process is stationary.

Since γ_1 corresponds to the slope of the lower frequency region of our power spectrum model, the value of γ_1 effectively determines whether or not data generated using the model will be stationary or non-stationary. An illustration of this effect is given in Figure 5.1. The higher frequency slope was fixed to $\gamma = 2$, and an identical random phase spectrum $\phi_m(f) \propto U(0,1)$ was used to generate signals with 5 different values of γ_1. As the value of γ_1 exceeds unity, the non-stationarity of the signals becomes evident via visual inspection (for example, the mean of the process wanders significantly). We can consider the γ_1 value to relate to the "statistical stability" of the signal, rather than to stationarity in the mathematically defined sense. It is useful to think of stationarity in this relative sense, as truly stationary signals are mathematical constructs that do no not strictly occur in real-world data [60].

5.3   Simulation

As discussed previously, PSD estimates of the dynamics of ocular aberrations (when measured at the far point) can be well approximated by a single slope up to approximately 10 Hz. When subjects are accommodating, the PSD estimates of Zernike modes take on a more complex shape [4], which could be better approximated with the two-slope model. Each Zernike mode can be modelled separately, and simulated data from these models can be combined to form a full simulation of wavefront dynamics.

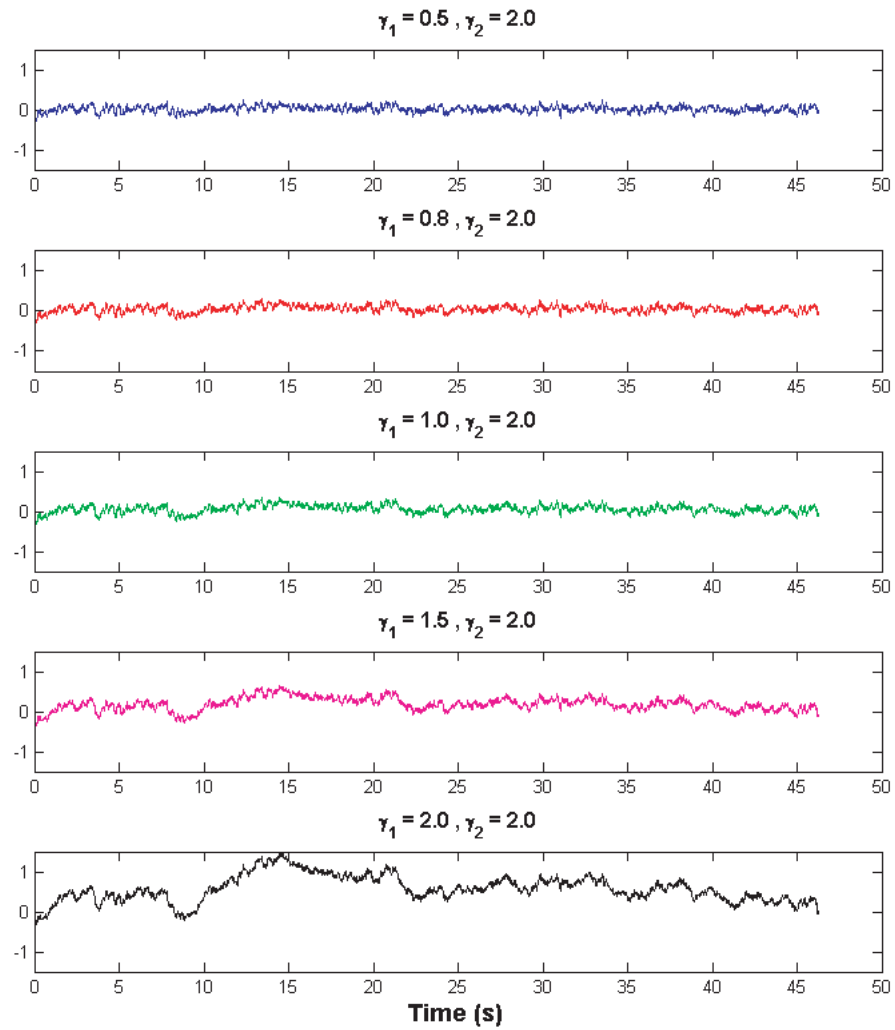The PSD estimates of ocular accommodation signals can be well approximated by a

Figure 5.1: Illustration of the two-slope model, and its relationship to stationarity. All signals were generated using the two-slope model, with identical phase spectrum $\phi_m(f) \propto U(0,1)$. For $\gamma_1 > 1$, non-stationary output was obtained.

single slope at the far point (and in some cases at the near point), but a two-slope structure is often observed, particularly when the subject is viewing in the intermediate range. Thus, the two-slope power-law model is best suited to these cases. From Table 4.2, we noted that there is a strong difference between the two measured PSD slope values m_1 and m_2 for all subjects, when viewing at the intermediate point. The values of m_1 below unity would in particular suggest that the accommodation dynamics tend to be stationary in these cases.

5.4 Validation of the Model

To assess the validity of our model, we generated signals from the model using parameters obtained directly from real data. From a measured signal, we determined the measured phase spectrum, two fitted slope values, and power-law scale factor, and used these as the model parameters $\phi_m(f)$, γ_1, γ_2, and c respectively. We then synthesised a time-domain representation using these model parameters. To justify the use of the model, we must assess its validity. Unfortunately, for non-stationary signal models, no well-established validation methodology exists [83].

In Section 2.2, we introduced the time-frequency coherence function. Time-frequency coherence gives a normalised measure of the cross-correlation between spectral components of two non-stationary processes. If we use measured signals to determine the parameters of our model, we would expect that simulated data generated using this model should have comparable spectral composition to the original signals. Therefore, the time-frequency coherence between the original and simulated signals should demonstrate a significant relationship between the two. With this reasoning, we can use the time-frequency coherence function as an indicator of the performance of our models.

Aberrations Signal Model

Figure 5.2 shows a comparison between a real dynamic aberration signal measurement and a version generated using our model, with the model parameters determined from the original signal. The signal was a single 40 s realisation of Zernike spherical aberration for subject CML. The estimated power-law exponent for this trial was $\hat{\gamma} = 1.6$. Visual inspection of the simulated signal found that it bore much similarity to the original. Periodograms of the real and simulated signals compared well in terms of their overall shape. We also compared the real and modelled signals by
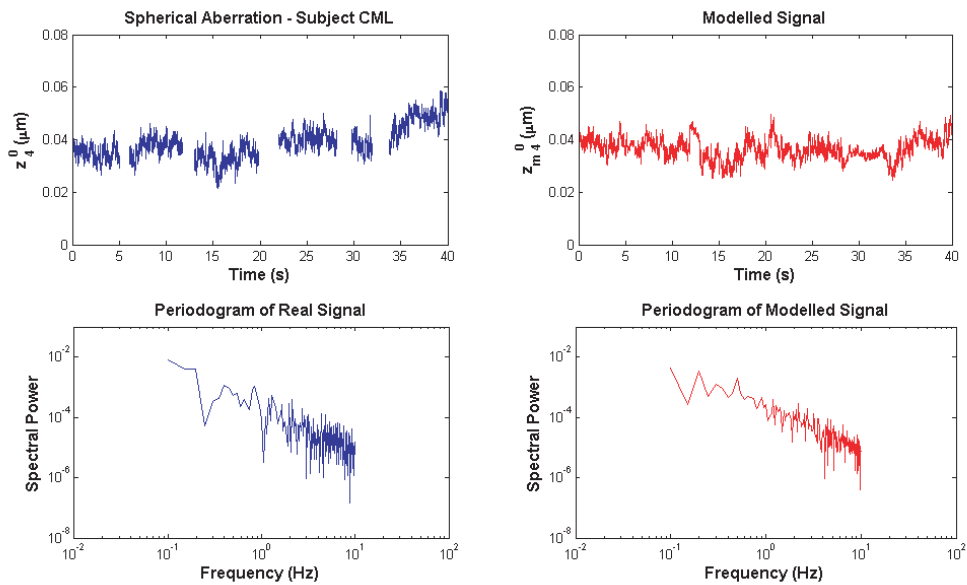
Figure 5.2: Comparison between a realisation of an aberration signal and a version generated using our model, with the model parameters determined from the original signal. The signal is Zernike spherical aberration $c_4^0(t)$ for subject CML.

virtue of their time-frequency coherence. Figure 5.3 shows the time-frequency coherence between the real and modelled signals. The value of the time-frequency coherence function is considerably close to unity for most values of t and ω, and so we conclude that the simulated signal has spectral content that is close to that of the original measured signal from which the model parameters were estimated.

Accommodation Signal Model

Figure 5.4 shows a comparison between a real accommodation signal measurement and a version generated using our model, with the model parameters determined from the original signal. The measurement was of subject ED accommodating at the intermediate point. The estimated power-law exponent values for this trial were $\gamma_1 = 0.3$ and $\gamma_2 = 4.0$. Visual inspection of the simulated signal found it to be in close agreement to the original. Periodograms of the real and simulated signals compared well in terms of their overall shape. We also compared the real and modelled signals by virtue of their time-frequency coherence. Figure 5.5 shows the time-frequency coherence between the real and modelled signals. Again, the value of the time-frequency coherence function is considerably close to unity for most values of t and
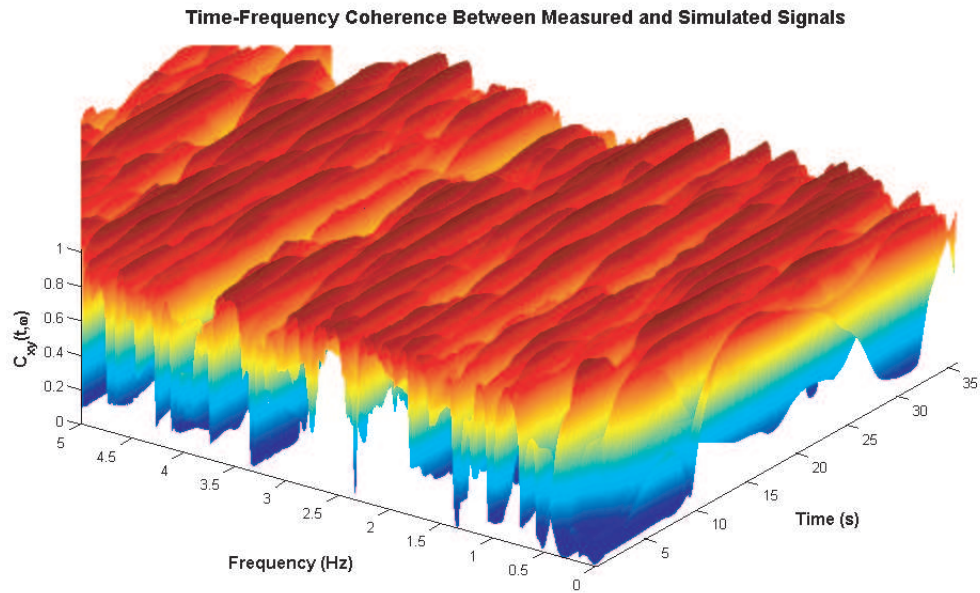
Figure 5.3: Time-frequency coherence between real and simulated signals for Zernike spherical aberration (Subject CML).
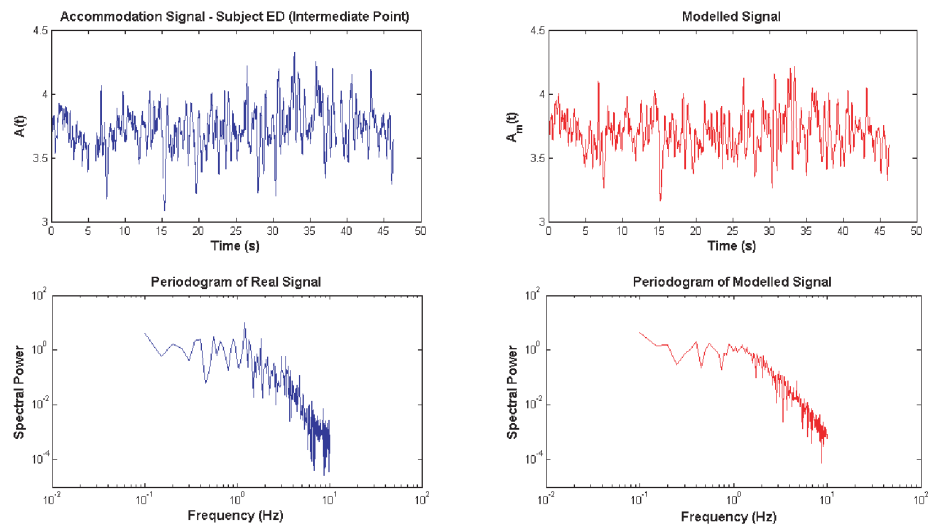

Figure 5.4: Comparison between a real accommodation signal measurement and a version generated using our model, with the model parameters determined from the original signal.
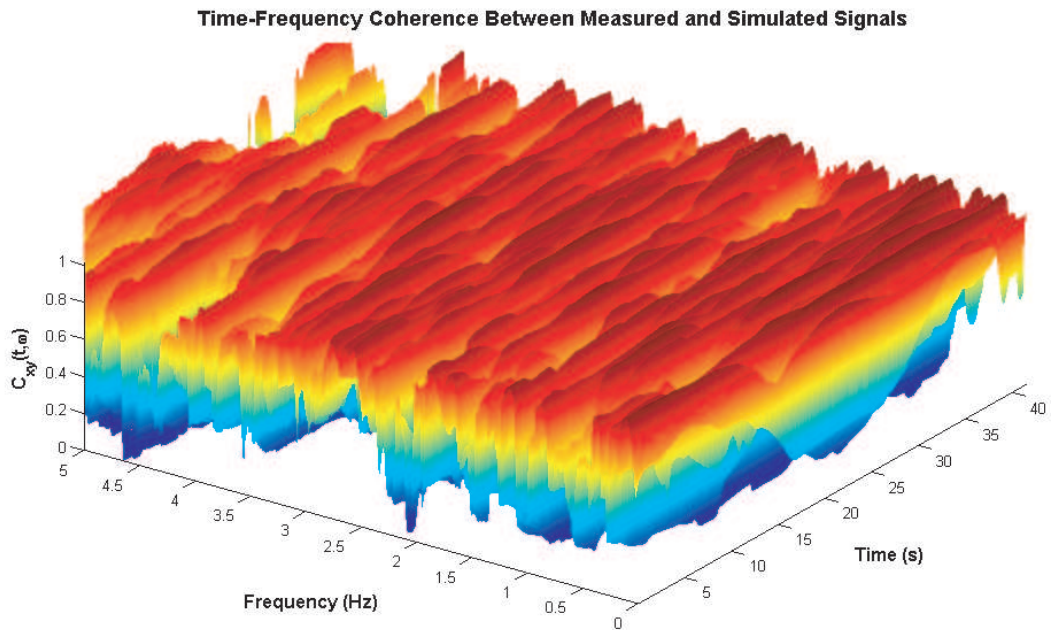
Figure 5.5: Time-frequency coherence between real and simulated accommodation signals for subject ED at the intermediate point.

ω. As with the aberrations signal model previously, we conclude that the simulated signal has spectral content that is close to that of the original measured signal from which the model parameters were estimated.

Modifications to the Model

We have identified several modifications to the model described above, which may be of benefit. Rankine et al. [129] suggested that greater flexibility in modelling of non-stationary data can be achieved by allowing the estimated power-law exponent $\hat{\gamma}$ to be time-varying, i.e., $\hat{\gamma} = \hat{\gamma}(t)$. While we do not agree with the authors that a time-varying exponent is a necessity for modelling and generating non-stationary signals, we have observed that $\hat{\gamma}$ can vary significantly over a single epoch of data. However, by allowing $\hat{\gamma}$ to vary with time in our model, we observed only marginal improvement in the model performance. This could be partly due to the difficulties in validating model performance, however we feel that the potential benefits in allowing $\hat{\gamma}$ to be time-varying must be weighed against some drawbacks. Firstly, the time-scales upon which γ varies significantly are difficult to determine. Secondly, by attempting to estimate γ over shorter time-scales, one must take into account the

additional bias in the estimates[5].

For a single slope model, we made the assumption that the phase spectrum can be modelled by uniform random variates. We carried this approach into the two-slope model, however this may not be a reasonable assumption for the two-slope case. Further study is required: for example, hypothesis testing of the actual measured phase spectra of piecewise-linear slope power-law data to see if they differ significantly from uniform variates.

It has also been proposed that physiological processes exhibiting $1/f$ behaviour can be modelled and simulated using fractional Brownian motion (fBm), a specific type of Gaussian continuous time process. This method has been implemented for EEG by Stevenson et al. [130]. The use of fBm is allows $1/f$ processes to be modelled in such a way that the increments are stationary and normally distributed with zero mean, while taking into account the self-similarity properties. The statistical properties of fBm are well defined, and it may have the advantage of being simpler to implement than our coloured noise-based model.

Application of Models

In this chapter, we have presented a methodology for the simulation of complex non-stationary physiological signals, namely dynamic ocular aberration and accommodation signals. We have demonstrated how the non-stationary and self-affine properties of these signals can be modelled by using a power-law model of the spectral power. Using a method based on coloured noise generation, we then simulated these processes. The simulations produced data whose properties corresponded well to real data in their time, frequency, and time-frequency content.

The model for the dynamics of ocular aberrations was originally conceived as a way to extend static models of aberrations over a large population, such as the model developed by Thibos et al. [19]. If the dynamic model parameters could be similarly estimated over a large population, the authors' idea of creating a database of "virtual eyes" could be extended to include the dynamics of aberrations. A notable feature of the accommodation signal is its dependence on the mean accommodative effort. A model of dynamic accommodation could be extended to include this state-dependence by modelling the relationship between the γ_1, γ_2, and c parameters and the accommodative effort.

---

[5]For asymptotically unbiased estimators (such as the Hill estimator), performing estimation over shorter data lengths increases the bias and is therefore undesirable.

One property that we have not directly addressed in our modelling approach is the non-linearity of aberration and accommodation signals. We previously discussed the presence of harmonic distortion in our measured signals, which suggests the presence of non-linearity. This is not surprising for a physiological process. Non-linearity has been directly addressed in EEG signal models [83], and we feel that proper study of non-linearity in ocular signals is also warranted, e.g., using bispectrum or bicoherence analysis methods.

Chapter 6

Conclusions

In this thesis, we presented a study of the temporal dynamics and statistical characteristics of ocular wavefront aberrations and accommodation. This was achieved using high-performance aberrometer technology. We made use of many analysis tools and methodologies, some of which had not been applied to this type of physiological process previously. We also presented a framework for the modelling and simulation of the dynamic behaviour of ocular wavefront aberrations and accommodation, which is based in part on properties uncovered through our analysis. This Chapter is divided into two sections. Firstly, we will summarise and discuss the findings of our work and their potential applications. We will then discuss topics derived from this work that remained without investigation, but could potentially be addressed by future research.

6.1   Summary of Thesis Work

Non-Stationarity of Ocular Aberrations and Accommodation

One of the recurring issues referred to throughout the course of this thesis was the issue of temporal non-stationarity in the measured aberration and accommodation signals. It had been previously established that ocular aberrations exhibit non-stationary temporal behaviour [15,16], and that accommodation measurements at a subject's far point contain low-frequency drifts [27]. We investigated the matter further by mea-

suring aberrations and accommodation for different levels of accommodative effort, and assessing their stationarity through different methods, to try to establish systematic features.

Our results showed that in the absence of a fixation stimulus, or with a fixation target positioned at the far point, the temporal dynamics of aberrations and accommodation tend to be non-stationary. However, given a fixation stimulus at an intermediate point in the accommodative range, some subjects' aberration and accommodation dynamics showed increased statistical stability, to the point that many measurement trials could be considered to be representative of a stationary process. The results also suggested that experience may be a factor that endows subjects with improved statistical stability in their accommodative response, as a greater number of stationary measurement trials were obtained from the most experienced subjects. The phenomenon of subjects' learning leading to improved performance (and hence altered statistics) in a motor task involving visual input was previously investigated by Cabrera et al. [118], through a series of stick-balancing experiments. Our findings may have implications in areas such as visual performance tests involving ocular adaptive optics.

Influence of Mean Accommodative Effort on Dynamics

We measured accommodation under four different viewing conditions to assess the dependence of the dynamics and statistics of accommodation on the mean level of effort. Previous authors had conducted studies of the effect of stimulus vergence on mean accommodative response [38, 42], however we conducted our analysis by comparing subjects with similar levels of accommodative effort. We endeavoured to look for consistent trends from subject to subject, independent of their refractive error, in order to characterise some features of the signals.

Our results showed differences in the characteristics of the measured accommodation signal depending on the relative accommodative effort. At the intermediate point, we computed a systematically more negative slope of the periodogram in the higher frequency slope range, while at the far point (and with partial cycloplegia) the periodogram could be better fitted by a single straight line over the whole 0.2-10 Hz range. The relatively large size of our sample (9 subjects) compared to previous work enabled us to demonstrate these differences were consistent across subjects.

$1/f$ Scaling of Dynamics

We used a combination of PSD estimation and time-frequency methods to analyse the spectral content of our measured signals. All ocular wavefront sensor measurements of more than a few seconds are afflicted by artifacts due to blinks, but we avoided this problem in our PSD estimation by using the Lomb-Scargle periodogram instead of a standard DFT-based method. This enabled us to estimate the power spectrum of our data with flexible resolution and without artificially introducing interpolated data. To our knowledge, this is the first time that this method has been applied in studies of ocular dynamics, though it has been applied to other physiological signals [131]. We identified signs of $1/f$ behaviour in the aberration and accommodation signals. This is known to be a feature of processes that exhibit self-affine behaviour, and has been identified in many other physiological processes (See Section 4.6), including the heartbeat [82, 108, 132]. This is of particular interest, as the heartbeat is known to correlate with aberration dynamics [18].

Long-Term Dependence of Accommodation

$1/f$ processes are associated with long-term dependence [78, 80]. This means that the current value of the signal depends not only on its most recent value but also on its long-term history. We examined the autocorrelation function of the increments in accommodation, due to the fact that in general the ACF of a signal may be interpreted as a measure of the memory in the system from which the signal arose [50]. We observed notable differences between the ACF of the increments at the intermediate point when compared to all the other viewing conditions (which resembled that of a random walk, i.e. with no discernible correlation at lags other than zero). It is difficult to draw conclusions from this presence of long-term correlation for the intermediate point case, but it appears that the dynamics of the accommodation system are quite different for intermediate viewing, compared to viewing at the far point or even at the near point. It is also possible that the memory in the system could play some active role in stabilising the accommodative response when the subject is viewing targets at their intermediate point.

Potential Use for Models of Ocular Wavefront Dynamics

We presented a methodology for constructing models of the temporal dynamics of ocular aberrations and accommodation. These models demonstrate a general framework that could be adapted for several applications. Roberts [133] asserted that mea-

suring and understanding the dynamic performance of the eye is critical to the future development of advanced customised refractive surgeries, which is in itself important for generating an overall improvement of refractive surgery results. Therefore, any improvements in the measurement and modelling of dynamic aberrations could be beneficial in areas such as the development of customised laser ablation algorithms for refractive surgery. It has also been suggested that models of dynamic aberrations could be adapted to aid in the testing of aberrometer designs, ocular adaptive optics systems, or customised contact lenses [122].

6.2 Proposal of Further Work

Improvements in Modelling of Aberrations and Accommodation

One of the key elements of accommodation we have explored in this thesis is that its statistical properties are *state-dependent*, i.e., the accommodation signal depends on the mean level. We developed a model that can give an accurate representation of these statistics for a given state. However, the model could be made more powerful by explicitly specifying the relationship between the dynamic model parameters and the level of accommodative effort. As we discussed in Section 5.4, a combination of the dynamic model of aberrations with a static population model would also be a significant improvement.

The dynamics of ocular wavefront aberrations and accommodation are significantly influenced by pulse and respiration [18, 33, 95]. Ideally, this relationship should be factored into any model of aberration and accommodation signals. We did not explicitly model the cardiopulmonary dynamics in our approach. They were not excluded however, as our model is based on the overall shape of the PSD in the 0.1-10 Hz range, which encompasses the contribution of pulse and respiration effects. A modelling approach that addresses the cardiopulmonary dynamics in a more direct manner would give scope for improvement in accuracy. Another possible extension to the model is the simulation of interference in the signals due to subjects' blinking, including the associated transient behaviour of the tear film.

The Role of Microfluctuations in the Control of Accommodation

As we discussed in Section 1.3, a role for the microfluctuations of accommodation has been proposed by many authors [27, 37, 43, 47]. We hoped to contribute to this area

of research by employing hardware and analysis techniques that had not previously been utilised in the field of study. Winn et al. [31] performed experiments to determine the perceptual detectability of the microfluctuations by presenting a stimulus modulated by measured accommodation signals to a subject under cycloplegia. This study examined only 3 subjects and used accommodation measurements made with a -4 D demand only, to modulate the stimulus.

We believe there is potential for our modelling and simulation techniques to be used in an updated study of the perceptual detectability of microfluctuations. The original study used RMS values to quantify the threshold for detection of the microfluctuations, with the authors noting that the threshold value required was very similar to the RMS of the measured response. This was an important result, which suggested that the microfluctuations are capable of providing information to control accommodation without the need for any sub-threshold control mechanism. However, as we discussed in Section 4.4, the RMS can be a misleading quantity when dealing with signals that may be non-stationary. We have also demonstrated that the spectral power and statistical characteristics of the microfluctuations in accommodation can vary considerably depending on the level of accommodative effort. Our model could be adapted to provide simulated data that would more accurately reflect the statistical nature of the accommodation signal, and under several different accommodative states as opposed to just one. Combined with a larger number of subjects, this could lead to an interesting follow-up study to that of Winn et al. [48].

Accommodation Dynamics and the Development of Myopia

In Chapter 5, we discussed the association between sustained periods of near viewing requiring high levels of accommodation and the development of myopia. It has been shown that late-onset myopia (LOM) subjects exhibit differences in accommodative response to sustained near visual tasks when compared to emmetropes. In particular, regression times from near to far after several minutes of near viewing have been shown to be significantly longer for LOM subjects [123]. It has been proposed that an anomaly in the accommodative control system may be a precursor to the development of myopia. Gilmartin and Bullimore [124] have stated that it may be possible to identify predisposing factors in young emmetropes that may indicate the potential for LOM. Such findings could be used to improve the efficacy of treatment. Many of the studies in this area have so far focused on the response of the accommodation system to changes in stimulus demand. A possible future study could compare the temporal and statistical characteristics of the accommodative response for emmetropic and

LOM subjects, with tasks involving a fixed stimulus (i.e., steady-state conditions), in order to determine if there are any discernible differences between LOM and emmetropic subjects under similar levels of relative accommodative effort.

Appendix A: List of Symbols

A	Accommodation signal
a_k	Autoregressive model parameters
b_k	Moving average model parameters
C_{xx}	Autocovariance function
c	Power-law scaling exponent
c_n^m	Zernike coefficient
E	Expected value operator
F	Cumulative distribution function
$\mathcal{F}$	Fourier transform operator
f	Probability density function, cyclic frequency
r	Radial distance
H	Transfer function in z-domain
I	Irradiance distribution
i	Imaginary unit $i = \sqrt{-1}$
M	Wavefront sensor slope matrix
m	Sample lag
m_i	Slope value
N	Series length
n	Refractive index

P_{xx}	Power spectral density
P_{xy}	Cross-spectral density
R	Reconstructor matrix
R_n^m	Radial polynomials
R_{xx}	Autocorrelation function
R_{xy}	Cross-correlation function
r	Radial distance
r_{xx}	Autocorrelation coefficient
T	Time period
t	Time
U	Uniform distribution
u	Complex amplitude of wave function
W	Wave aberration
$\mathcal{W}$	Time-frequency distribution
w	Window function
Z_n^m	Zernike circle polynomials
z	Position along the optical axis
α	Power-law exponent
Γ_{xy}	Coherence function
γ	Slope of spectral density
Δ	Difference operator
δ_{m_0}	Kronecker delta function
ϵ	Modelling error
ϵ_p	Prediction error
η	Outcome of stochastic process
θ	Azimuthal angle co-ordinate
λ	Wavelength
μ	Mean
μ_t	Time average
ν	White noise disturbance
ρ	Radial co-ordinate

ρ_c	Centroid
σ	Standard deviation
τ	Time lag
τ_c	Correlation time
Φ	Smoothing kernel function
ϕ	Phase angle
ω	Angular frequency

Appendix B: Glossary

ACF	Autocorrelation function
AM	Amplitude modulation
ANSI	American National Standards Institute
AR	Autoregressive
ARIMA	Autoregressive integrated moving average
ARMA	Autoregressive moving average
CCD	Charge-coupled device
CDF	Cumulative distribution function
CMOS	Complimentary metal-oxide-semiconductor
FBM	Fractional Brownian motion
FM	Frequency modulation
DFT	Discrete Fourier transform
ECG	Electrocardiogram
EEG	Electroencephalogram
FFT	Fast Fourier transform
LED	Light-emitting diode
LOM	Late-onset myopia
LSSA	Least-squares spectral analysis

LTI	Linear time-invariant
PDF	Probability density function
PRK	Photorefractive keratectomy
PSD	Power spectral density
RMS	Root mean square
STFT	Short-Term Fourier transform
TFR	Time-frequency representation
WSS	Wide-sense stationary
ZAM	Zhao-Atlas-Marks

Bibliography

[1] T. Young. On the mechanism of the eye. *Phil. Trans.*, 92(1):23–88, 1801.

[2] A. Gullstrand. *Handbuch der Physiologischen Optik*. Voss, Hamburg, 1909.

[3] E. Dalimier. *Adaptive Optics Correction of Ocular Higher-Order Aberrations and the Effects on Functional Vision*. PhD thesis, National University of Ireland, Galway, 2007.

[4] A. Mira-Agudelo, L. Lundström, and P. Artal. Temporal dynamics of ocular aberrations: Monocular vs binocular vision. *Ophthal. Physiol. Opt.*, 29:256–263, 2009.

[5] P. Artal, A. Benito, and J. Tabernero. The human eye is an example of robust optical design. *J. Vis.*, 6(1):1–7, 2006.

[6] D. Dursun, D. Monroy, R. Knighton, T. Tervo, M. Vesaluoma, K. Carraway, W. Feuer, and S.C. Pflugfelder. The effects of experimental tear film removal on corneal surface regularity and barrier function. *Ophthalmology*, 107(9):1754–1760, 2000.

[7] A. Dubra. *A Shearing Interferometer for the Evaluation of Human Tear Film Topography*. PhD thesis, Imperial College, London, 2004.

[8] R. Montés-Micó, J.L. Alió, and W.N. Charman. Dynamic changes in the tear film in dry eyes. *Invest. Ophthalmol. Vis. Sci.*, 46(5):1615–1619, 2005.

[9] D.A. Atchison and G. Smith. *Optics of the Human Eye*. Butterworth-Heinemann, 2002.

[10] H.A. Weeber. *Mechanics of Human Accommodation and Presbyopia*. Ponsen & Looijen B.V., 2008.

[11] I.E. Loewenfeld. *The Pupil: Anatomy, Physiology, and Clinical Applications*. Iowa State University Press, 1993.

[12] H. Gross, editor. *Handbook of Optical Systems*. Wiley-VCH, 2005.

[13] V.N. Mahajan. *Aberration Theory Made Simple*. SPIE Press, 1991.

[14] L. Diaz-Santana, V. Guériaux, G. Arden, and S. Gruppetta. New methodology to measure the dynamics of ocular wave front aberrations during small amplitude changes of accommodation. *Opt. Express*, 15:5649–5663, 2007.

[15] H. Hofer, P. Artal, and D.R. Williams. Dynamics of the eye's wave aberration. *J. Opt. Soc. Am. A.*, 18:497–506, 2001.

[16] D.R. Iskander, M. Collins, M. Morelande, and M. Zhu. Analyzing the dynamic wavefront aberrations in the human eye. *IEEE Trans. Biomed. Eng*, 51:1969–1980, 2004.

[17] K. Hampson, E. Mallen, and J.C Dainty. Coherence function analysis of the higher-order aberrations of the human eye. *Opt. Lett.*, 31:184–186, 2006.

[18] M. Zhu, M.J. Collins, and D.R. Iskander. Microfluctuations of wavefront aberrations of the eye. *Opthal. Physiol. Opt.*, 24:562–571, 2004.

[19] L.N. Thibos, A. Bradley, and X. Hong. A statistical model of the aberration structure of normal, well-corrected eyes. *Ophthal. Physiol. Opt.*, 22:427–433, 2002.

[20] L.N. Thibos, X. Hong, A. Bradley, and X. Cheng. Statistical variation of aberration structure and image quality in a normal population of healthy eyes. *J. Opt. Soc. Am. A*, 19(12):2329–2348, 2002.

[21] D. Merino. *Adaptive Optics for Optical Coherence Tomography*. PhD thesis, National University of Ireland, Galway, 2007.

[22] V.N. Mahajan. *Optical Imaging and Aberrations*. SPIE Press, 1998.

[23] L.N. Thibos, R.A. Applegate, J.T. Schweigerling, R. Webb, and VSIA Standards Taskforce Members. Standards for reporting the optical aberrations of the eye. *J. Ref. Surg.*, 18:652–660, 2002.

[24] G.M. Dai. *Wavefront Optics for Vision Correction*. SPIE Press, 2008.

[25] D.R. Iskander, B.A. Davis, M.J. Collins, and R. Franklin. Objective refraction from monochromatic wavefront aberrations via Zernike power polynomials. *Ophthal. Physiol. Opt.*, 27(3):245–255, 2007.

[26] J. Porter, A. Guirao, I. G. Cox, and D. R. Williams. Monochromatic aberrations of the human eye in a large population. *J. Opt. Soc. Am. A*, 18(8):1793–1803, 2001.

[27] W.N. Charman and G. Heron. Fluctuations in accommodation: a review. *Opthal. Physiol. Opt.*, 8:153–164, 1988.

[28] S. Plainis, H. Ginis, and A. Pallikaris. The effect of ocular aberrations on steady-state errors of accommodative response. *J. Vis.*, 5:466–477, 2005.

[29] S. Gruppetta, F. Lacombe, and P. Puget. Study of the dynamic aberrations of the human tear film. *Opt. Express*, 13:7631–7636, 2005.

[30] K.Y. Li and G. Yoon. Changes in aberrations and retinal image quality due to tear film dynamics. *Opt. Express*, 14:12552–12559, 2006.

[31] B. Winn, J.R. Pugh, B. Gilmartin, and H. Owens. Arterial pulse modulates steady-state ocular accommodation. *Curr. Eye Res.*, 9(10):970–975, 1990.

[32] L.F. Schmetterer, F. Lexer, C.J. Unfried, H. Sattmann, and A.F. Fercher. Topical measurement of fundus pulsations. *Opt. Eng.*, 34(3):711–716, 1995.

[33] K. Hampson, I. Munro, C. Paterson, and J.C. Dainty. Weak correlation between the aberration dynamics of the human eye and the cardiopulmonary system. *J. Opt. Soc. Am. A.*, 22:1241–1250, 2005.

[34] C. Scheiner. *Oculus, hoc est: fundamentum opticum*. Innsbruck, 1619.

[35] R.A. Schachar. Cause and treatment of presbyopia with a method for increasing the amplitude of accomdation. *Ann. Ophthalmol.*, 24:445–447,452, 1992.

[36] J.L. Ungerer. Problems and solutions in the optometric management of presbyopic airline pilots. Master's thesis, College of Optimetry, University of Melbourne, 1986.

[37] F.W. Campbell, J.G. Robson, and G. Westheimer. Fluctuations of accommodation under steady viewing conditions. *J. Physiol.*, 3(145):579–594, 1959.

[38] C. Miege and P. Denieul. Mean response and oscillations of accommodation for various stimulus vergences in relation to accommodation feedback control. *Ophthal. Physiol. Opt.*, 8(2):165–171, 1988.

[39] L.R. Stark and D.A. Atchison. Pupil size, mean accommodation response and the fluctuations of accommodation. *Opthal. Physiol. Opt.*, 17(4):316–3223, 1997.

[40] M. Alpern. Variability of accommodation during steady fixation at various levels of illuminance. *J. Opt. Soc. Am.*, 48(3):193–197, 1958.

[41] L. Stark, Y. Takahashi, and G. Zames. Nonlinear servoanalysis of human lens accommodation. *IEEE Trans. Syst. Sci. Cybern.*, 1 (1):75–83, 1965.

[42] P. Denieul. Effects of stimulus vergence on mean accommodation response, microfluctuations of accommodation and optical quality of the human eye. *Vision Res.*, 22(15):561 – 569, 1983.

[43] J.C. Kotulak and C.M. Schor. Temporal variations in accommodation during steady-state conditions. *J. Opt. Soc. Am. A*, 3(2):223–227, 1986.

[44] L.S. Gray, B. Winn, and B. Gilmartin. Accommodative microfluctuations and pupil diameter. *Vision Res.*, 33(15):2083 – 2090, 1993.

[45] P.A. Ward and W.N. Charman. Effect of pupil size on steady state accommodation. *Vision Res.*, 25:1317–1326, 1985.

[46] H.D. Crane. A theoretical analysis of the visual accommodation system in humans. report NASA CR-606. Technical report, NASA, Washington D.C., 1966.

[47] J.C. Kotulak and C.M. Schor. A computational model of the error detector of human visual accommodation. *Biol. Cybern.*, 54:189–194, 1986.

[48] B. Winn, W.N. Charman, J.R. Pugh, G. Heron, and A.S. Eadie. Perceptual detectability of ocular accommodation microfluctuations. *J. Opt. Soc. Am. A*, 6(3):459–462, 1989.

[49] K. Najarian and R. Splinter. *Biomedical Signal and Image Processing*. Taylor & Francis, 2006.

[50] E.N. Bruce. *Biomedical Signal Processing and Signal Modeling*. Wiley Series in Telecommunications and Signal Processing, 2001.

[51] A. Papoulis. *Probability, Random Variables, and Stochastic Processes*. WCB McGraw-Hill, 1991.

[52] J.C. Dainty. Lectures in probability, random variables, and stochastic processes, 2007.

[53] G.E.P. Box and G.M. Jenkins. *Time Series Analysis, Forecasting and Control.* Holden-Day, San Francisco, California, 1970.

[54] M.R. Masliah. Stationary/nonstationary identification.

[55] K. Kant and M. Venkatachalam. Characterizing non-stationarity in the presence of long-range dependence, 2001.

[56] Y. Grenier. Time-dependent ARMA modeling of nonstationary signals. *IEEE Trans. Acoust. Speech Signal Process.*, 31:899–911, 1983.

[57] R.M. Bethea and A.G. Piersol. *Applied Engineering Statistics*. Marcel Dekker, Inc., 1991.

[58] R.M. Rangayyan. *Biomedical Signal Analysis : A Case-Study Approach*. Wiley-IEEE Press, Piscataway, New Jersey, 2002.

[59] C. Lessard. *Signal Processing of Random Physiological Signals (Synthesis Lectures on Biomedical Engineering)*. Morgan & Claypool, 2006.

[60] M.B. Priestley. *Non-Linear and Non-Stationary Time Series Analysis*. Academic Press, London, United Kingdom, 1988.

[61] W. Wenhua and W. Wenxing. Recursive least squares algorithm for nonstationary random signal. *3rd International Conference on Signal Processing*, 12:197–200, 1996.

[62] W. Martin and P. Flandrin. Wigner-ville spectral analysis of nonstationary processes. *IEEE Trans. Acoust. Speech Signal Process.*, 33:1461–1470, 1985.

[63] A.V. Oppenheim and R.W. Schafer. *Digital Signal Processing*. Prentice-Hall, 1975.

[64] P. Vaniček. Approximate spectral analysis by least squares fit. *Astrophys. & Space Sci.*, 4:387–391, 1969.

[65] N.R. Lomb. Least-squares frequency analysis of unequally spaced data. *Astrophys. & Space Sci.*, 39:447–462, 1975.

[66] J.D. Scargle. Studies in astronomical time series analysis ii. statistical aspects of spectral analysis of unevenly spaced data. *Astrophys. J.*, 263:835–853, 1982.

[67] H.P.A. Van Dongen, E. Olofsen, J.H. Van Harteveldt, and E.W. Kruyt. Searching for biological rhythms: Peak detection in the periodogram of unequally spaced data. *J. Biol. Rhythms*, 14(6):617–620, 1999.

[68] P. Vaniček. Further development and properties of the spectral analysis by least-squares. *Astrophys. & Space Sci.*, 12:10–33, 1971.

[69] R.A. Muller and G.J. MacDonald. *Ice Ages and Astronomical Causes: Data, Spectral Analysis and Mechanisms*. Springer London Ltd, 2000.

[70] L. Cohen. *Time-Frequency Analysis*. Prentice-Hall, 1995.

[71] H. Choi and W.J. Williams. Improved time-frequency representation of multicomponent signals using exponential kernels. *IEEE. Trans. Acoustics, Speech, Signal Processing*, 37(6):862âĂŞ871, 1989.

[72] A. Swami, J. Mendel, and C. Nikias. Higher-order spectral analysis toolbox for use with MATLAB®, 2003.

[73] Y. Zhao, L.E. Atlas, and R.J. Marks. The use of cone-shaped kernels for generalized time-frequency representations of nonstationary signals. *IEEE Trans. Acoust. Speech Signal Process.*, 38(7):1084–1091, 1990.

[74] G. Matz and F. Hawatsch. Time-frequency coherence analysis of nonstationary random processes. In *10th IEEE Workshop Stat. Signal Array Process., Pocono Manor PA*, pages 554–558, 2000.

[75] M. Muma, D.R. Iskander, and M.J. Collins. The role of cardiopulmonary signals in the dynamics of the eye's wavefront aberrations. *IEEE Trans. Biomed. Eng.*, 57(2):373–383, 2010.

[76] L.B. White and B. Boashash. Cross spectral analysis of nonstationary processes. *IEEE Trans. Inf. Theory*, 36(4):830–835, 1990.

[77] A. Clauset, C.R. Shalizi, and M.E.J. Newman. Power-law distributions in empirical data. arXiv:0706.1062v1, URL http://arxiv.org/abs/0706.1062v1., 2007.

[78] D. Sornette. *Critical Phenomena in Natural Sciences*. Springer, 2003.

[79] N. Kasdin. Discrete simulation of colored noise and stochastic processes and 1/f power law noise. *Proc. IEEE*, 83:802–827, 1995.

[80] J.M. Hausdorff and C.K. Peng. Multiscaled randomness: A possible source of 1/f noise in biology. *Phys. Rev. E*, 54(2):2154–2157, Aug 1996.

[81] T. Yambe, S. Nanka, S. Naganuma, S. Kobayashi, S. Nitta, T. Fukuju, M. Miura, N. Uchida, K. Tabayashi, A. Tanaka, M. Takayasu, K. Abe, H. Takayasu, M. Yoshizawa, and H. Takeda. Extracting 1/f fluctuation from the arterial blood pressure of an artificial heart. *J. Artif. Organs*, 20:777–782, 1996.

[82] P.C. Ivanov, L.A. N. Amaral, A.L. Goldberger, S. Havlin, M.G. Rosenblum, H.E. Stanley, and Z.R. Struzik. From 1/f noise to multifractal cascades in heartbeat dynamics. *Chaos*, 11(3):641–652, 2001.

[83] P. Celka and P. Colditz. Nonlinear nonstationary wiener model of infant seizures. *IEEE Trans. Biomed. Eng*, 49(6):556–564, 2002.

[84] D.R. Iskander, M.R. Morelande, and M.J. Collins. Estimating the dynamics of aberration components in the human eye. In *IEEE Signal Process. Workshop Statist.*, pages 241–244, 2001.

[85] M.S. Smirnov. Measurement of the wave aberrations of the eye. *Biophysics*, 6:766–795, 1961.

[86] J. Liang, B. Grimm, S. Goelz, and J.F. Bille. Objective measurement of wave aberrations of the human eye with the use of a Hartmann-Shack wave-front sensor. *J. Opt. Soc. Am. A*, 11(7):1949:1957, 1994.

[87] S. Bara. Measuring eye aberrations with Hartmann-Shack wave-front sensors: Should the irradiance distribution across the eye pupil be taken into account? *J. Opt. Soc. Am. A.*, 20(12):2237–2245, 2003.

[88] H.H. Barrett and K.J. Myers. *Foundations of Image Science*. Wiley & Sons, Inc., 2004.

[89] W.H. Southwell. Wave-front estimation from wave-front slope measurements. *J. Opt. Soc. Am.*, 70:998–1006, 1980.

[90] L. Diaz-Santana and J.C. Dainty. Effects of retinal scattering in the ocular double-pass process. *J. Opt. Soc. Am. A*, 18(7):1437–1444, 2001.

[91] C. Leroux. *Time-resolved aberrometry with a Shack-Hartmann wavefront sensor*. PhD thesis, School of Physics, NUI Galway, 2010.

[92] L. Llorente, L. Diaz-Santana, D. Lara-Saucedo, and S. Marcos. Aberrations of the human eye in visible and near infrared illumination. *Optom. Vis. Sci.*, 80:26–35, 2003.

[93] S. Martinez-Conde, S.L. Macknik, and D.H. Hubel. The role of fiixational eye movements in visual perception. *Neuroscience*, 5:229–240, 2004.

[94] J.P. Ryle, M. Al-Kalbani, N. Collins, U. Gopinathan, Gerard Boyle, D. Coakley, and J.T. Sheridan. Compact portable ocular microtremor sensor: design, development and calibration. *J. Biomed. Opt.*, 14(1):014021, 2009.

[95] M. Zhu. *Microfluctuations of Wavefront Aberrations of the Eye*. PhD thesis, School of Optometry, Queensland University of Technology, 2005.

[96] D.A. Benedetto, D.O. Shah, and H.E. Kaufman. The instilled fluid dynamics and surface chemistry of the tear film. *Investigative Ophthalmology & Visual Science*, 14:887–902, 1975.

[97] J.I. Prydal, P. Artal, H. Woon, and F.W. Campbell. Study of human precorneal tear film thickness and structure using laser interferometry. *Invest. Ophthalmol. Vis. Sci.*, 33:2006–2011, 1992.

[98] N. Davies, L. Duaz-Santana, and D. Lara-Sucedo. Repeatability of ocular wavefront measurement. *Optom. Vis. Sci.*, 80(2):142–150, 2003.

[99] L. Diaz-Santana, C. Torti, I. Munro, P. Gasson, and C. Dainty. Benefit of higher closed-loop bandwidths in ocular adaptive optics. *Opt. Express*, 11(20):2597–2605, 2003.

[100] M. Al-Abdulmunem. Spontaneous blink rate of a normal population sample. *Int. Contact Lens Clin.*, 26(2):29–32, 1999.

[101] M. Collins, B. Davis, and J. Wood. Microfluctuations of steady-state accommodation and the cardiopulmonary system. *Vision Res.*, 17:2491–2502, 1995.

[102] P.S. Naidu and B. Paramasivaiah. Estimation of sinusoids from incomplete time series. *IEEE Trans. Acoust. Speech Signal Process.*, 32(3):559–662, 1984.

[103] H. Dante. Spectrum estimation of time series with missing data. *IEEE International Conference on Acoustics, Speech, and Signal Processing*, 10:89–92, 1985.

[104] N.J. Grossbard and E.M. Dewan. Methods for estimating the autocorrelation and power spectral density functions when there are many missing data values. In *Proceedings of Fifth ASSP Workshop on Spectral Estimation and Modelling*, 1990.

[105] J.D. Bartlett and S.D. Janus. *Clinical Ocular Pharmacology (4th Edition)*. Butterworth-Heinemann, London, 2000.

[106] G. Goertzel. An algorithm for the evaluation of finite trigonometric series. *Amer. Math Monthly*, 65(1):34–35, 1958.

[107] François Auger, Olivier Lemoine, Paulo Gonçalvès, and Patrick Flandrin. The time-frequency toolbox, 1996.

[108] M. Kobayashi and T. Musha. 1/f fluctuation of heartbeat period. *IEEE Trans. Biomed. Eng.*, 29(6):456–457, 1982.

[109] H.B. Dick. Accommodative intraocular lenses: Current status. *Curr. Opin. Ophthalm.*, 16:8–26, 2005.

[110] P.B. Kruger, S. Matthews, M. Katz, K.R. Aggarwala, and S.A. Nowbotsing. Accommodation without feedback suggests directional signals specify ocular focus. *Vision Res.*, 37(18):2511–2526, 1997.

[111] L.S. Gray, B. Winn, and B. Gilmartin. Effect of target luminance on microfluctuations of accommodation. *Ophthal. Physiol. Opt.*, 13(3):258–265, 1993.

[112] G.L. van der Heijde, A.P.A. Beers, and M. Dubbelman. Microfluctuations of steady-state accommodation measured with ultrasonography. *Opthal. Physiol. Opt.*, 16(3):216–221, 1996.

[113] F.W. Campbell and J.G. Robson. High-speed infrared optometer. *J. Opt. Soc. Am.*, 49(3):268–272, 1959.

[114] K.M. Hampson, S.S. Chin, and E.A.H. Mallen. Dual wavefront sensing channel monocular adaptive optics system for accommodation studies. *Opt. Express*, 17(20):18229–18240, 2009.

[115] A. Arnulf and O. Dupuy. Contribution to the study of microfluctuations of accommodation of the eye (in French). *Rev. Opt.*, 39:195–208, 1969.

[116] W. Nowak, A. Hachol, and H. Kasprzak. Time-frequency analysis of spontaneous fluctuation of the pupil size of the human eye. *Optica Applicata*, 38(2):469–480, 2008.

[117] The Mathworks™. Technical solutions: How do I perform regression and impose a constraint on the regression function?, June 2009.

[118] J.L. Cabrera and J.G. Milton. Human stick balancing: Tuning Lévy flights to improve balance control. *Chaos*, 14 (3):691–698, 2004.

[119] C.W. Eurich and K. Pawelzik. Optimal control yields power-law behavior. Lect. Notes Comput. Sci., Springer, 2005.

[120] J.L. Cabrera and J.G. Milton. Self-similarity in a human balancing task. In *Proceedings of the Second Joint EMBS/BMES Conference*, 2002.

[121] R. Navarro, E. Moreno-Barriuso, S. Bará, and T. Mancebo. Phase plates for wave-aberration compensation in the human eye. *Opt. Lett.*, 25(4):236–238, 2000.

[122] S.O. Galetskiy, T.Yu. Cherezova, and A.V. Kudryashov. Adaptive optics in ophthalmology: human eye wavefront generator. *Proc. SPIE*, 6849:6849091–8, 2008.

[123] H.M. Culhane and B. Winn. Dynamic accommodation and myopia. *Invest. Ophthalmol. Vis. Sci.*, 40(9):1968–1974, 1999.

[124] B. Gilmartin and M.A. Bullimore. Adaptation of tonic accommodation to sustained visual tasks in emmetropia and late-onset myopia. *Optom. Vis. Sci.*, 68(1):22–26, 1991.

[125] A. Dunne. Time series simulation. *J. Roy. Statist. Soc.*, 41:3–8, 1992.

[126] B. Le Roux, J.M. Conan, C. Kulcsár, H.F. Raynaud, L.M. Mugnier, and T. Fusco. Optimal control law for classical and multiconjugate adaptive optics. *J. Opt. Soc. Am. A.*, 21(7):1261–1276, 2004.

[127] K. Billah and M. Shinozuka. Numerical method for colored noise generation and its application to a bistable system. *Phys. Rev. A*, 42(12):7492–7495, 1990.

[128] B. Boashash and M. Mesbah. A time-frequency approach for newborn seizure detection. *IEEE Eng. Med. Biol. Mag.*, 20(5):54–64, 2001.

[129] L. Rankine, N. Stevenson, M. Mesbah, and B. Boashash. A nonstationary model of newborn eeg. *IEEE Trans. Biomed. Eng*, 54(1):19–28, 2007.

[130] N. Stevenson, L. Rankine, M. Mesbah, and B. Boashash. Modelling newborn eeg background using a time-varying fractional brownian process. In *EU-SIPCO*, 2007.

[131] T. Ruf. The Lomb-Scargle periodogram in biological rhythm research: Analysis of incomplete and unequally spaced time-series. *Biol. Rhythm Res.*, 30(2):178–201, 1999.

[132] P.Ch. Ivanov, M.G. Rosenblum, C.K. Peng, J. Mietus, S. Havlin, H.E. Stanley, and A.L. Goldberger. Scaling behaviour of heartbeat intervals obtained by wavelet-based time-series analysis. *Letters to Nature*, 383:323–326, 1996.

[133] C. Roberts. Future challenges to aberration-free ablative procedures. *J. Refract. Surg.*, 16:623–629, 2000.